Design, Fabrication, Experimentation and Analysis of High-Speed Microscale Gas Bearings

by

Chee Wei Wong

Bachelor of Science in Mechanical Engineering (1999)

Bachelor of Arts in Economics (1999)

Submitted to the Department of Mechanical Engineering
in partial fulfillment of the requirements for the degree of

Master of Science

at the

MASSACHUSETTS INSTITUTE OF TECHNOLOGY

January 2001

Author .....
Department of Mechanical Engineering
January 19, 2001

Certified by .....
Dr. Stuart A. Jacobson
Research Engineer, Department of Aeronautics and Astronautics
Thesis Supervisor

Certified by .....
Professor Alan H. Epstein
R.C. Maclaurin Professor of Aeronautics and Astronautics
Thesis Supervisor

Read by .....
Professor John G. Brisson II
Professor of Mechanical Engineering
Thesis Reader

Accepted by .....
Professor Ain A. Sonin
Chairman, Department Committee on Graduate Students

Design, Fabrication, Experimentation and Analysis of High-Speed Microscale Gas Bearings

by

Chee Wei Wong

Bachelor of Science in Mechanical Engineering (1999)

Bachelor of Arts in Economics (1999)

Submitted to the Department of Mechanical Engineering
on January 19, 2001, in partial fulfillment of the
requirements for the degree of
Master of Science

Abstract

We report here new and further developments into the MicroBearing device for the MIT Microengine Program. The all-silicon device consist of a free-rotating microturbine, with 4.2 mm rotor diameter, enclosed within a five wafer fusion-bonded stack. Of note are the low aspect ratio journal bearing and large journal bearing clearances, primarily limited by microfabrication, from which stable bearing operation must first be demonstrated as viable. Theoretical modeling of the gas-lubricated hydrostatic journal bearing presents design charts, a comparative study of existing predictions and investigation into rotational effects to consider the bearing stiffness during operation. Continued experimental refinements and exploration with our microfabricated rotor achieved rotational speeds up to 1.4 million rpm and peripheral speeds in excess of 300 m/s. Extensive experimental data is presented with analysis, focusing on whirl motion and its harmonic resonances as candidates for instability. Causes of ultimate failure is suggested with recommendations for further improvements.

Moreover, in an effort to accomplish self-sustained microbearings, the axial thrust bearing is redesigned for a self-acting spiral groove bearing. The chosen constraint is to incorporate the hydrodynamic thrust bearing with minimal changes to the current device, whilst providing the required load and stiffness. Stability analysis and rarefaction considerations on the optimized design suggests an operating range for the bearing, leading to a hybrid design for ample stiffness during initial operation. The design is then developed into a microfabrication process flow and implemented successfully into the MicroBearing test devices. Experiments on a hybrid bearing were performed to gage the spiral grooves characteristics. A purely hydrodynamic aft thrust bearing device is then tested for operation through low speeds, although the effects of the spiral grooves could not be accurately determined. Finally, transition to a hydrodynamic operating mode for a hybrid bearing is demonstrated.

Thesis Supervisor: Dr. Stuart A. Jacobson
Title: Research Engineer, Department of Aeronautics and Astronautics

Thesis Supervisor: Professor Alan H. Epstein
Title: R.C. Maclaurin Professor of Aeronautics and Astronautics

Acknowledgments

I am deeply indebted to several people in the MIT MicroEngine Project, without whom it will be quite impossible to complete this work. To these people, I give my appreciation, thanks and wish them sweet sucess:

- Stuart Jacobson: without whom I will still be reading up on the difference between hydrostatic and hydrodynamic effects.
- Luc Fréchette: without whom, I will still be crashing my devices and searching for the right mass flow controller.
- Chuang-Chia Lin: who developed and demonstrated the first device.
- Doyle Jay Orr and Edward Stanley Piekos: who, together, in their work silently taught me the operation of the MicroBearing rig.
- Xin Zhang: without whom, I will still be spinning photoresist on my wafers.
- Fred Ehrich and Kenny Breuer: for their insights into this project and communicating their experiences to a novice.
- Alan Epstein, who made this all possible, and John Brisson, for the support and thoughts when reading through this thesis.

The list does not end there. Paul Warren helped me put together incredible gadgets, Jimmy Letendre showed me how to work the swagelocks, and Lori Martinez who handled everything so superbly. Thanks also to the wonderful friends in Gas Turbine Lab and Microsystems Technologies Lab, without whom all this would be meaningless.

Finally and most importantly, my Dad, Mum, brother Chee-Yann, and Maggie Chang gave me the choice, the emotional support and the incentive to do this work. This thesis is thus dedicated to my family and Maggie—I can never thank you all enough.

Contents

List of Figures

List of Tables

Nomenclature

a_0	speed of sound under standard conditions
a_1	groove width of spiral groove bearing
a_2	ridge width of spiral groove bearing
α	spiral groove angle of spiral groove bearing
A	analytical numerator for $f_{r\epsilon}$ in spiral groove stability: $3\{(1+\bar{\delta})^2[\bar{b}_1 +(1-\bar{b}_1)(1+\bar{\delta})^4] + \bar{b}_1(1-\bar{b}_1)\sin^2\beta[(1-\bar{b}_1)(1+\bar{\delta})^8 -(2-\bar{b}_1)(1+\bar{\delta})^6 + 2\bar{b}_1(1+\bar{\delta})^5 + 2(1-\bar{b}_1)(1+\bar{\delta})^3 -(1+\bar{b}_1)(1+\bar{\delta})^2 + \bar{b}_1]\}$
$A_{0,a}$	Constantinescu coefficient: $\frac{f_{r0}}{1-\lambda^4}$
$A_{1,a}$	Constantinescu coefficient: $1 + \bar{b}_1\bar{\delta}\frac{1-\lambda^2}{1+\lambda^2}$
$A_{2,a}$	Constantinescu coefficient: $\frac{f_{r\epsilon}}{f_{r0}} - \frac{f_{s\epsilon}}{f_{s0}}$
$A_{3,a}$	Constantinescu coefficient: 1
$A_{4,a}$	Constantinescu coefficient: 1
$A_{0,b}$	Constantinescu coefficient: $(\frac{0.3\lambda f_{r0}}{\lambda-\bar{R}_i} + \frac{1}{1-\lambda^2})(1-\bar{R}_i{}^2)$
$A_{1,b}$	Constantinescu coefficient: $1-\lambda^2 + \frac{(\lambda-\bar{R}_i)(7.2\lambda+3.2\bar{R}_i)}{6} + \frac{2\bar{b}_1\bar{\delta}(\lambda-\bar{R}_i)(1.8\lambda+0.8\bar{R}_i)}{3}$
$A_{2,b}$	Constantinescu coefficient: $\left[\frac{f_{r\epsilon}+\frac{10(\lambda-\bar{R}_i)}{\bar{R}_i(1-\lambda^2)}}{f_{r0}+\frac{3.33(\lambda-\bar{R}_i)}{\bar{R}_i(1-\lambda^2)}} - \frac{f_{s\epsilon}}{f_{s0}}\right]\bar{R}_i{}^2$
$A_{3,b}$	Constantinescu coefficient: $1-\bar{R}_i{}^2 + \frac{(\lambda-\bar{R}_i)(7.2\lambda+3.2\bar{R}_i)}{6}$
$A_{4,b}$	Constantinescu coefficient: $(0.3\bar{R}_i f_{r0} + \frac{\lambda-\bar{R}_i}{1-\lambda^2})/(0.7f_{r0} + \frac{\lambda(\lambda-\bar{R}_i)}{1-\lambda})$
$A_1{}'$	constant in linear pressure approximation of groove in spiral groove
$A_2{}'$	constant in linear pressure approximation of ridge in spiral groove
b	length of spiral groove along spiral direction
$\bar{b}_1$	$\frac{a_1}{(a_1+a_2)}$
χ	inertia parameter: $\frac{\rho W C^2}{\mu}$
χ_{ax}	axial inertia parameter: $\frac{\rho C^4 P_{in}}{12\mu^2 L^2}$

c	arbitrary positive constant
C	bearing clearance
$C_1(\alpha, H, \gamma, \lambda, k)$	end effect correction factor: $\frac{e^{-\frac{\pi}{k}(1-\frac{\alpha}{90})(\tan\alpha)\frac{2}{1+\gamma}\frac{1+\gamma H^3}{1+H^3}} - \lambda^2 e^{+\frac{\pi}{k}(1-\frac{\alpha}{90})(\tan\alpha)\frac{2}{1+\gamma}\frac{1+\gamma H^3}{1+H^3}}}{1-\lambda^2}$
$C_2(\alpha, H, \gamma, \lambda, k)$	end effect correction factor: $\frac{e^{-\frac{2\pi}{k}(1-\frac{\alpha}{90})(\tan\alpha)\frac{2}{1+\gamma}\frac{1+\gamma H^3}{1+H^3}} - \lambda^4 e^{+\frac{2\pi}{k}(1-\frac{\alpha}{90})(\tan\alpha)\frac{2}{1+\gamma}\frac{1+\gamma H^3}{1+H^3}}}{1-\lambda^4}$
$C_1\prime$	constant in linear pressure approximation of groove in spiral groove
$C_2\prime$	constant in linear pressure approximation of ridge in spiral groove
δ	h_2/h_0
$\bar{\delta}$	(current groove film thickness - current ridge film thickness)$/h_2$
d	effective or nominal molecular diameter
dP	axial differential pressure
D	bearing (rotor) diameter
Δp	nondimensional axial differential pressure: $\frac{dP}{P_{ir}}$
e	distance between bearing and journal center
ϵ	nondimensional eccentricity ratio: $\frac{e}{C}$
η	viscosity of fluid $(N \cdot sec/m^2)$
f_{r0}	Constantinescu parameter: $\frac{\bar{h}_1^3+\bar{b}_1(1-\bar{b}_1)(\bar{h}_1^3-1)^2\sin^2\beta}{(1-b_1)\bar{h}_1^3+\bar{b}_1}$
$f_{r\epsilon}$	Constantinescu parameter: $\frac{A}{[(1-\bar{b}_1)(1+\bar{\delta})^3+\bar{b}_1]^2}$
f_{s0}	Constantinescu parameter: $\frac{\bar{h}_1^3+\bar{b}_1(1-\bar{b}_1)(\bar{h}_1^3-1)^2\sin^2\beta}{(1-b_1\,\bar{h}_1^3+\bar{b}_1}$
$f_{s\epsilon}$	Constantinescu parameter: $\frac{3\bar{\delta}(1+\bar{\delta})^2}{[(1-\bar{b}_1)(1+\bar{\delta})^3+\bar{b}_1]^2}$
f_u	Constantinescu parameter: $2\bar{b}_1(1-\bar{b}_1)\,\bar{\delta}\,\sin\beta$
$g_1(\alpha, H, \gamma)$	main correction factor: $\frac{\gamma H^2(\cot\alpha)(1-H)(1-H^3)}{(1+\gamma H^3)(\gamma+H^3+H^3(\cot^2\alpha)(1+\gamma)^2}$
$g_2(\alpha, H, \gamma)$	$\frac{g_2^*(\alpha,H,\gamma)}{1+\gamma}$
$g_2^*(\alpha, H, \gamma)$	$(\gamma+H)+\frac{3\gamma H(1-H)^2(1+\gamma H^3)}{(1+\gamma H^3)(\gamma+H^3)+H^3(\cot^2\alpha)(1+\gamma)^2}$
γ	a_2/a_0

H	$h_2/h_1; \frac{H}{(1-H)}$
h_0	groove depth of spiral groove bearing
h_1	$h_0 + h_2$
h_2	ridge film height of spiral groove bearing
h_c	depth in inner chamber of spiral groove bearing
$\bar{h_1}$	current groove film thickness/ h_2
Kn	Knudsen number
k	number of grooves in spiral groove bearing
k_s	hydrostatic film stiffness
κ	Boltzmann's constant
L	journal bearing length
Λ	nondimensional bearing number: $\frac{6\mu w}{P_a}(\frac{R}{C})^2$
Λ_c	compression number in spiral grooves: $\frac{3\mu\omega_h r_2^2}{P_a h_2^2}$
λ	$\frac{r_1}{r_2}$
m	number of grooves, k, plus number of ridges in spiral groove bearing
M_t	frictional torque from spiral groove bearing
$\bar{M}$	nondimensional mass: $\frac{mP_a}{72L\mu^2}(\frac{C}{R})^5$
μ	dynamic viscosity $(Pa.s)$
n	molecular number density
ω	angular velocity (rad/sec)
P	general pressure term
P_a	ambient pressure
P_{ir}	interrow pressure, at exit of journal bearing
P_s	supply pressure to fluid film of concern
$\hat{P}$	nondimensional pressure: $\frac{P_s}{P_a}$
p_{exact}	analytical solution of pressure difference in spiral groove bearing

p_{r1}	pressure buildup (above ambient) at radius r_1 of spiral groove bearing
ϕ	attitude angle
R	bearing (rotor) radius
Re	Reynolds number: $\frac{2\rho u_s C}{\mu}$
$\bar{R}_i$	radius of possible shaft through thrust bearing/r_2
r_1	inner radius of spiral groove bearing
r_2	outer radius of spiral groove bearing
r_{1eff}	effective inner radius of spiral groove bearing
r_{2eff}	effective outer radius of spiral groove bearing
ρ	fluid density
Ta	Taylor number: $\frac{\rho^2 R W^2 C^3}{\mu^2}$
U	nondimensional axial core velocity: $\frac{axialvelocity(downstream)}{u_s}$
u_s	uniform axial velocity at journal inlet
W	rotational frequency
W_n	whirl resonant frequency
$W_{n,helmholtz}$	Helmholtz resonant frequency
W_t	load capacity of bearing
w	rotational rate (rad/s)

Chapter 1

Introduction

Nothing tends so much to the advancement of knowledge as the application of a new instrument. The native intellectual powers of men in different times are not so much the causes of the different success of their labours, as the peculiar nature of the means and artificial resources in their possession.
—Sir Humphrey Davy, 1778-1829.

1.1 Background—The MIT MicroEngine Project

Exploration into the micro-scale domain brings out fascinating effects and allows for creative devices and systems [29, 20]. Epstein *et al.* in 1995 presented the feasibility for a MEMS[1]-based gas turbine engine with power densities significantly better than the best military batteries available, enabling new frontiers in propulsion and power generation [26, 27].

The baseline MicroEngine proposed, as illustrated in Figure 1-1, introduces a 1 cm diameter by 3 mm thick Si heat engine with a power density in the vicinity of 2300 MW/m^3 [25]. A power output 10-20 W is estimated for a 10 $gram/hr$ H_2-burning engine, with comparable results for later generation engines burning hydrocarbon fuels [28]. While the cube-square law[2] for power density allows us to achieve the high power density and favors a minimal

[1]Micro Electro Mechanical Systems.

[2]Cycle power output of an engine scales with the flow rate and thereby the flow area; weight simply scales

length scale, other considerations such as Couette drag, combustion efficiency, instrumentation and microfabrication of critical lengths set the lower bound on the length scale [36, 43]. In addition, an evaluation of the engine performance through classic thermodynamic cycles suggest equivalent acheivements of the MicroEngine to their full-sized brethens [32, 24].

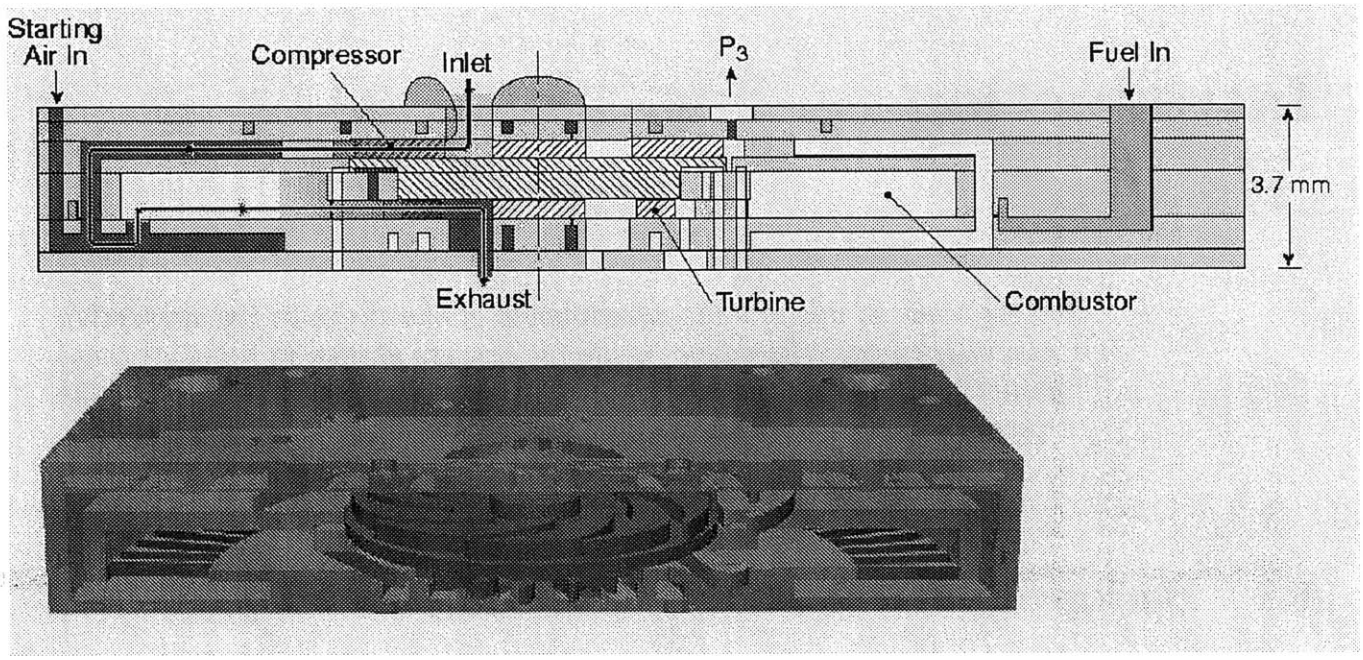

Figure 1-1: Baseline design of the MIT MicroEngine [25]. Top: Demo engine cross-section at two different radial locations. Bottom: 3-D section of the demo engine. (Courtesy of Diana Park)

To demonstrate the technology necessary for a fully-integrated MicroEngine, several main components were designated for individual demonstration:

1. *Sustainable high-temperature efficient combustors*: High peak cycle temperatures in the range of 1200 to 1800 K are neccessary to achieve the desired level of efficiency for the Brayton gas turbine cycle. Operation at this temperature range, dedicated by

with the volume. The resulting power density then scales directly with the inverse of the length scale.

silicon material constraints, needs to be validated. Residence time is also an issue on combustion chemical efficiency. This is discussed in [70, 44] and recent work presented in [45, 64].

2. *Low friction bearings for high-speed turbomachinery operation*: A demonstration of high-speed rotating micro-machinery supported on low friction bearings is necessary. Tip speeds in the range of 300 to 600 m/s are required for a single-stage centrifugal compressor pressure ratio of 4:1. Design considerations are presented in [59, 58] and a 26:1 scaled-up "macro" version was pursued [54] to explore the parameter space, given the uniqueness of our regime from existing literature. To-scale "micro" devices were reported in [40, 31].

3. *Efficient electrical machinery*: In the electromechanical conversion for the induction generator/motor, high temperature and high speed operations create new challenges to previous MEMS micromotors which typically operate in the range of $10^{-8}W$ [66, 4]. This is discussed in [50] and the results summarized in [51, 31].

Furthermore, in each of these components, the need for proper consideration of material characteristics is immediately apparent. Finally, extending into the microscale regime also introduces the inherent challenges of microfabrication, instrumentation and packaging, of which ingenious solutions often arise in successful devices.

1.2 Development of a MicroBearing investigation

Development of a MicroBearing test device thus stems from attempting to achieve a transonic Mach number with the turbomachinery. As a quick and simple introduction, Figure 1-2 illustrates the nomenclature involved. The design space, limited primarily by microfabrication techniques, is significantly different from typical values found in literature, resulting in

the need to explore the rotordynamic stability issues. Specifically, the parameters of concern[3] are:

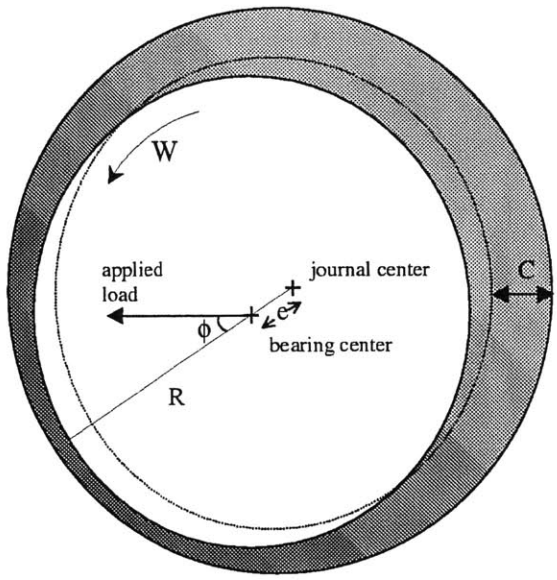

Figure 1-2: Nomenclature terms in the journal bearing.

L/D : A microfabricated journal bearing length, L, to the rotor diameter, D, ratio at 0.075, an order of magnitude smaller than typical bearings in literature.

W : A rotational speed, W, two orders of magnitude larger than commonly found. This is due to the required tip speed and small rotor radius.

C/R : A journal bearing clearance, C, to rotor radius, R, ratio at approximately five times larger than typical reported.

ζ : A nondimensional load parameter[4], ζ, approximately two orders of magnitude smaller than previous reported values. This is because ζ scales proportionately with the length scale.

[3]Other common nondimensional parameters such as the dimensionless mass, $\bar{M}$, and the bearing number, Λ, are in the typical range of unity and from 10^{-1} to 10^{1} respectively.

[4]ζ is defined as $\frac{W}{2RLP_a}$.

This unique parameter space thus necessitated the theoretical modeling of the bearing stability, a proof of feasibility on a macroscale device and finally actual bearing operation at the microscale regime. A gas-lubricated bearing was conceived as the most probable option over electrostatic and magnetic bearings[5]. In electrostatic bearings, there is the need to introduce additional[6] circuitry for an electrostatic [48] bearing; in magnetic bearings, the added complexity is deemed unfeasible at the microscale currently.

1.2.1 The Device and Previous MicroBearing work

Figure 1-3 shows the device that encloses the microrotor and the bearings. Of note are the flow systems and plenums for the device, whilst the rotor is hidden from view. Figure 1-4 highlights the rotor and its subcomponents under infra-red illumination.

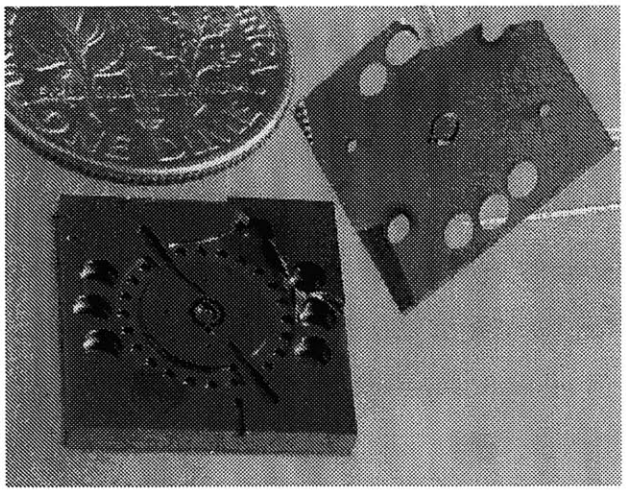

Figure 1-3: Sectioned overview of the MicroBearing device.

[5]Other choices of bearings such as rolling elements and more viscous liquid lubricants will lead to high dissipation with difficulty of incorporation into the final MicroEngine and thus not feasible

[6]The electrostatic circuitry is termed as "additional" since the journal gap must be present for rotation. And, since it will be difficult to pump the gap to vacuum, fluidic flow will be present in the bearing—of which gas-lubricated hydrodynamic effects will dominate.

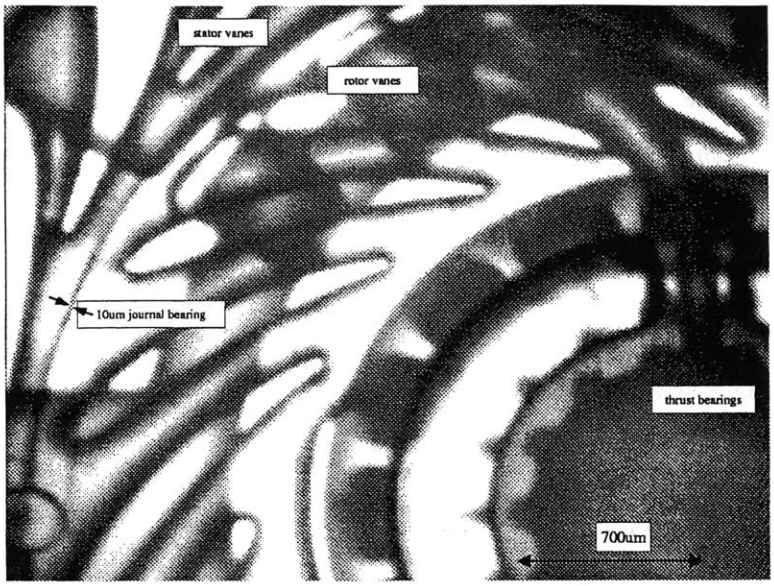

Figure 1-4: Infra-red map of the MicroBearing Rig.

In previous work on this device, Piekos provided an extensive numerical simulation of the gas-lubricated journal bearing, considering both hydrodynamic and hydrostatic operational modes [57]. He also provided a study into variants of the plain, cylindrical journal bearings. Concurrently, Ehrich developed a 26:1 scaled-up rig which Orr employed to demonstrate operation in the new parameter space [54], and Lin and Khanna established the fabrication process flow and initial testing of the first MicroBearing device [40]. Savoulides combined theoretical models to effect a suggested hybrid hydrostatic-hydrodynamic mode [63]. Fréchette improved the current design and fabrication techniques, and first demonstrated possible high-speed operation [31]. Jacobson, Breuer and Ehrich also provided important experience and guidance to the team throughout the MicroBearing development [35, 9, 21]. Microfabrication expertise was further included by Zhang in later developments [76].

1.3 Problem Statement and Methodology

We began with (1)an evaluation of the existing theoretical models for the hydrostatic journal bearing, and (2)a characterization of the experimental performances of the MicroBearing devices. Chapter 2 puts together the former—a comparison of the theoretical models and design charts based on these models. We also include a discussion on the rotational effects and ideas for better hydrostatic journal bearing modeling.

Chapter 3 involves a broad range of experimental work on the MicroBearing devices—ranging from flow testing, to modification of the experimental setups, to development of better operating schedules. We present a host of data on multiple device tests with the derived operating protocol and the resulting frequency spectra on rotor whirl motion. Analysis of the experimental data suggests likely causes of ultimate failure. We thus follow with recommendations on development of an eccentricity sensor and incorporation of variant journal bearing designs.

Development into the next-generation MicroBearing device, moreover, requires self-sustained[7] bearings for the MicroEngine. Since the hydrostatic thrust bearings require large external pressurizations in the order of 60-80 psig (compared to the main turbine inlet pressurization of approximately 20 psig at 1.4 million rpm), the development plan was to incorporate self-pressurizing hydrodynamic squeeze-film thrust bearings to satisfy the requirements. The final part of this thesis was thus committed to modeling the hydrodynamic effects at the thrust bearings. Chapter 4 discusses the issues involving optimal design, stability issues and possible causes for failure during operation. Chapter 5 establishes the fabrication process flow and presents the implemented fabrication results. Initial tests on the actual devices are reported.

The methodology taken in this research is summarized in Figure 1-5, wherein the approach begans with the hydrostatic journal bearing and later moves onto the hydrodynamic

[7]We coin the term "self-sustained" here as indicative of the bearing pressurizations at a fraction of the main turbine inlet pressure, to allow a single maxima pressurization at the turbine.

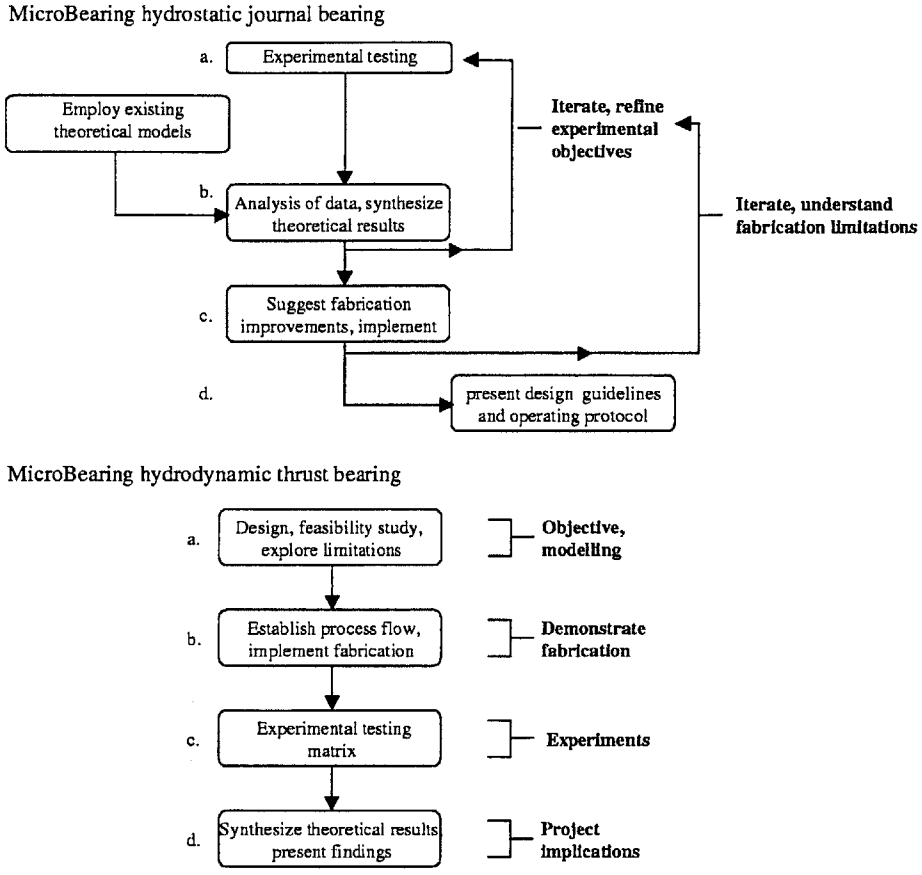

Figure 1-5: Schematic on approach for MicroBearing developments.

thrust bearing. To place the experimental hydrostatic journal bearing work into perspective, we now begin with the theoretical modeling efforts on the hydrostatic journal bearing.

Chapter 2

Hydrostatic Journal Bearing: Theory

I do not know what I may appear to the world; but to myself
I seem to have been only like a boy playing on the seashore,
and diverting myself in now and then finding a smoother pebble
or a prettier shell than ordinary, while the great ocean of truth
lay all undiscovered before me.
—I. Newton, 1642-1727.

The initial focus of the MicroBearing research effort was on hydrodynamic journal bearings, with its operation modeled extensively against several design parameters. The theoretical work on a hydrostatic journal bearing, interestingly, served only as a sidenote to the hydrodynamic journal bearing work in Piekos and Orr [57, 54]. Other theoretical work in the journal bearings includes: (1) a hybrid between the hydrostatic and hydrodynamic effects by Savoulides [63], and (2) a feasibility study of electrostatic journal bearings by Mur Miranda [48]. Though hydrodynamic journal bearing operation is not ruled out, hydrostatic operation has, however, since proved to be a feasible procedure for MicroBearing operation and hence is further explored in this work.

This chapter provides a quick synopsis on hydrostatic journal bearing theory, working on the basis of previous modeling. We began with a comparison of the hydrostatic models developed, followed by an exploration into the rotational effects on journal bearing stiffness,

and then present a set of design charts for the hydrostatic journal bearing.

2.1 Comparison of hydrostatic models

Piekos [57] modelled the hydrostatic stiffness through an analytical solution cited in Bhatti and Savery [6]. The 1976 paper, working with only the entrance length region, assumed a velocity profile and solved for the presure distribution:

$$P = -\frac{3}{280}\rho u_s^2[22U^2 - 10U - 12 - 15ln(3 - 2U)] + P_s \tag{2.1}$$

A linear pressure distribution is then assumed for the rest of the journal bearing. An integration of this pressure distribution gives the bearing force, after subtracting the inertia effect. The means of estimating this entrance length effect is by choosing it to be the position such that it reaches 99.9% of the uniform downstream velocity.

Interestingly, the resulting stiffness is not linear with eccentricity. Piekos, in modelling of the hydrostatic stiffness, found that there were three stages of stiffness that can be explained with the $\chi_{ax}\Delta p$ parameter [57], where χ_{ax} is found from geometric parameters and Δp a non-dimensional axial differential pressure[1]:

- At low $\chi_{ax}\Delta p$ (on the order of 1): The stiffness increases with eccentricity, such that small perturbations at zero eccentricity sees a smaller stiffness than at larger eccentricities.

- At moderate $\chi_{ax}\Delta p$ (on the order of 30): Here stiffness is maximum at zero eccentricity. Slight perturbations from the zero eccentricity brings out a decreased stiffness.

- At very high $\chi_{ax}\Delta p$ (on the order of 100): Here the maximum stiffness again lies away from zero eccentricity. A perturbation at zero eccentricity sees less stiffness than at an

[1] $\chi_{ax} = \frac{\rho C^4 P_{ir}}{12\mu^2 L^2}$ and $\Delta p = \frac{dP}{P_{ir}}$. P_{ir} is the inter-row pressure above the blades and dP the axial differential pressure.

off-centered position.

Our MicroBearing device χ_{ax} is found to be approximately 8.8[2]. With our operating Δp at up to 20 during initial spin-up and continually decreasing to less than unity, this suggests a possible transition between the three stiffness stages as first illustrated by Piekos. In Figure 2-1, we illustrate the resulting natural frequency from this model at a moderate $\chi_{ax}\Delta p$. We plot the natural frequency against the axial differential pressure for two different eccentricities (zero and 10% eccentricity) in this regime. We note that the natural frequency does decrease with the eccentricity, though only slightly, and increases steadily with the axial differential pressure.

The hydrostatic journal bearing is also modelled by Breuer [9], though work from Tang and Gross [68]. The work furnishes design curves for inherently-compensated and orifice-compensated bearings, based on analytical solutions of viscous flow equations[3]. In this instance, the pressure profile is

$$P(x) = \sqrt{\frac{\hat{P}^2 - \frac{r_i}{r_o} - \frac{x}{r_o}(\hat{P}^2 - 1)}{1 - \frac{x}{r_o}}} \tag{2.2}$$

where r_i and r_o are the inner and outer lengths of the journal bearing respectively, x the distance along the journal bearing, and $\hat{P}$ the nondimensional supply pressure. The nondimensional supply pressure, $\hat{P}$, is also a function of a discharge coefficent C_d, typically around 0.9 and 1, with the latter for an inherently compensated journal bearing. Moreover, the load, W_t, is expressed directly with

$$\frac{W_t}{P_a A} = \hat{P}\left[1 - \frac{(1 - \frac{r_i}{r_o})(3 + \hat{P})}{3(1 + \hat{P})}\right] - \frac{1 + 2\frac{r_i}{r_o}}{3} \tag{2.3}$$

where A is the area of the restricting orifice.

[2] χ_{ax} scales linearly with journal outlet pressure—P_{ir}, in our device.

[3] The solutions are limited to laminar flow with negligible fluid inertia, and parallel bearing surfaces. The model, however, does not account for relative motion of bearing surfaces like in our situation.

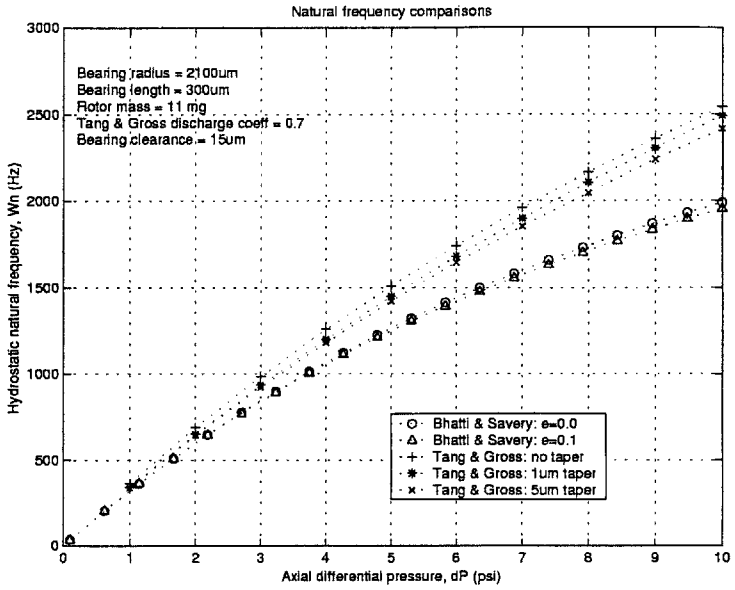

Figure 2-1: A comparison of the hydrostatic natural frequency between the Bhatti-Savery and Tang-Gross models by Piekos and Breuer respectively [57, 9].

A natural frequency comparison of the Bhatti-Savery model by Piekos and Tang-Gross model by Breuer is illustrated in Figure 2-1. We observe a good coherence between the models within the axial differential pressures of concern in the MicroBearing device, though the gradients are slightly differing above approximately 5 psi. Both models predict the natural frequency as increasing with axial differential pressure.

Finally, the Bhatti-Savery modeling assumes a uniform velocity profile prior to entrance into the journal bearing. However, this assumption may have to be modified because of the possible flow separation, brought out by the sharp 90^o turn at the entrance. An orifice computation, such as brought up in the second model by Breuer [9], might be more relevant to account for this additional effect.

Orr also presented a model that coincides well with the above two models [54]. Working with the interacting boundary layer theory from MIT lectures presented by Drela [19], Orr used an empirical scheme from White [72] to compute the hydrostatic natural frequency. Moreover, Orr computed the radial hydrostatic load for different eccentricities at the same axial differential pressure. He, however, noted that the load roughly flattens out with ec-

centricity and advocated the use of a linear spring stiffness when computing our natural frequency.

2.2 Rotational Effects

The outer wall of the journal bearing moves at a high circumferential speed. However, the hydrostatic bearing analysis of the previous section neglected rotational effects on the flow. This assumption must be validated. A typical model considers the flow effects between concentric cylinders at a constant gap[4], with inner cylinder rotating. Coney and El-Shaarawi models this effect in the entrance length regime, which is applicable for us with a short journal bearing of 0.075, by a simplification of the Navier-Stokes equations and solving numerically with a finite-difference scheme [12]. They present several computations with a common factor—Re^2/Ta—as representative of whether the rotational effect can be decoupled from the axial through-flow, where Re is the Reynolds number and Ta the Taylor number. The parameter is obtained after nondimensionalizing a reduced form of the Navier-Stokes equations. We translate this factor, for our device, into

$$\frac{Re^2}{Ta} = \frac{4u_s^2}{CRW^2}. \tag{2.4}$$

This is actually a simple ratio of the axial through-flow energy to the rotational energy [56]. Knowing the actual experimentally-obtained journal bearing flowrate[5], the rotational speed and the relevant geometries, we observe the following dependence on speed in Figure 2-2. We also append in Figure 2-3 the computed experimental axial velocity in our MicroBearing operation.

From Figure 2-2, our $\frac{Re^2}{Ta}$ parameter is on the order of 10^2 for our device. Coney and

[4]This is possible in the hydrostatic mode where the amplitude of the whirl motion is small, compared to hydrodynamic operation.

[5]The journal bearing flowrate was obtained through a previously defined experimental spin-up schedule that kept the ratio of speed versus axial differential pressure approximately constant.

El-Shaarawi cite a 0.3% increment in pressure drop over a stationary parallel wall situation for $\frac{Re^2}{Ta} \geq 10$ and a 3% increment for $\frac{Re^2}{Ta} \geq 1$. This suggests the rotating core for our device as having negligible effect on the pressure drop in the journal bearing. In a purely hydrostatic journal bearing operation, we would thus expect an insignificant change in whirl natural frequency when varying the rotational speed.

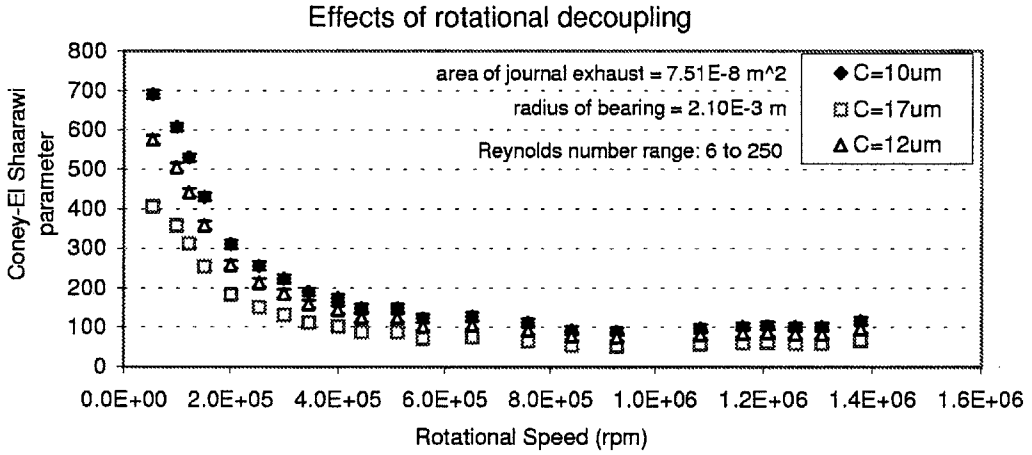

Figure 2-2: The Coney and El-Shaarawi parameter against rotational speed for our MicroBearing geometry.

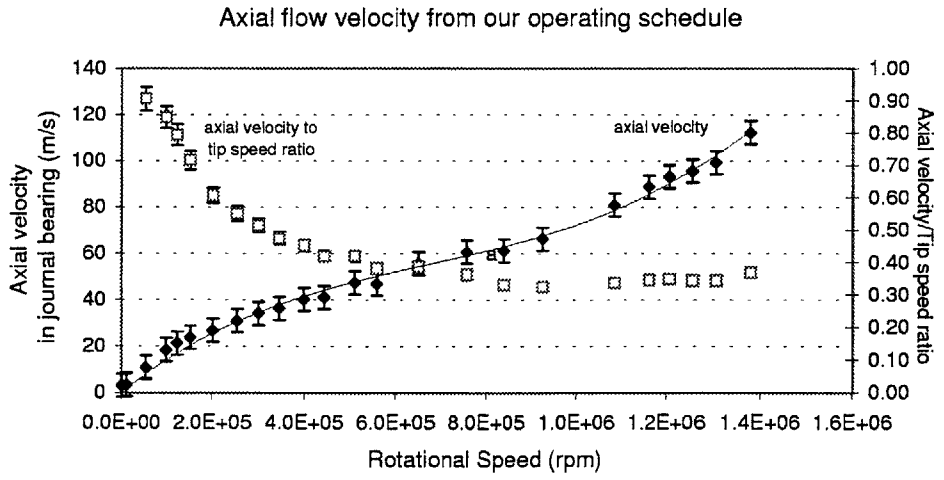

Figure 2-3: The axial velocity in the journal bearing from experimentally-obtained flowrates.

2.3 Design charts

Modification of the current plain, cylindrical journal bearing design for hydrostatic operation, apart from other kinds of journal bearings, fall into a simple three degrees-of-freedom design space. The variables involved are:

- Journal bearing clearance, C
- Journal bearing length, L
- Journal bearing radius, R

with the interest in stiffness (and associated natural frequency) for journal bearing operation. Based on the current hydrostatic model from Piekos, the following design space is mapped out in Figure 2-4 and 2-5 for different axial differential pressures.

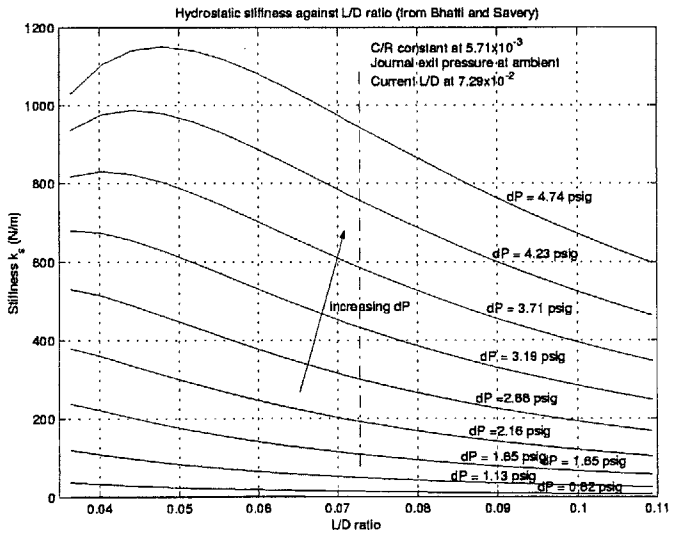

Figure 2-4: Hydrostatic stiffness against $\frac{L}{D}$ for differing axial differential pressures.

This sample calculation is for our current MicroBearing geometry and operating range: L/D at 7.29×10^{-2}, C/R at 5.71×10^{-3}, and axial differential pressures up to 5 psig. In our current design space, Figure 2-5 suggests increasing C/R results in a larger stiffness for a given axial differential pressure. In fact, $\frac{\Delta k_s}{\Delta c/R}$ still increases for our design space. On

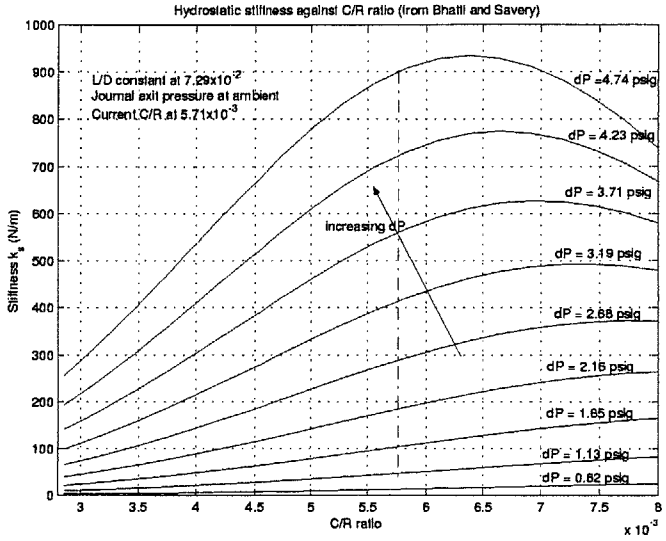

Figure 2-5: Hydrostatic stiffness against $\frac{C}{R}$ for differing axial differential pressures.

the other hand, increasing L/D at a given axial differential pressure decreases the stiffness. Moreover, this model suggests our current design as slightly deviating from the optimal values of hydrostatic stiffness. New L/D and C/R values could be implemented to increase the stiffness further. Finally, we note the accuracy of the modelling at $\pm 30 N/m$ when pinpointing both curves at the original geometry. This is due to an estimated correction to the rotor mass[6] when varying the geometries.

These design charts might prove useful, upon matching these theoretical models with experimental data, when considering a modification to the current MicroBearing geometry. This is especially so if the intent is to extend the operational range of the hydrostatic mode, when faced with the larger imbalance effects at higher rotational speeds.

2.4 Further remarks on Hydrostatic Modeling

A variety of different considerations on the theoretical work of a hydrostatic journal bearing is summarized here for possible future development. These considerations are also helpful

[6]We separated the rotor mass in a blade mass and a journal mass, of which the journal mass varies with the geometric parameters of interest

when operating the MicroBearing device experimentally, or when redesigning the journal bearing.

Larson and Richardson theory A stability criterion is suggested by Larson and Richardson in the work of externally-pressurized gas-lubricated bearings [38]. It is proposed that the tangential stiffness in the hydrostatic operation is insufficient to counteract the destabilizing effects of hydrodynamic whirl, a concern when the whirl component in the bearing reaction becomes increasingly important with larger rotational speeds. A simplified analysis by Larson and Richardson results in the stabilility criterion as

$$R_{whirl} = \frac{W}{W_n} = 2 + \frac{(\tau_1 - \tau_2)k_s}{k_{hd,t}} \tag{2.5}$$

where R_{whirl} is the whirl ratio, τ_1 and τ_2 the time lag constants as modeled in Richardson [61], and $k_{hd,t}$ the hydrodynamic tangential stiffness. Here we note that, in inherently compensated bearings, τ_1 is greater than τ_2 and that Richardson had obtained approximated solutions and experimental correlations for these time constants. The resulting whirl ratio is always greater than two, increasing with a larger inherent damping (of a hydrostatic bearing) that increases $(\tau_1 - \tau_2)$. The presented stability criterion is also consistent with their observations that increasing the hydrodynamic tangential stiffness $k_{hd,t}$ reduces the stability. This informs us of potential instabilities when reaching a whirl ratio of two during experimental operation, and that increasing the inherent damping in our hydrostatic journal bearing would improve the stability limit. The highest whirl ratio recorded in their paper is between 5 to 6.

"Lock-up" phenomenon In a 1972 MTI[7] publication by Vohr [42, Chap 5.5], a phenomenon of "lock-up"—in hydrostatic journal bearings with orifice feeding—is also mentioned. Vohr observed "a sudden forcing against the bearing wall when the journal ec-

[7]Mechanical Technology Incorporated.

centricity reaches a certain value" and quotes this value as less than 0.4 eccentricity, or a maximum of 0.5. While Vohr did not append his experimental results, he suggests two reason for this "lock-up" phenomenon that deals mainly with the feeder holes. (This danger of "lock-up" is also believed to be present in hydrostatic thrust bearings by Cheng [42, Chap 5.3].) However, we believe it is also possible for this "lock-up" behaviour to be caused by the imposed sideload exceeding the load-capacity of the hydrostatic journal bearings. Nevertheless, this might warrant a caution in attempting to transit from a hydrostatic operation to a more stable hydrodynamic mode, when the hydrostatic stiffness is insufficient at larger eccentricities.

Inertia effects For our MicroBearing device, the inertia effect can be relatively significant, with the inertial parameter χ approaching order unity—on a similar order of magnitude as the pressure and viscous terms. Much of the hydrostatic design in MTI (as well as hydrodynamic design) is based on negligible inertia forces on its computation [42, Chap 5.2]. Support for neglecting the inertia term, and hence allowing us to employ the cited hydrostatic models, is brought forth by Piekos with his "Bearing Analysis Suite for Investigating Common Simplifications" modeling. It is also presented by DiPrima and Stuart, Nataraj *et al.*, and Banerjee *et al* [57, 17, 52, 3]. It was noted by these authors that order-unity inertial parameters, for incompressible[8] flow, have negligible effects on bearing performance.

Annular Pressure Seals and the "Lomakin" effect Lomakin first explained the large direct stiffness found in pumps seals. A closer look into these seals reveal a similarity with our plain cylindrical journal bearing conditions—a larger than usual clearance, and a large pressure drop across the length of the journal bearing. The flow becomes highly turbulent and thus the Reynolds equation inappropriate for estimation [11]. Childs(1993) presented an analysis initially derived by Nelson(1985), beginning with the continuity, axial momentum balance, and angular momentum balance equations. The large direct stiffness,

[8]We treat the journal bearing as incompressible flow because of its very small L/D ratio, allowing for large side leakages.

briefly restated here, is accounted for by the combined effect of the inlet loss and the axial differential pressure gradient. Childs also reported possible fully developed flow in seals after only three hydraulic diameters and seals becoming destabilizing for rotational speeds slightly above twice the whirl natural frequency.

Also of mention is the need to decrease the average tangential velocity (which is roughly proportional to the cross-coupled stiffness term that is destabilizing). Methods to decrease this velocity, and hence increase the direct stiffness, are in a roughened stator or in "swirl brakes" that are reported in turbopumps. Finally, Childs presents examples of stiffness variations with axial differential pressure and rotational speeds. Given that our journal bearing geometry is similar to that of the annular seals reported and operated at low eccentricities about a centered position, it seems favourable to employ the existing modeling on annular seals for our hydrostatic journal bearing operation.

Chapter 3

Hydrostatic Journal Bearing: Experiment

Physics constitutes a logical system of thought
which is in a state of evolution... The justification of the system
rests in the proof of usefulness of the resulting theorems
on the basis of sense experiences, where the relations of the latter to the former
can only be comprehended intuitively.
—A.E., Out of my later years

This chapter presents experimental work on the MicroBearing device. We begin with the current fabrication challenges, highlighting improvements to a high aspect ratio journal bearing, minimizing the DRIE[1] non-uniformity, and achieving critical dimensions for the hydrostatic thrust bearings. The next section then summarizes the pre-testing procedure—flow testing and freeing the rotor—to characterize the thrust and journal bearings. Actual testing and operational results of the MicroBearing is next discussed. In understanding the instability of the hydrostatic journal bearing operation, we looked into determining the whirl natural frequency and its effects. We end this chapter with a summary of the causes for failure and suggestions for further development of the hydrostatic journal bearing.

[1]Time-multiplexed Deep Reactive Ion Etching.

3.1 Fabrication challenges

The fabrication of the MicroBearing rig involves 5 wafers and at least 13 masks—a complex system with regards to alignment, process development on each wafer and, indeed, achievability of the entire fabrication process flow. Lin [40] demonstrated the first successful fabrication. Figure 3-1 shows the general layout of the wafers involved.

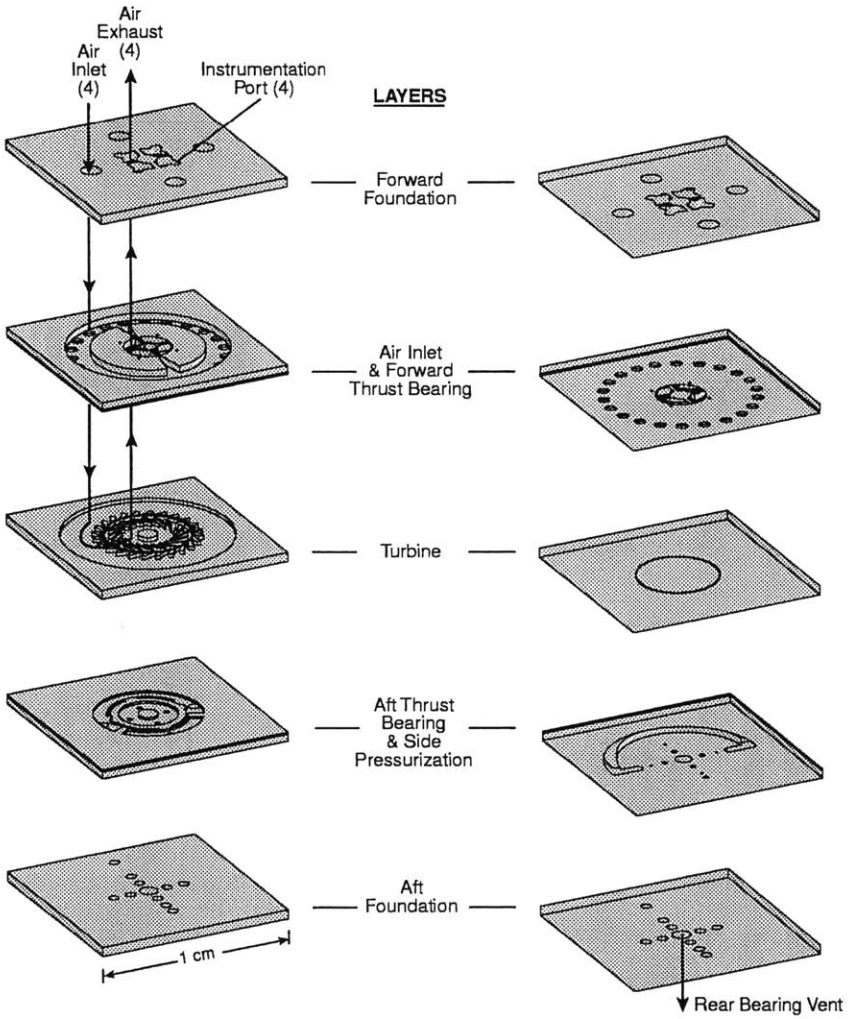

Figure 3-1: Exploded overview of the 5 wafers involved in the MicroBearing rig. The left column shows the top view; the right column the bottom view. Drawing is to-scale at 15mm on the edge of each die. (Lin, [40])

Developments of the MicroBearing fabrication process has challenged several limits in microfabrication, with significant contributions from Lin [40], Frechette [31] and Zhang [76]. In this section, we shall discuss the reducton of die-level etch depth non-uniformity with 65% etch wetted area[2] [2, 46], DRIE for a $300\mu m$ journal bearing at an aspect ratio of 30 and tapering of less than $0.5\mu m$, and consistent fabrication of $10.0\mu m$ through-holes as nozzles for the hydrostatic thrust bearings. In addition, we list in Appendix B.3 the crucial dimensions which have to be achieved for the MicroBearing device in order for successful spin-up operation. We began with the reduction in etch non-uniformity.

3.1.1 Etch non-uniformity

Etch non-uniformity of the blades (Figure 3-2) at the wafer-level results in an imbalance across the devices. Typical DRIE in our process result in the center [3] dies having shallower etches than the edge dies. A wafer-level etch non-uniformity in the shape of an inverted bow translates, at the die-level, into a slight difference in the blade height from one side of the rotor to the other. This causes the center of mass to be misaligned with the geometric center and hence an imbalance—an especially crucial issue for high-speed rotating machinery.

We studied the effect of etch recipes on etch non-uniformity by varying the rate of etch product removal and etch rate[4]. The compiled results are listed in Figure 3-3 for optimization of the etch conditions. Recipe 5[5] was chosen for the minimum etch variation. Note that there is significant reduction in edge die variation, with also slight reductions on the center dies. The real device etches are done with this recipe, though the final device etches had slight variations from the test etches. With the die-level etch non-uniformity reduced down

[2]Approximately 64.8% (146 mm^2 out of 225 mm^2) for die-level and 22.5% (1750 mm^2 out of 7770 mm^2) at the wafer-level is exposed.

[3]"Center" dies are denoted as the devices on the central region of the wafer and "edge" dies as closer to the edge of the wafer. There are four "center" dies and eight "edge" dies on each wafer.

[4]In collaboration with Dr. Xin Zhang of Microsystems Technologies Laboratories.

[5]Performed with the Surface Technology Systems DRIE machine, this recipe used an electric power of 8W and a APC angle of 61°.

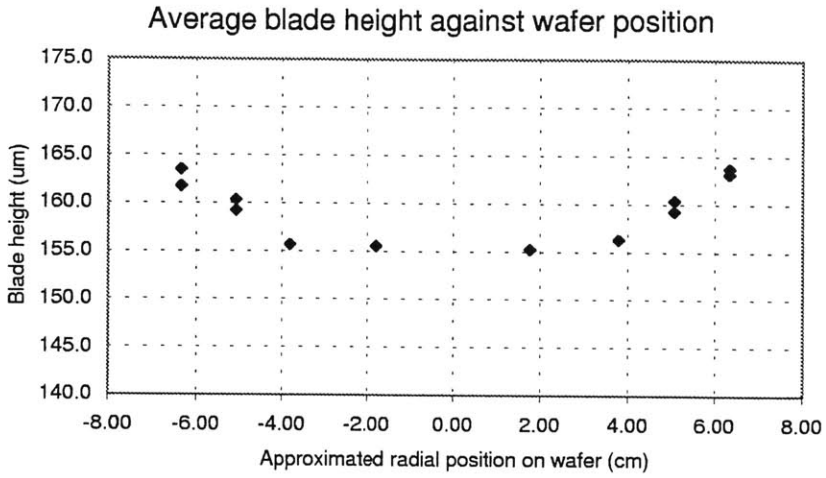

Figure 3-2: Measurement depicting the deep etch non-uniformity across a sample wafer.

to approximately $\pm 0.25\mu m$ for the center dies, Jacobson predicted[6] an imbalance of 4% for the MicroBearing device [35].

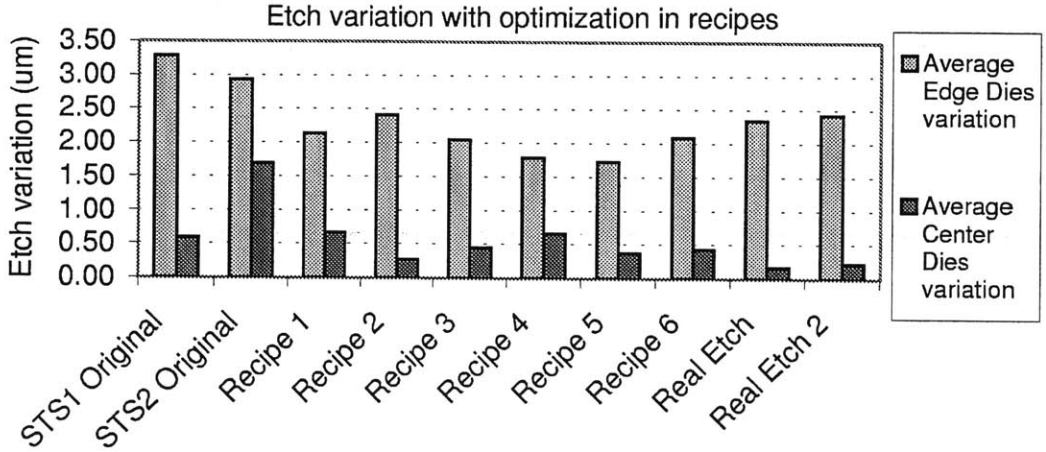

Figure 3-3: Average etch non-uniformity across devices with different etch recipes.

We note here that the process has been further improved by Tom Takacs and Dennis Ward for the MicroEngine [67]. They perceived that allowing more diffusion of reactants

[6]This computation is for a $\pm 2\mu m$ misalignment, total thickness variation of $3\mu m$, and asumming complete removal of the tabs binding the rotor.

and products would lead to a more uniform etch surface. This is made possible through reducing the number of dies on each wafer and positioning the dies near the edges of the wafer for better diffusion at the wafer center.

3.1.2 Journal bearing wall

In the previous builds, the journal bearing had a significant tapering of above $10\mu m$ along the $300\mu m$ etch depth of the journal [31]. This is highly undesirable for our journal bearing operation, especially in the hydrodynamic operation where the journal eccentricities have to be brought above 0.8. The fabrication team was able to optimize the time-multiplexed DRIE to produce an approximately straight journal wall with a tapering of less than $0.5\mu m$ for an etch depth of $300\mu m$ [2]. This is shown in Figure 3-4. Current requirements of the MicroEngine necessitates deep-etches in the range of $500\mu m$.

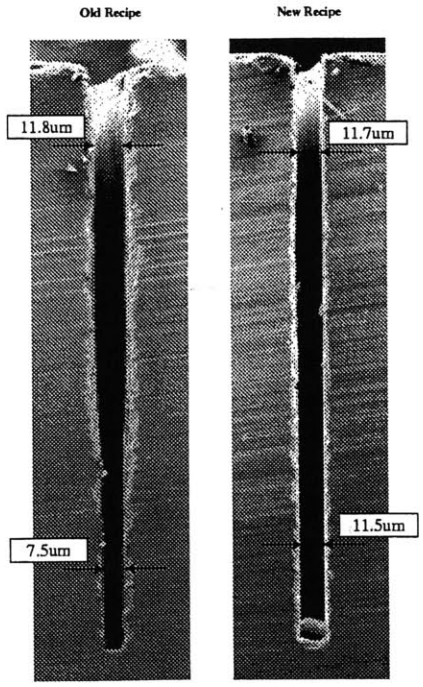

Figure 3-4: Optimization of the DRIE process to create a straight edge journal bearing wall. The etch depth is $280\mu m$ on the left figure and $315\mu m$ on the right. Courtesy of Zhang [46].

Nozzle diameter	*Length of nozzle*	*Total thrust bearing gap*	*Derived stiffness*
$10.0\mu m$	$100.0\mu m$	$3.0\mu m$	$370{,}326N/m$
$11.5\mu m$	$100.0\mu m$	$3.0\mu m$	$266{,}843N/m$
$12.8\mu m$	$100.0\mu m$	$3.0\mu m$	$201{,}130N/m$
$10.0\mu m$	$100.0\mu m$	$2.0\mu m$	$169{,}106N/m$
$10.0\mu m$	$100.0\mu m$	$4.0\mu m$	$465{,}220N/m$
$10.0\mu m$	$50.0\mu m$	$3.0\mu m$	$315{,}871N/m$
$10.0\mu m$	$150.0\mu m$	$3.0\mu m$	$414{,}446N/m$

Table 3.1: Hydrostatic stiffness at different configurations. The first line describes our desired design choice.

3.1.3 Hydrostatic thrust bearing nozzles

In the hydrostatic thrust bearing, the desired nozzle diameter stands at $10.0\mu m$. Fabrication of these nozzle diameters precisely is difficult, given the aspect ratio of approximately 10 at the etch depth of $100\mu m$. Variation of nozzle diameter away from the design value results in large changes in stiffness, as modeled in Table 3.1. The results are computed from a model developed by Jacobson [35] and Figure 4-1 depicts the model conceptually. Equal forward and aft thrust bearing geometries are used, except for the exit radii of the thrust bearing flow (which stands at $700\mu m$ for the forward and $900\mu m$ for aft thrust bearing). The inlet temperature is taken at 300K and the number of nozzles modeled at 20.

In an earlier build of the MicroBearing devices (Build number 3), we have an average nozzle size of $12.8\mu m$, resulting in a predicted 46% drop in stiffness. In fact, this led to a thrust bearing failure during testing as brought out in Section 3.5. In the next MicroBearing build thereafter, we thus toleranced the nozzle size tightly to the $10.0\mu m$ design value and the thrust bearings were able to function well even during high speed operation.

3.2 Pre-testing

Pre-testing involves static flow testing, releasing the rotor, free flow testing and calibration of the instruments. A checklist for preparing the MicroBearing rig for testing is provided in Appendix B-12. These flow tests are imperative to gauge the characteristics of the thrust and journal bearings.

3.2.1 Static flow testing

Static flow testing gives us a measure of the similarity between the Low/High plenums[7]. Built to be identical within the limits of microfabrication, the flowrates are similar since the Low and High piping (of the device packaging) are of equal length. Figure 3-5 shows a summary of the journal bearing flowrates. At a journal bearing pressurization of 10.0 psig, the maximum discrepancy of the flowrates are on the order of 25-30 sccm[8] across a device. Across devices within a wafer build, the variation could be up to 100 sccm. The small discrepancy within each device suggests that the channels fabricated within each device (including the journal bearing) and the packaging leading up to the device are acceptably identical for hydrostatic operation. This reduces the likelihood of differences in packaging and channels within the die causing the device to crash.

Static thrust bearing flow testing, however, has larger flow discrepancies, especially on the forward thrust bearing. Figure C-1 in Appendix C.1 shows the respective flowrates. Note that the aft thrust bearing flow varies only slightly, compared to the forward thrust bearing[9].

[7]The journal bearing is divided into two plenums, termed here as "Low" and "High", that allow for side-pressurization external loading in light of the low mass of the rotor.

[8]This translates to approximately 8% of the total flow at 1 million rpm.

[9]The cause of the large variation in the flowrate has not been determined, although it is suspected to lead to the leaky forwardthrust bearings often observed

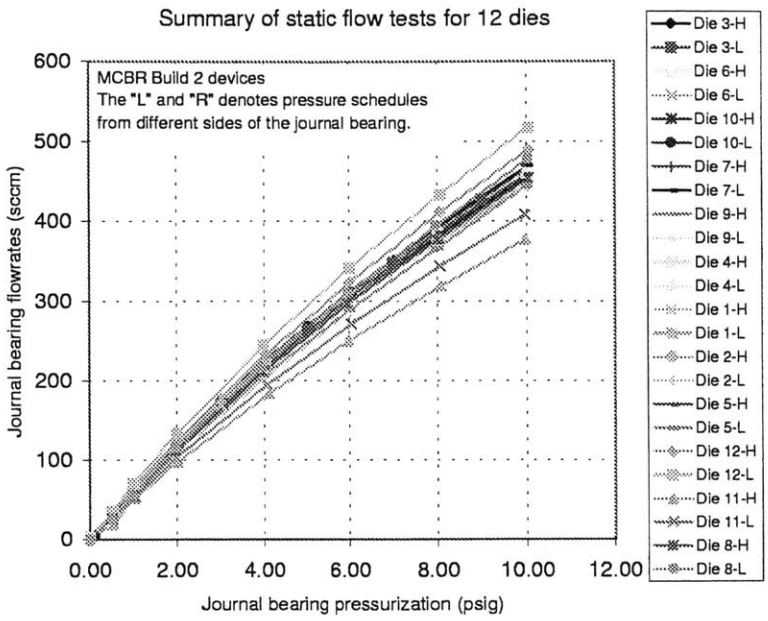

Figure 3-5: Summary of static journal bearing flowrates, depicting the slight variations across each die.

3.2.2 Tab break-off

With deep reactive-ion etching of the journal bearing, the rotor would simply fall off if it is not attached to another level when the journal is created[10]. We used an approach developed by Frechette [31] to bind the rotor to the second wafer level by four pillars of $76\mu m \times 50\mu m$ rectangular dimension. Figure 3-6(a) shows a topview SEM of the location of the tabs with the pillars underneath. Several variants of this "tabs-to-rotor" approach was pursued—Lin [40] used a laser-assisted procedure to remove the tabs, and Frechette [31] (our current design) had the tabs reduced in size, in an effort to reduce the imbalance, and mechanically broken off with silicon micro-needles. Figure 3-6(b) shows the insertion of a micro-needle through the main exhaust of the turbine to break off the tabs, releasing the rotor.

[10]A handle-wafer approach (with gold deposited as foundation plates) to hold onto the rotor was pursued by Lin, but found to have low yield after the thermal compression fusion bonding. All-silicon wafers builds have since been pursued in the MicroBearing device, though a tabless build could still be possible by just manually popping in the rotors (while watching the appropriate cleaniness and matching the dies) before thermal compression. Other devices, such as the turbocharger in the MicroEngine program and the turbopump in the MicroRocket program, are using a sacrificial oxide layer to hold onto the rotor during fabrication before oxide removal to release the rotor.

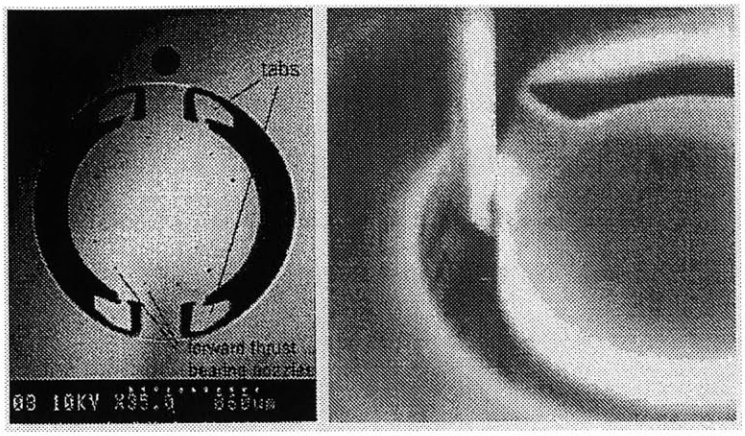

Figure 3-6: (a) Topview SEM of wafer with tabs underneath, holding onto rotor, (b)Insertion of micro-needle to break off tab, freeing up rotor for operation.

This "tabs-to-rotor" approach works well and the released tabs (approximately of $380\mu m$ x $150\mu m$ size) are shown in Figure 3-7, after having fallen out of the die when broken off. We see here that, despite the silicon fusion bonding between the pillars and the top of the tab (signified by the triangular piece), the point of breakage often lies near the bottom of the pillar. This is helpful in reducing the imbalance caused by the mass of the pillar remaining on the rotor[11].

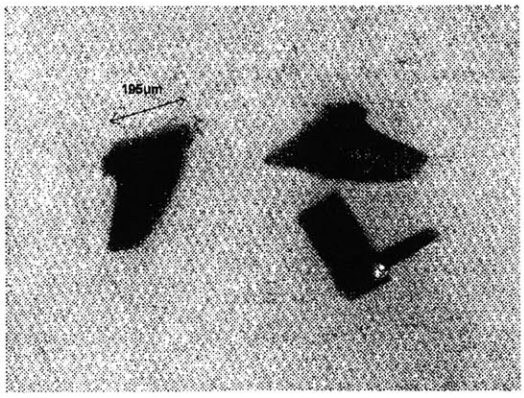

Figure 3-7: Released tabs of the MicroBearing rig.

[11]In attempting to improve the imbalance on the rotor, there is also the consideration on the fabrication of a "tabless" rotor, wherein the rotor is manually placed into the bearing prior to final wafer bonding. However, the manual placement of the rotors might result in contamination of the bonding surface just prior to bonding. The tab residue is also believed to not contribute strongly to the imbalance [35].

3.2.3 Free flow testing

Free flow testing[12] of the devices gives us comparison information on the characteristics of the device. Especially helpful are the thrust bearing flowrates which permits an understanding of the nozzle sizes, the thrust bearing gap size, and the axial position of the rotor for a given set of flowrates. Figure 3-8 shows the typical thrust bearing flowrates for a single device. A summary across the dies is listed in Appendix C.1.

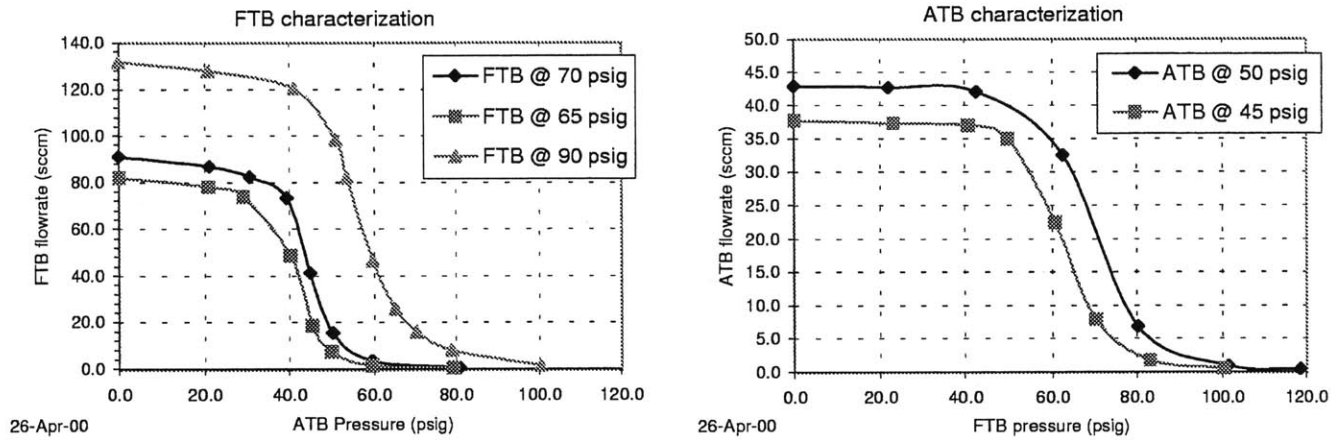

Figure 3-8: Sample flowrates characterization of thrust bearings for a released rotor. This flowrates are obtained from device MCBR 4-9. 'FTB' denotes the forward thrust bearing and 'ATB' the aft thrust bearing.

3.3 Experiment

This section describes the experimental setup of the MicroBearing rig, along with actual test results of the device. Included are different variants of the current setup, with descriptions of the data acquisition system and the speed sensor instrumentation. The operational results are summarized, with tip speeds up to 303 m/s, in this section and analysis of the results covered in Section 3.4 and 3.5.

[12] "Free flow testing" refers to flow tests when the rotor is free and able to rotate.

3.3.1 Experimental set-up

Packaging Packaging of a microdevice is often surprisingly difficult. The package of the MicroBearing rig was built by Victor Dubrowski, James Letendre, Lin [40] and Fréchtte [31] and is illustrated in Figure 3-9. The flow paths for the journal bearing and the main turbine air are as labelled. Here we note there should be equal pressure drops across the Low/High plenums in order for precise control of the bearing load, and hence the length of these two pipings were matched carefully. We have also experimented with piping both Low/High journal bearing plenums on a single valve, to strictly enforce an identical pressurization on both plenums for a purely hydrostatic operation mode. This scheme seems to have worked well for our operation, though if any side-load does appear[13], we would not be able to actively zero it out.

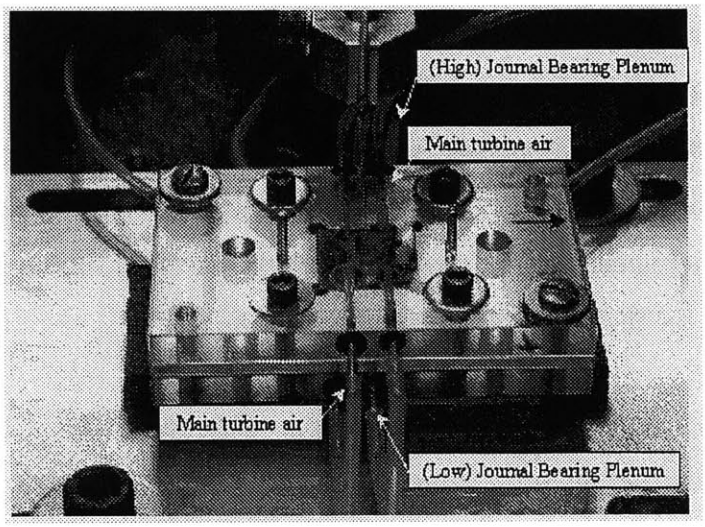

Figure 3-9: MicroBearing device in package, ready for experimental testing.

Electrical Control of the flowrates With MKS Type 1179A mass-flow controllers built into the system, the flowrates can be set with voltage input signals. This was implemented

[13]We certainly do not expect any with a single pressure source.

for the main turbine flow as a method for the MicroBearing to be spun up directly with command-inputs from the computer interface. A 10kΩ 10-turns potentiometer for a supply voltage of 5V was currently used to control the input signal. While potentiometer control was also intended for precise control of the rotational speed, the mass flow controller response time of 2 sec[14] by a simple PID controller is likely be the cause for slight time-variant responses in the speed initially, even though all other pressures were kept constant. The Low/High plenums are also equipped with mass-flow controllers for electrical control of the journal bearing flowrates (if desired) during the spin-up operation.

Speed sensor To measure the rotational speed and its subharmonic components, a fiber optic displacement sensor is employed. It was initially put together by Lin [40], Fréchette [31] and Jacobson [35]. Commercially made by Philtec[15], the laser diode puts out a 670nm light source at a maximum power of 0.5mW. Changes in displacement of the surface (such as when a 150μm raised height passes underneath, with an additional 150μm of fixed clearance) effects the signal output. For our frequencies in question, the displacement resolution stands at 0.5μm for the far field and 0.035μm in the near field[16]. The results achieved for our 150μm blade had a change of about 1.0V to 1.5V detected. Though somewhat less than the 2V stated in the product specification, this is enough for us to do the signal post-processing since our noise-level is on the order of approximately 50mV.

Data Acquisition Our data acquisition is written with LabView^{TM} 5.0, and takes data at 1.25MHz and 1kHz on two separate computers. The 1.25MHz data acquistion records the Philtec speed sensor signal, enabling us to postprocess the signal for rotational speed and its harmonic components (Section 3.4.2).

The 1kHz data is, however, averaged every 200 datapoints[17], displayed and stored onto

[14]Product specified as < 2 sec for within 2% of the setpoint. 2% of the setpoint could translate to 400 sccm in a 20,000 sccm flow controller.

[15]We employed model number D6-A1BMTV+L+H.

[16]Near field for our device is 27.9 to 63.5μm and far field is 182.9 to 617.2μm

[17]Averaging was done to reflect an accurate current picture and to avoid a massive set of data accumulated

file at 5Hz. Averaging of the data is performed only on the mass flowrate and pressure sensor measurements which have a slower time response, and not on the speed measurements. Speed measurements through the Philtec are also displayed on a spectrum analyzer, from which we can detect the harmonic resonances of the device during operation.

We would like, however, the 1kHz datapoints to be stored into a buffer such that any sudden effects onto the MicroBearing could be recorded just before any crash. This buffer of the previous few seconds (at 1kHz) can later be investigated to determine a cause of failure, if any. To ensure timely recording, the trigger for this buffer should be deployed in the software—a trigger that would activate automatically when a certain parameter (for example, rotational speed) decreases dramatically.

Two methods[18] are possible to implement the buffer for the last few seconds of 1kHz data—using two separate matrices, or using shift registers from LabView.

In the first method, the concept is to write the desired 5 secs of data between two matrices A and B such that neither is empty at any one time. This method, as in the second, avoids as much manipulation of matrices as possible, as LabView is relatively unwieldy with large matrices. This is illustrated in Figure 3-10. We begin with filling of matrix A. When matrix A is filled, the incoming data is channeled into matrix B. When matrix B is then filled, we empty matrix A and began filling it again. In this way, we will have at least one set of previous data in either matrix A or B. Having the advantage of taking up less run-time memory over the second method, we went ahead to implement this. However, upon experimentation, we discovered that the implemented control structures (needed to determine when either matrix is full, and to reset the matrix) also takes relatively large computational resources[19].

The second approach was found to work satisfactorily. Usage of a "shift register" pushes

after every run.

[18]Another method which we tried and did not work was to have two separate AI_Read sub VIs to extract the data out of the already in-built buffer. However, we later found out that the in-built buffer only strings out data in future time—to build up a buffer of previous time, we would still have to concatenate the data ourselves.

[19]This is because we cannot overcome the condition that the VI has to check the current matrices density in EVERY loop before moving on to the other matrix.

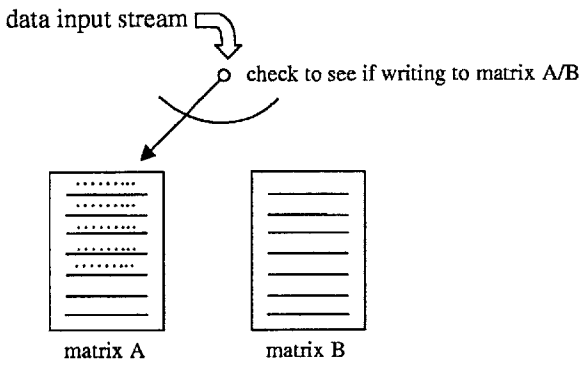

Figure 3-10: Concept of using a dual-matrix to implement previous-time buffer. The data input stream fill ups one matrix and then swtiches to the other when the first gets full. This continues to be processed between the two matrices such that neither one is empty at any one time.

every data set into another matrix that is temporarily stored. We repeat this shifting for a total of 5 secs of previous data, and concatenate the data into a large matrix only when we need to write out this data. This is briefly illustrated in Appendix B.5. The appended layout shows the general structure, without the details, of the data acquisition modules.

We note the additional "shift registers" were able to process the data without much computational cost. As the purpose of the implemented buffer is to record sudden actions in the crash data, there is no need to extend the buffer to more than 5 secs, although this is certainly possible. Next, we included the switches onto the buffer. A "safety" switch was first added such that the triggering will not occur under any conditions if the "safety" switch is off. This is to cater for wild fluctuations in measurements when the experiment just started, or when resetting the data acquistion program. With the "safety" switch activated, the 1kHz data acquisition will then occur when the tracked value falls below a pre-determined percentage, or when the user deliberately desires the data acquisition. We set the detection of a crash as a 90% drop from the current rotational speed and the results work well. We were able to record a 1kHz 5 sec data sample just before the crash, without any detectable slow-down on the data acquisition system.

3.3.2 Operation of the MicroBearing rig

With the hydrostatic journal bearing mode not as well modeled as the hydrodynamic counterpart, operation of the MicroBearing rig relied heavily on previous experimental work. Running a post-operation analysis on previous MicroBearing devices that failed, Jacobson suggested a parameter—$\frac{Rotational\ Speed}{(Axial\ differential\ pressure)^n}$—that should be kept approximately constant. Quite logically, this is the comparison of the excitation load (related heavily to the rotational speed) to the load capacity of the bearing (denoted by the axial differential pressure across the journal bearing). At low speeds, we found a nondimensional[20] $\frac{Rotational\ Speed}{(Axial\ differential\ pressure)^{0.83}}$ at 0.12 empirically for ease of operation, and, at axial differential presssures above 1.0 psig, a non-dimensional $\frac{Rotational\ Speed}{(Axial\ differential\ pressure)^2}$ at 4.5[21]. This scheme worked well in getting our devices above 1 million rpm. We also note a region (usually with rotational speeds at 40,000 to 80,000 rpm) whereby subharmonic resonances appear frequently. This is because, on following our schedule, this is the regime when we are crossing the critical natural frequency. Upon crossing this region, however, we were usually able to reach operation above 500,000 rpm through a purely hydrostatic mode.

In employing the speed sensor, we process the frequency spectrums in real-time, through a spectrum analyzer, and Figure 3-11 shows a sample during operation. Occasionally at low rotational speeds, we detect additional peaks (as further discussed in Section 3.4) appearing on the spectrum. The appearance of these peaks suggest the whirling motion of the rotor—either due to vibrational excitation at resonance or an inversion of the rotor. Indeed, the appearance of these peaks, when severe enough in terms of amplitude, generally indicate the approach of a stability boundary.

Figure 3-12 illustrates a summary of the devices operating above 500,000 rpm. We note that a typical operation takes several hours, a length of time due to meticulous recording

[20]With rotational rate normalized by design speed and axial differential pressure normalized by ambient pressure.

[21]This translates to a dimensional $\frac{Rotational\ Speed}{(Axial\ differential\ pressure)^{0.83}}$ at $35{,}000 rpm/Pa^{0.83}$for axial differential pressures below 1.0 psig and a dimensional $\frac{Rotational\ Speed}{(Axial\ differential\ pressure)^2}$ at $50{,}000 rpm/Pa^2$ for axial differential pressures above 1.0 psig.

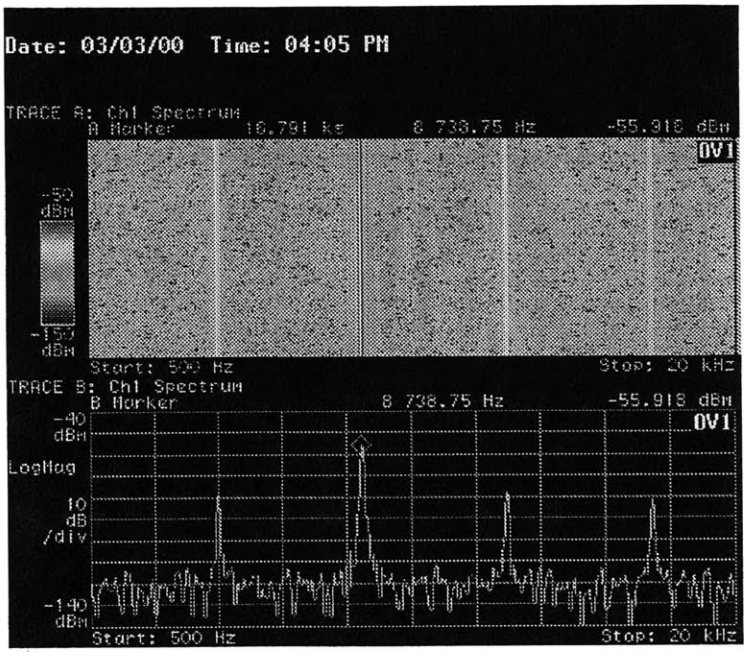

Figure 3-11: A sample frequency spectrum during operation, with rotational frequency at 4369Hz. The top viewgraph shows an intensity spectrum over time, while the bottom viewgraph shows a spectrum sampled at a particular time. With two speed bumps, twice the synchronous rotational speed often gives the strongest signal.

of experimental data for post-analysis, and that the devices are spun to the order of 10^8 revolutions. Acceleration of the turbine was shown in Lin [40] and Jacobson to not be a limiting factor[22]—hence it is conceivable for the device to spin up to the required tip speed in a much shorter time span.

In Figure 3-13, we also show the journal bearing flowrate starting from 30% of the main turbine flow at start-up and decreasing to 15% at high rotational speeds, suggesting that hydrostatic journal bearing operating mode might well be supported in the MIT MicroEngine, with a smaller decrease in cycle efficiency than initially perceived.

Due to the brittle nature of silicon, it is not unusual for the devices to fracture catastrophically upon crashing. This is especially so at rotational speed above 100,000rpm. At

[22]Rotor acceleration is experimentally shown to reach 60,000 rpm in 0.1sec by Lin [40],Section 4.2.2 and Chapter 6.

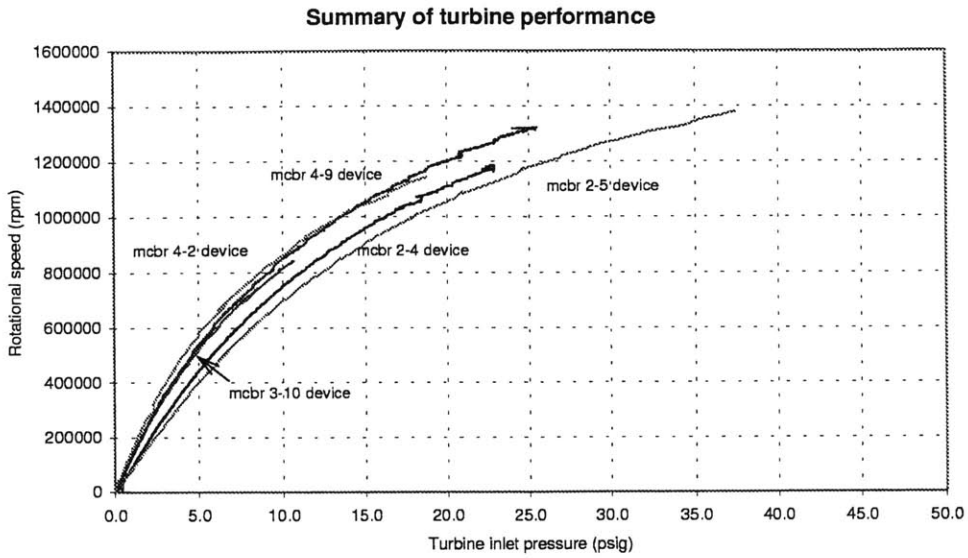

Figure 3-12: Summary of the spin-up of the MicroBearing devices.

lower speeds, multiple crashes or impacts against the journal bearing wall (as detected by rapid deceleration and acceleration in our speed sensor) often leads to drastically poorer performances such that these crashes or impacts occur more frequently and earlier on. This is due to chipping damage of the rotor at the journal bearing region. Figure 3-14 shows a device that broke into several parts, after a fatal crash at 1.33 million rpm.

3.4 The MicroBearing Natural Frequency

This section describes the determination of the MicroBearing natural frequency, in an attempt to avoid the whirl instabilities. We begin with a discussion of the physics of rotor whirling motion and rotor "inversion". This is followed by an analysis on the experimental frequency spectra. Effects of different factors on the natural frequency are presented. A waterfall chart is then presented, whereby we notice the appearance of a half-speed whirl. In operation of the MicroBearing rig, it is suspected that drifting away from the stable region bounded by the first and second-multiple natural frequency is the precursor to a device crash.

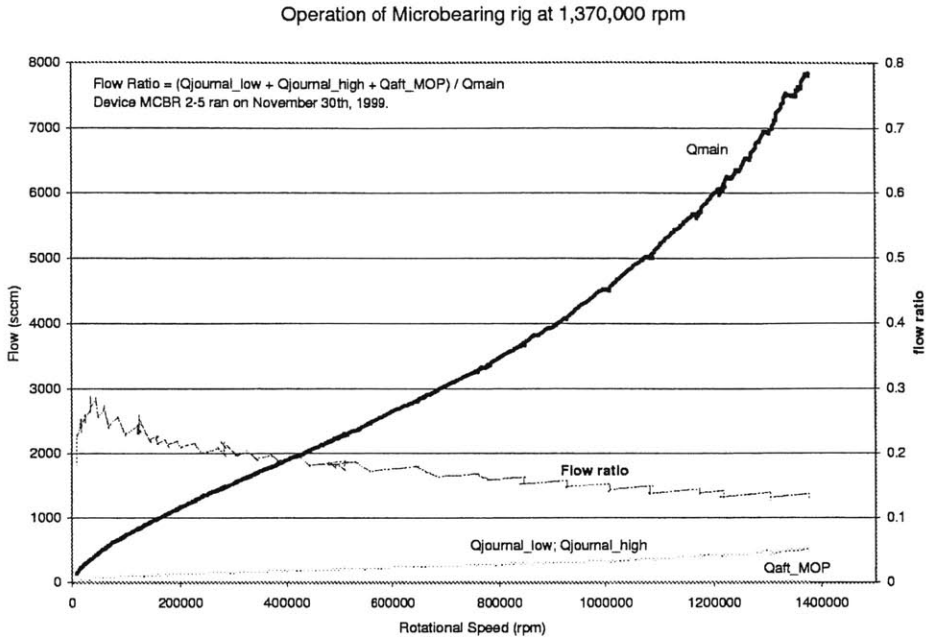

Figure 3-13: Respective flowrates of the bearings in a typical MicroBearing operation. The hydrostatic journal bearing flow ratio decreases as we increase up in tip speed.

3.4.1 Whirling motion

The motion of a rotor in a plain journal bearing[23], in a hydrostatic bearing mode, can be described in two states: (1) subcritical operation, in which the rotor rotates about the bearing geometric center, (2) supercritical operation, in which rotation occurs about the center of mass[24]. Supercritical operation, often termed "inverted" operation, occurs when the rotational frequency exceeds the journal bearing natural frequency.

In a subcritical operation, the causes of journal bearing crash failures is due to sideloads to the journal bearing. Examples are the rotational sideload from rotor imbalance, vibrational disturbances due to impact on the device, or an external sideload due to different pressures in the journal bearing. In a supercritical operation, however, the sideload leads to an additional whirl motion of the bearing geometric center. Figure 3-15 delineates this whirl motion. We see the orbiting of the center of mass around the bearing centeras depicted by the labeled

[23]Cylindrical, 360° around rotor, without any lobes.

[24]In the presense of imbalance, the center of mass is offset from the bearing geometric center.

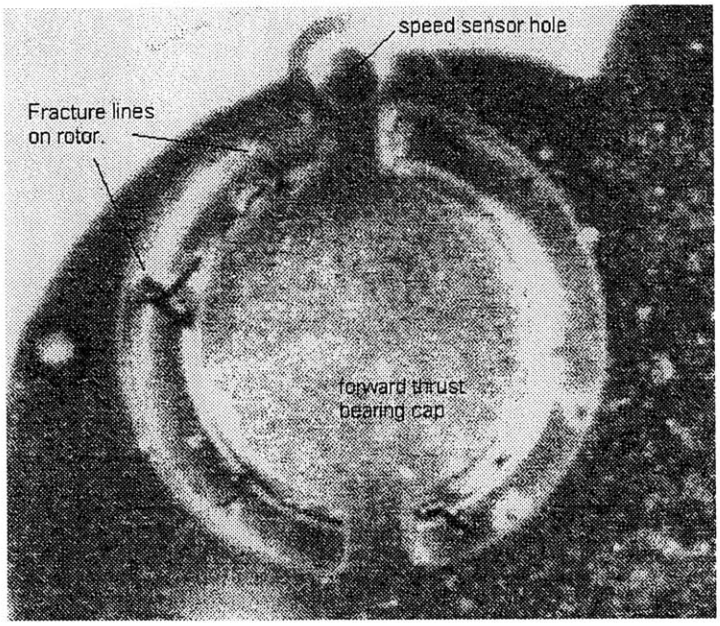

Figure 3-14: The aftermath after crashing at 1.33 million rpm.The rotor is visible under the main exhaust port and here we notice the fracture lines on the lines after a high-speed crash.

phases I, II and III. Causes of journal bearing failures, therefore, now includes the amplitude of this whirl motion, which we believe is strongly affected by the journal bearing natural frequency excitation. As we are typically operating in the supercritical regime, Section 3.4.2 is thus devoted to determining the MicroBearing journal bearing natural frequency.

3.4.2 Analysis of Power Spectrum

Determination of ω_n Detection of the natural frequency is made in real time with a spectrum analyzer[25]. However, to post-process the information at a higher accuracy and resolution also occasionally required high speed data[26]. Figure 3-16 shows a sample spectrum. It was postulated earlier by Ehrich that these frequencies can be generated from the sum and differences of the rotational speed,ω and the whirl natural frequency,ω_n [22]. This is generalized by Orr as the following Cauchy product [54]:

[25]Hewlett-Packard 89410A DC-10MHz Vector Signal Analyzer.
[26]As mentioned in Section 3.3.1, this data is sampled at 1.25MHz.

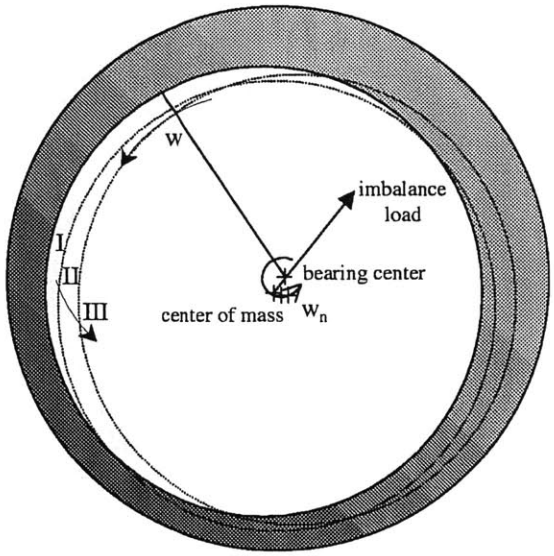

Figure 3-15: Supercritical whirl motion in a plain hydrostatic-mode journal bearing—'inverted' operation. Phase I, II and III depict the motion of the center of mass orbiting around the bearing center, which is fixed by definition.

$$\Phi = \left(\sum_{p=1}^{\infty} e^{ipW}\right) \times \left(\sum_{q=1}^{\infty} e^{iqW_n}\right) \times \left(\sum_{m=1}^{\infty} e^{imW_{n,hd}}\right) \times \left(\sum_{n=1}^{\infty} e^{inW_{v,hd}}\right). \tag{3.1}$$

where $W_{n,hd}$ is the hydrodynamic whirl frequency, and $W_{v,hd}$ the hydrodynamic vibration frequency. In a purely hydrostatic mode, the last two terms cancel out. The remaining terms express the boundaries upon crossing the nth-order harmonics of the fundamental natural frequency. By seeking out the fundamental at each axial differential pressure, we could conceivably avoid crossing the boundaries during operation.

In order to determine the natural frequency, W_n, we superimposed two spectrums—of which the rotational speed W is kept constant, yet with a sizable change in axial differential pressure. The frequency peaks which shifted must hence be dependent on this axial differential pressure change. Since increasing the axial differential pressure should increase the stiffness of the journal bearing and thus increases the natural frequency, the peaks that shifted to a higher frequency reveal the natural frequency. Figure 3-17 gives an example. Here we note the shifting of a certain set of peaks from the synchronous frequency upon an

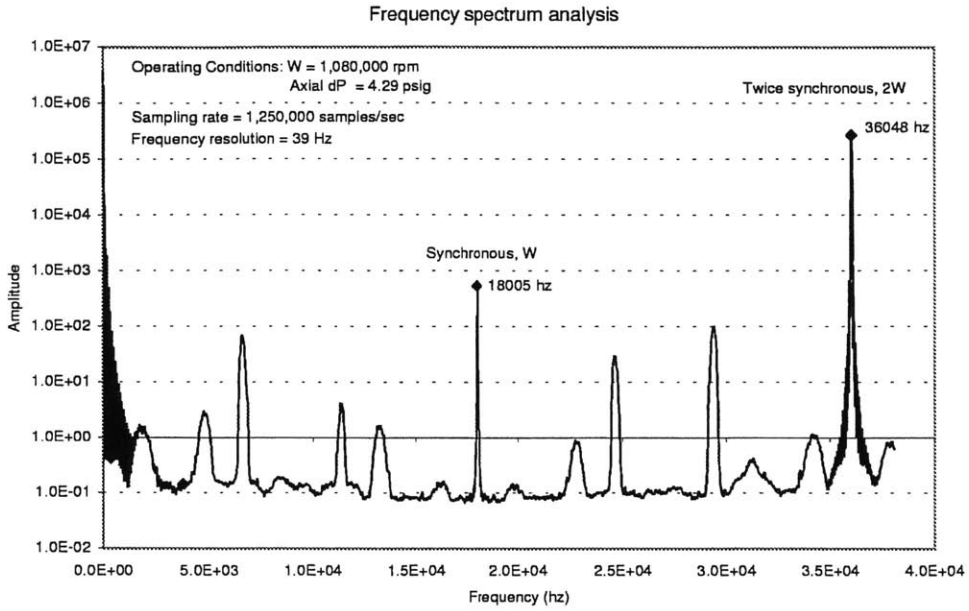

Figure 3-16: A sample Fourier spectrum during operation.

increase in axial differential pressure, suggesting a candidate for W_n. From this hypothesis, the rest of the spectrum can be recreated with higher-order harmonic responses. In fact, in these spectra, even the second-order harmonics is visible.

Figure 3-18 shows a replication of this phenomenon at about half the rotational speed. Again we notice the "sums and differences" in the harmonic response. An experimental matrix to determine the natural frequencies is repeated during testing to obtain a broad spectrum of data. As a sidenote, on some of our high-speed spectra, we observe a distinct shape to the frequency spikes that is mirror-imaged on the synchronous frequency. This could be useful as an additional check on our selection of the natural frequency.

Figure 3-19 sums up the whirl natural frequency for the range of axial differential pressure we have operated. This experimental data is accumulated over 4 of the highest-speed dies, from two separate builds. We noticed that the natural frequency increases sharply at above approximately 3 psig. While the natural frequency between the ranges of 3 psig and 5 psig is pretty well mapped out, the general trend of the natural frequency above 5 psig is still unclear. The theoretical models (Section 2.1), however, indicate no signs of the natural

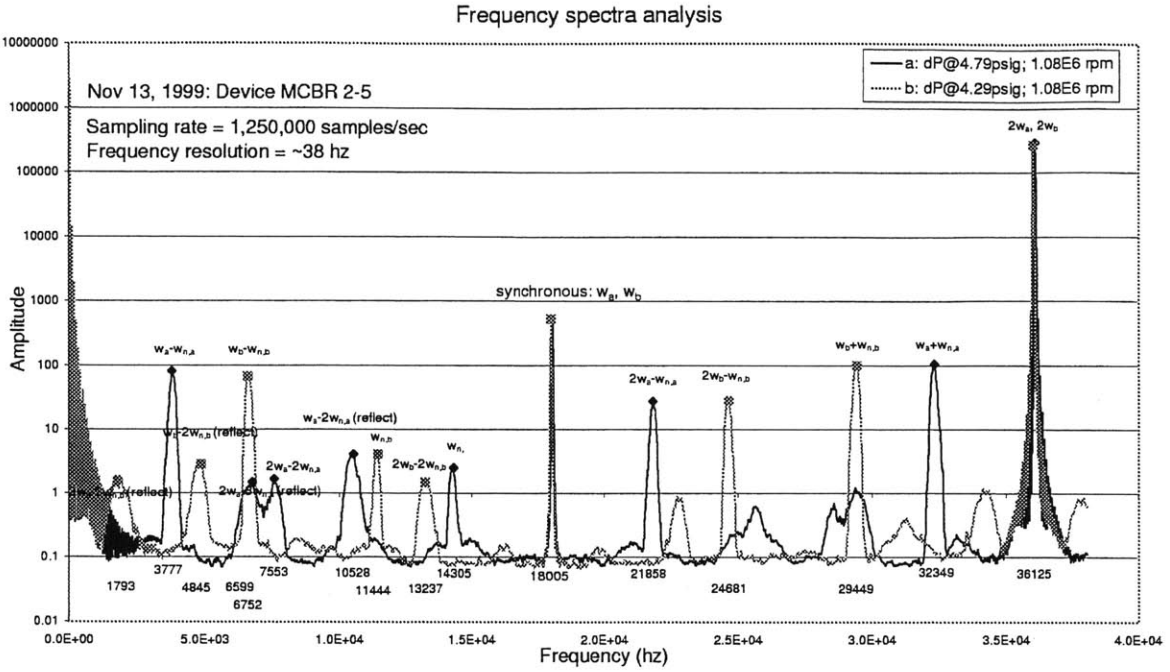

Figure 3-17: Determination of the MicroBearing natural frequency at 1.08 million rpm, with subharmonic resonances accounted.

frequency peaking off after a certain axial differential pressure. There are suggestions[27] of the natural frequency reaching a constant value between 4 to 5 psig. Finally, we point out that, within each die, there is a clear continous relation on the natural frequency; however, across different dies, the discrepancy could be as large as 2500 Hz.

[27]Brought up by Fred Ehrich.

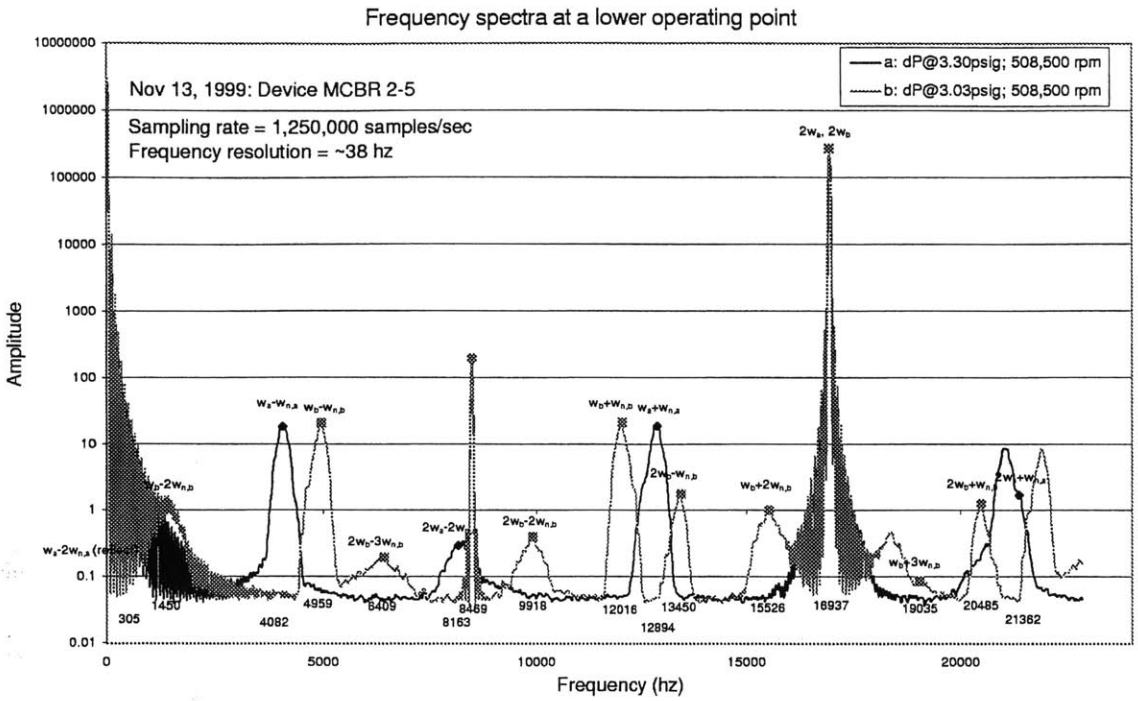

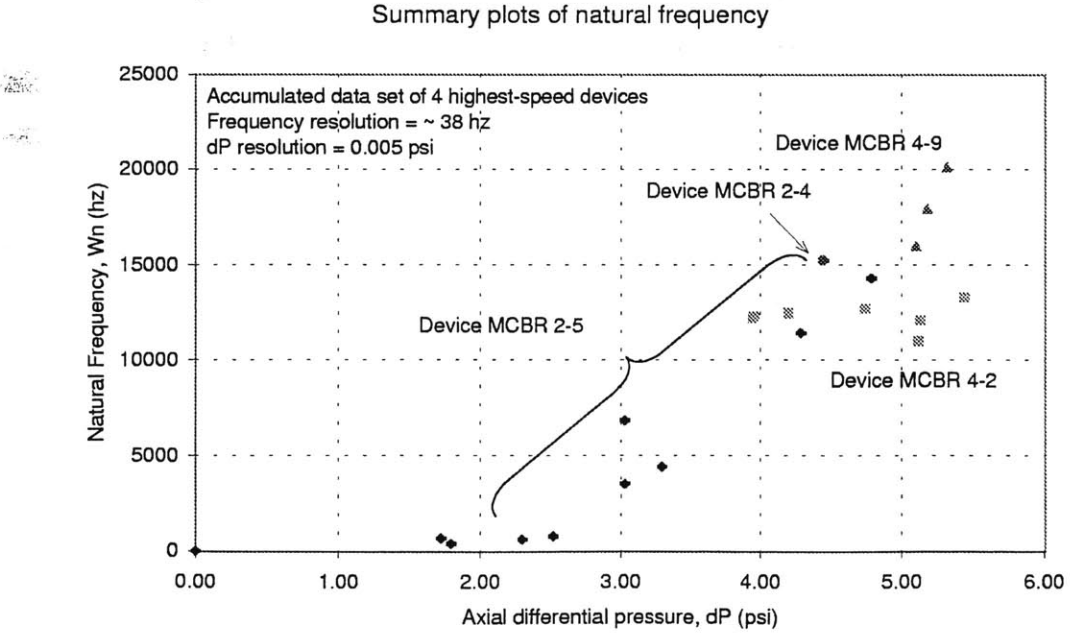

Figure 3-19: Natural frequencies summary of four highest tip speed MicroBearing devices, compiled from extensive data set. The different symbols represent natural frequency data taken from different devices.

Effects of rotational speed on W_n Theoretical considerations (Section 2.2) of rotational speed effects on W_n suggest the axial-through flow is weakly affected by the rotational motion. However, the experimental data at 508,000rpm, as shown in Figure 3-20, suggests the natural frequency is strongly affected by the rotational speed. With the speed increased on the order of 10%, the natural frequency almost halves. At speeds above 1 million rpm, however, we did not see this strong effect, though there is still a slight decrease in the natural frequency. This is at least consistent with the Coney and El-Shaarawi trends, where a larger change in stiffness is observed at lower rotation rates (as per Figure 2-2). This could perhaps be explained by conceptualizing the journal bearing flow as two independent degrees of freedom: an axial-through flow and a rotational flow. At lower speeds, such as at 477,000rpm, the journal bearing axial-through flow is smaller[28] because we do not require a large axial differential pressure. Increases in the rotational rate (by approximately 31,000rpm) will lead to the journal bearing flow traversing more rotations prior to exiting axially. However, at larger speeds, such as at 1 million rpm, the axial-through flow is larger[29] and similar increases in the rotational rate will lead to a smaller increase in the number of rotations prior to exiting the journal bearing. This therefore leads to a smaller change in journal bearing characteristics at higher speeds.

Other effects on the W_n Supplementary to the major effects of axial differential pressure and rotational speed, we observe a small time-dependence of the natural frequency. In Appendix C-4, we show the resulting two spectra at the same operating conditions, but with one taken after leaving the device running for another 3 minutes. This shift in the spectra, while small (on the order of 3%), could suggest a thermal effect that changes the fluid density and viscosity, and a possible damping effect of the bearings. Without measurements of the rate of the spectra shift, however, it is difficult to determine the cause of the shift as thermal or mechanical.

[28]The axial flow velocity is estimated to be at 45m/s for the necessary axial differential pressure, as derived in our operating schedule, needed in the journal bearing.

[29]This is estimated to be at 70m/s.

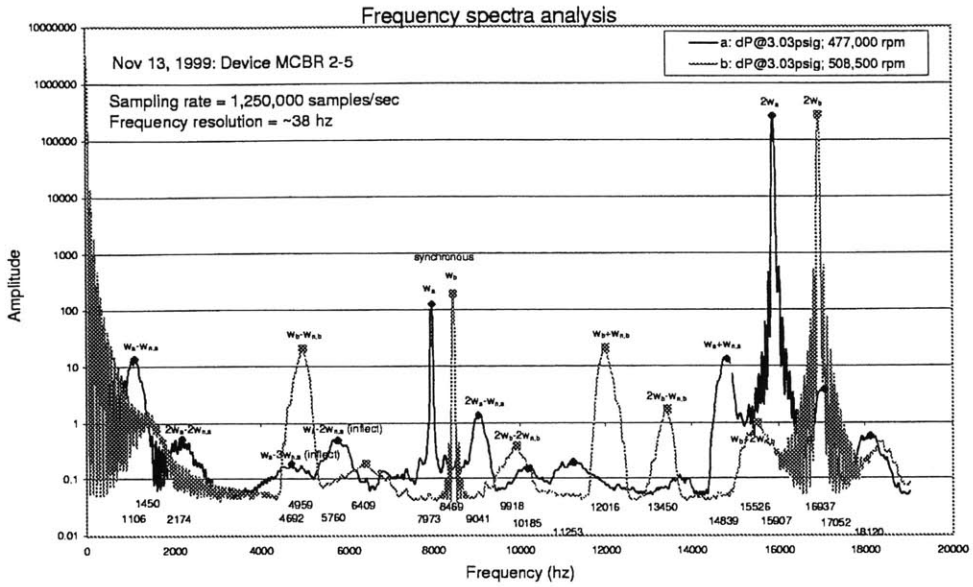

Figure 3-20: Effects of rotational speeds on MicroBearing natural frequency. The increase in rotational rate leads to a sharp decrease in the natural frequency.

Moreover, the flow exit from the main exhaust of the MicroBearing can excite vibrations on the speed sensor, leading to a deceptive frequency content on the spectrum. We thus physically load the speed sensor against the entry hole to damp out this vibration and, undoubtedly, we see the disappearance of this extraneous frequency on the spectrum. The effect of loading the speed sensor is portrayed in Appendix C-5. In obtaining the high-speed data for analysis, we took careful note to eliminate the source of this additional vibration and maintain the same sensor position throughout a whole set of experimental data.

Thirdly, there also exists an hysteresis effect in the journal bearing, as illustrated in Figure 3-21. Here, setting the same high rotational speed, we started with an initial condition (dP = 5.13psig), then increased it (to 5.44psig) and finally dropped it to below the initial value (at 4.74psig). We detect that the natural frequency does not drop back to the initial value, though the direction of change is consistent. This suggests a possible hysteresis effect, on the order of 10%, on the stiffness of the journal bearing. This brings out caution to the experimentalist who may be operating between two previously defined stable points.

In the latest MicroBearing builds, examination of the frequency spectra at low rotational

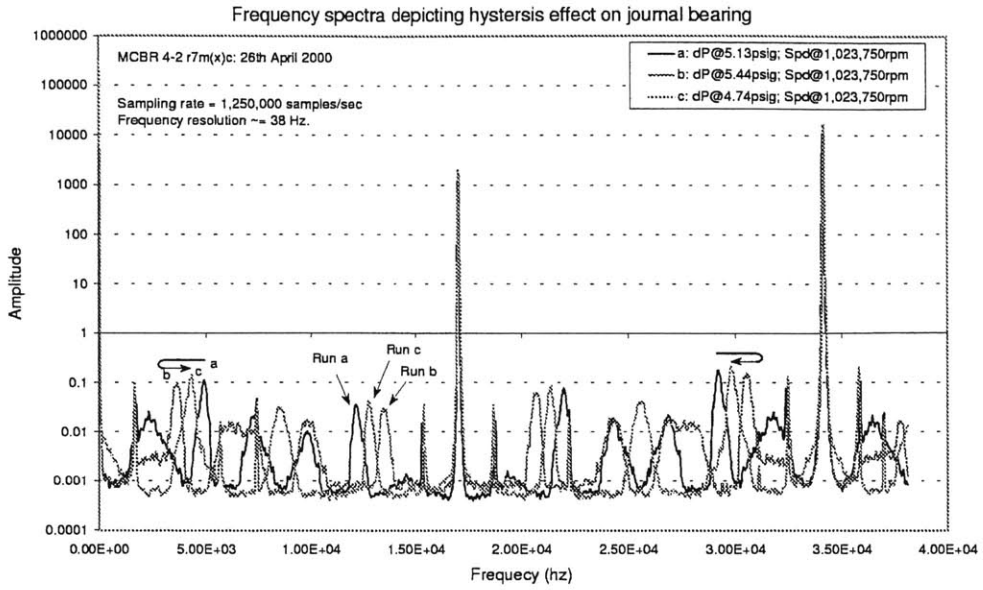

Figure 3-21: Hystersis effects of journal bearing.

speeds do *not* show the natural frequency until operation at high speeds. This is especially so for the dies at the center of the wafer, where we have less etch non-uniformity. This could be because of a smaller amplitude of whirl motion (that is undetected until higher rotational motion) due to a smaller imbalance. In order to confine ourselves to a stable operating regime, we use the operating line from previous builds to operate our device, while constantly watching out for subharmonic excitations.

Effects on crossing the natural frequencies Crossing integer multiples (termed also as cartiers) of the natural frequency at *early* stages of the spin-up operation is potentially hazardous. This is because we are often at a whirl ratio of 2 and above at low speeds, where it is suggested by Larson and Richardson to be an unstable region [38]. Equation 2.5 cites the whirl ratio boundary for stability—where the authors report a maximum whirl ratio of up to 6. At low speeds in our operating line, we are often at this order of magnitude; at high speeds, we managed a whirl ratio of between 1 and 2 as will be presented in Figure 3-24.

In addition, we note that, during high speed operation, we managed to cross the fundamental natural frequency in several of the dies while not detecting the subharmonic responses.

A sample of this characteristic is illustrated in Appendix C-6[30]. However, in the operation of this device, we continued to increase the axial differential pressure even when already at subcritical operation. This placed us at below the first natural frequency and we observed a consistent half-speed whirl frequency and a significant increase in load. These two effects are discussed in Section 3.4.3 and Section 3.5.

3.4.3 A waterfall chart

Combining the Fourier spectra at various rotational speeds produces a "waterfall plot" of the operation. Figure 3-22 portrays the spectrum from our device MCBR 4-9 up to 1.22 million rpm. A simpler illustration is listed in Appendix C-3. Here we see the synchronous speed (and its integer multiples) shifting to the right as expected. More interestingly, we observe the excitation of a "half-speed whirl" appearing very strongly before the final crash. In fact, subsequent changes in axial differential pressure seems to result in no changes to this peak of 10071 Hz[31].

Several authors (Atkin and Perez, Muszynska, and Childs) relate the appearance of this "half-speed whirl" as indicative of rotordynamic instability [11, 49, 1]. Childs clearly illustrates the "half-speed whirl" exceeding the synchronous component in leading up to instability [11, pg24.]. For a Jeffcott rotor, Muszynska further shows the transition of a "half-speed whirl" into a "whip" [32] where this large amplitude subsynchronous peak drops away from 50% of rotational speed and results in rotordynamic instability. This result is also analytically shown by Crandall in 1990 [16]. Interestingly, this "half-speed whirl" instability is also seen in a discussion by Orr on the macro Bearing rig experiments, where he terms this as the "sub-synchronous" at the "onset of hydrodynamic whirl stability" [54].

The appearance of the "half-speed whirl" in our device is therefore suggestive of the

[30]The device eventually reached a final speed of 1.3 million rpm.

[31]The additional spectrum of 2% change in axial differential pressure is not shown in Figure 3-22 since it falls right together with the original.

[32]This "whip" term by Muszynska is quite different from dry-friction whipping in rotating machinery, but rather is the natural frequency, W_n, discussed in this work.

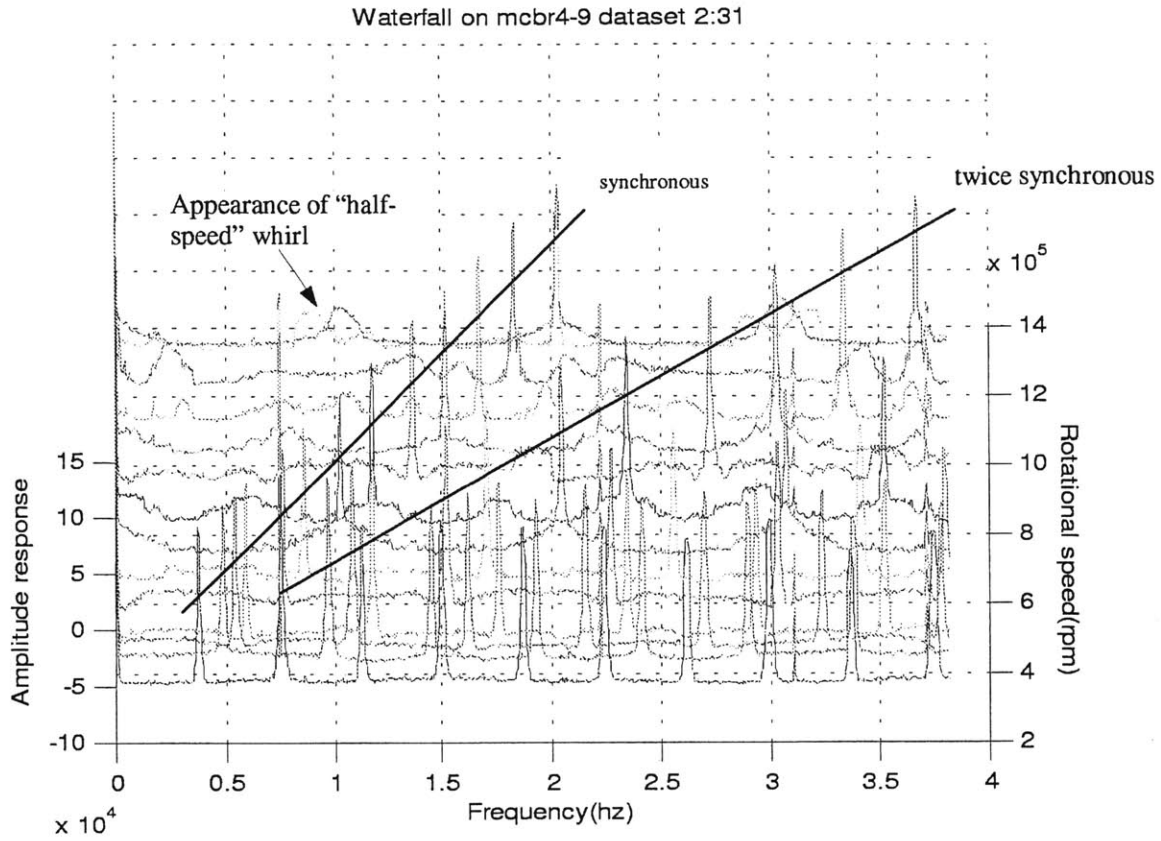

Figure 3-22: A waterfall chart of the Fourier spectra of device MCBR 4-9. The sharp peaks increasing in frequency are the synchronous speeds.

onset of instability. In operation of the MicroBearing rig, appearance of subharmonics at near 50% of the rotational speed is ultimately hazardous. A large change in axial differential pressure or load might possibly eliminate this "half-speed whirl" due to changes in bearing reaction forces, though the result is unclear. An example would be to increase the axial differential pressure significantly in an attempt to increase the hydrostatic stiffness greatly over the hydrodynamic stiffness; however, our previous attempt to do so brought the rotor to subcritical operation and a subsequent crash, when crossing the critical again. Childs suggests replacement of the plain journal bearing (wherein this effect is most pronounced) with other bearing modes as the most direct approach, though significant redesign would be needed. Some possible configurations include:

- Multilobe Bearing
- Axial-Groove Bearing
- Step Bearing
- Tilting-Pad Bearing[33],

of which the multilobe bearing has been investigated by Piekos [57].

3.4.4 Further remarks on W_n

Windowing In the power spectrum estimation for the detected signal, there are several methods to perform the windowing to reduce the noise. These consist of a Bartlett window, a Square window, generalized cosine windows (Hamming, Blackman, Hanning, *et al.*) and a Kaiser window. The results from a code compiled by Jacobson [35] is illustrated below for the Square, Hanning and Hamming windowing procedures. Upon comparison, we note that the Hanning window gives the least noise width around the synchronous frequency. Comparisons against other methods are listed in Appendix C.3.

3.5 Analysis of Results and Further developments

Summary of operating results Figure 3-24 here summarizes all the high-speed MicroBearing runs and the associated natural frequency obtained using the procedure described in Section 3.4.2. Here we observe we have operated our high-speed device between the first and second fundamental natural frequencies by maintaining our nondimensional parameter $\frac{Rotational\ Speed}{(Axial\ differential\ pressure)^2}$ at approximately 4.5.

In the final crashes of device MCBR 2-5 and MCBR 4-9, we observe a very significant increase in the load as will be discussed later. In addition, just prior to crashing of device

[33]A tilting-pad bearing is projected to eliminate stiffness cross-coupling terms and hence the source of bearing instability.

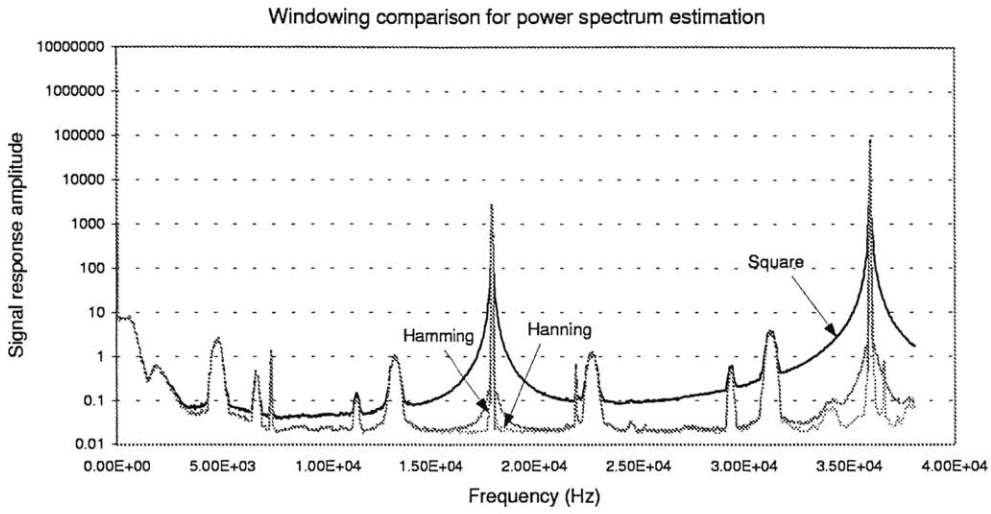

Figure 3-23: Comparison of Square, Hamming and Hanning windowing procedure on the power spectrum estimation of the MicroBearing natural frequency.

MCBR 4-9, we observe the appearance of a "half-speed" whirl phenomenon. Device MCBR 3-10 failed because of the thrust bearings. The cause of device MCBR 4-2 crash remains unclear, though it is strongly suspected, in this instance, to be due to the inaccurate control of the journal bearing needle valves at high pressures.

Side-loading and Hydrodynamic effects Figure 3-25 summarizes the differences in the journal bearings pressurizations (Low and High plenums) in the high-speed rotating dies. While we have attempted to zero out this undesirable side-loading during hydrostatic operation, the sharp increases in the sideload is often coupled with an "inverse" flowrate. That is, at very high speeds, we would notice the pressure in one of the journal bearing plenums (say the High) has a larger increase than the other, while the flowrate in that higher pressurized side being smaller. We have shown in Chapter 3.2.1 that the packaging and the in-device flow channels are acceptably similar (in terms of flowrates) for even up to 10.0 psig. Moreover, in device MCBR 4-9, this side-loading only increased when we were

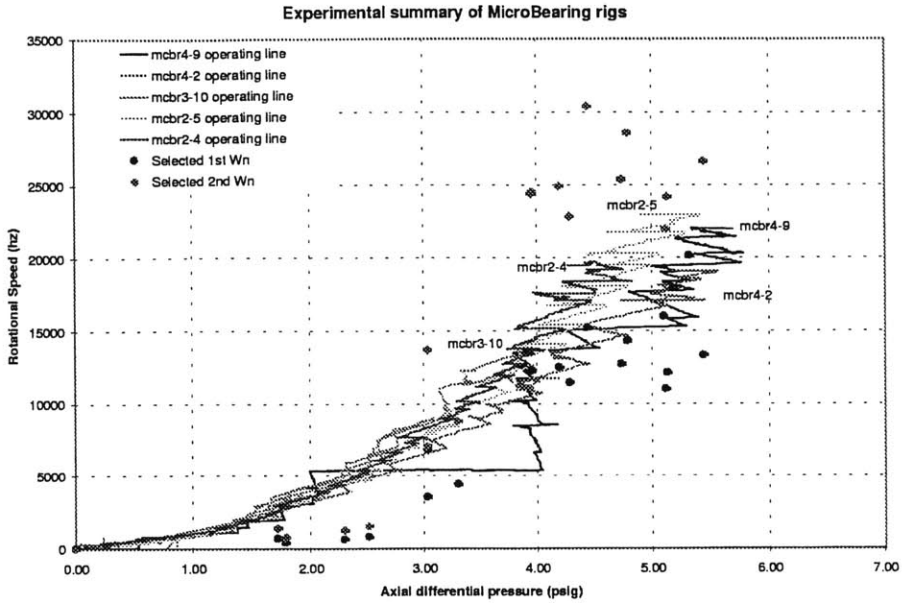

Figure 3-24: Summary of our device operating line with the experimentally determined natural frequency.

increasing the main turbine pressure[34]. Large loads were observed in several runs prior to crashing[35]. This suggests a possible cause of failure as the rotor spinning at an off-center position, not due to the journal bearing pressurizations.

Onset of hydrodynamic operation It is possible that the side-loading causes hydrodynamic operation, which leads to the rotor crashing. Piekos provides sample stable orbits at a center-offset fixed point operation in hydrodynamic mode and unstable orbits when the applied load is above or below the desired value [57]. This is the only logical conclusion given that the rotor crashes only with increases in the main turbine flow, and not when varying other flowrates.

While it is unclear when this transition occurs, the development of an eccentricity sensor will allow us to understand the hydrodynamic operation. In fact, without a measure of the

[34]Previous devices, including device MCBR 2-5, had both the main turbine and journal bearing pressure coupled together and thus indistinguishable as to the cause of crash.

[35]In addition, we did not observe a consistent trend of one journal bearing plenum being at a higher pressure than the other.

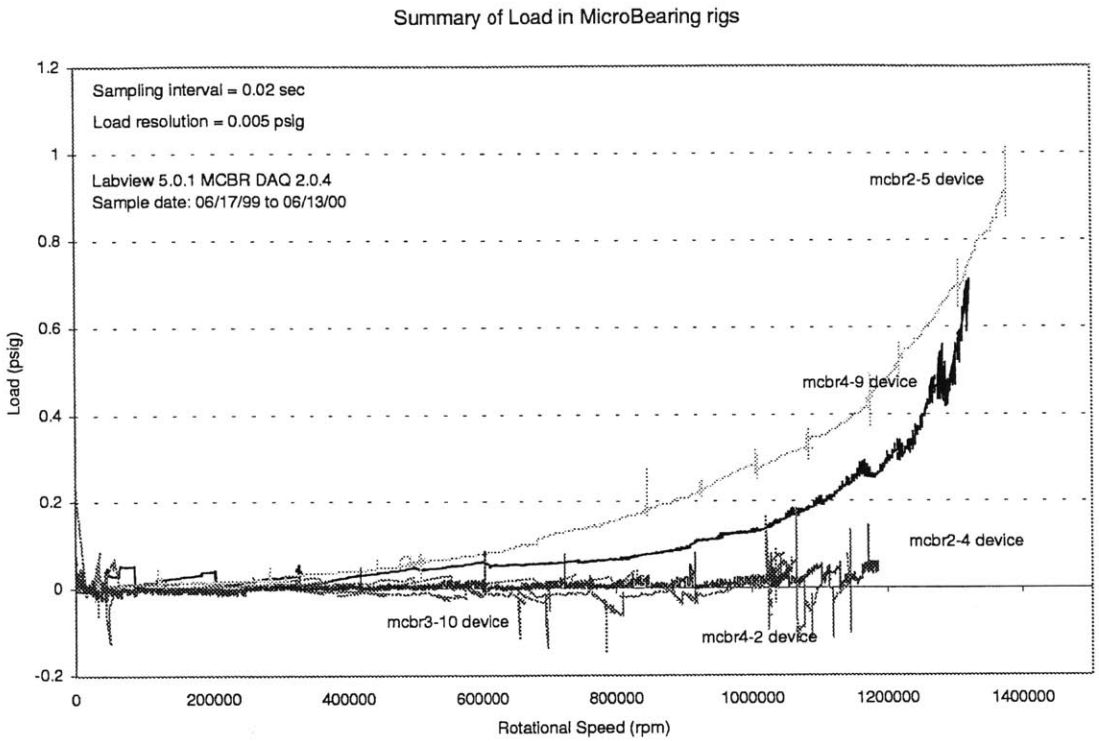

Figure 3-25: Summary of load in high-speed rotating dies, depicting sharp increases in load just before catastrophic crashes. This load is the difference in journal bearing pressures between the Low and the High plenums, leading to a sideload on the rotor.

in-built imbalance, it is even more difficult to estimate a desired applied external load for a required eccentricity. Using a hydrostatic journal bearing theoretical stiffness to predict an estimated load for a given eccentricity would not prove useful in this aspect since an accurate load parameter is neccessary for the experimentalist. We could conceivably also employ a computation of an expected flowrate for a given eccentricity and geometry for a more precise eccentricity, though it would be difficult to tell the eccentricity, for a rotating body, from a static plenum flowrate. Indeed, we do require accurate positioning of the eccentricity for hydrodynamic operation.

Half-speed whirl In the operation of device MCBR 4-9, we also observe the appearance of a "half-speed whirl" just before the onset of instability (Figure 3-22). This "half-speed whirl"

is presented in literature as detrimental to stability of rotordynamics. This appearance of the "half-speed whirl" was after we operated below the fundamental natural frequency in a subcritical operation. As mentioned earlier, experiments on the macro Bearing rig also noted this same "half-speed whirl" before hydrodynamic instability [54]. We would, nonetheless, certainly express caution to the experimentalist when detecting this "half-speed whirl" appearance in our gas-lubricated journal bearing design. As an interest from literature, suggestions to overcome this "half-speed whirl" stems into investigations of a multilobe or tilting-pad journal bearing design.

Larson and Richardson Instability In Richardson and Larson's paper [38], rotordynamic instability, in addition to half-speed whirl, is cited as occuring at greater than twice the fundamental natural frequency for hydrostatic operation. (There are, however, cases of operation to even six times this natural frequency presented [23, 38].) Having selected the MicroBearing natural frequency as seen in Section 3.4, it is hence prudent to operate at below twice this fundamental frequency when given the opportunity. Figure 3-24 shows our operation line, which we have miraculous kept by maintaining our nondimensional $\frac{Rotational\ Speed}{(Axial\ differential\ pressure)^2}$ parameter at approximately 4.5 at high rotational speeds.

Thrust Bearings Device MCBR 3-10 from Microbearing build 3 spun up well in terms of journal bearing operation. The first test on this batch of dies had an edge die that reached an ultimate rotational speed of 870,000 rpm, as represented in Figure 3-12. However, a post-analysis on its operation brought to light the failure of the thrust bearings just before its final crash. This is portrayed in Figure 3-26.

In Figure 3-26 we observe sharp jumps of the forward thrust bearing flowrate and a complementary drop in the aft thrust bearing flowrates. These spikes are suggestive of transient flowrates in the thrust bearings[36]. In fact, for this particular device, we recorded, earlier on, a rapid deceleration to zero rotational speed when a similar jump in thrust bearing

[36]The very large flowrate measurements are probably not accurate [35].

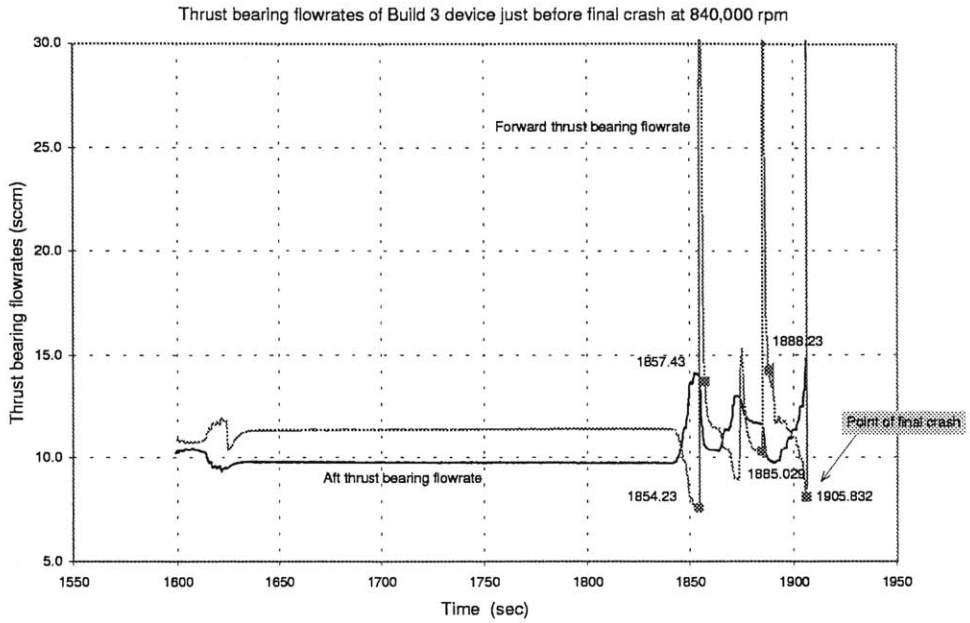

Figure 3-26: Failure of the thrust bearings in build 3 device seconds prior to ultimate crash and right at the point of crash.

flowrates occurred. Hence the multiple occurences of these sudden variations in thrust bearing flowrates, each spanning approximately 3 sec spikes across a time period of 50 sec, are indicative of the cause of the final failure. It is thus suggested that the thrust bearing nozzles be fabricated to as close to the design value of $10.0\mu m$ as possible[37].

Imbalance with MicroBearing performance The fabrication efforts to reduce the imbalance—through etch non-uniformity reduction and minimizing the misalignment on the rotor plate—has brought about large improvements in MicroBearing operation. We note here the "easy" spin-up of the devices and the high performance achievements of edge dies, which would not be possible with the previously suspected imbalance level.

[37]We note here that 12.8um nozzles (in MCBR Build 3) failed at high speeds, while 9.3um nozzles (in MCBR Build 4) function well at the maximum rotational speed we obtained.

Suggestions for further development With the transition into a hydrodynamic mode of operation and with hydrodynamic stiffness expected to be larger than its hydrostatic counterpart, the key to operation in the hydrodynamic mode would be the development of an eccentricity measurement scheme. This could possibly be in the form of a displacement sensor, or a highly calibrated flowrate model for a given eccentricity. Development of the sensor might be more favorable since it:

1. Enables hydrodynamic operation:
   - Hydrodynamic orbits may not be at a fixed point operation, and hence a flowrate from a static plenum might not be useful.
   - Deep etching of journal might cause slight variation in journal clearances across wafers and dies, leading to necessary intensive measurements of the actual clearance in order to use a highly calibrated flowrate-eccentricity model,
   - Recording of the orbits would be especially interesting and helpful in constructing of a hydrodynamic operating line.
2. Counterchecks the hydrostatic whirl frequency: With positional data, the velocity result can be obtained as a countercheck on our measurements. The specific hydrostatic whirl orbit could also be determined.

Constructing a reliable eccentricity sensor is not an easy task in microdevices as noted by Chen [10], and obtaining a commercial measurement system might be a useful path in parallel.

Moreover, instead of enabling a hydrodynamic mode of operation, we could perhaps delay the transition from a hydrostatic to a hydrodynamic mode. Other journal bearing geometries, such as the multilobe or step bearings, should be investigated. These bearing geometries, when designed appropriately, may lead to bearings with a larger hydrostatic to hydrodynamic stiffness ratio, allowing the benefits of hydrostatic bearings at higher speeds. These experiments into a variant journal bearing design, instead of a plain, cylindrical journal

bearing, would certainly be interesting and helpful in extending the current operating range of the MicroBearing device.

In terms of experimenting with the hydrostatic journal bearing operation, we can also consider coupling both Low and High journal bearing plenums together. This could be either supplying both plenums with a single flow source, or fabricating a single plenum for the journal bearing. While this will not allow side-loading, it will nonetheless ensure equal pressures on both sides of the journal bearing. Finally, reducing the imbalance—either through fabrication improvements or static balancing—could perceivably extend the range of hydrostatic journal bearing operation.

Chapter 4

Hydrodynamic Thrust Bearing: Theory

You might discover after a bit, for example,
that when there's only one bishop around on the board
that the bishop maintains its color. Later on you might
discover the law for the bishop as it moves on the diagonal
which would explain the law you understood before...
Then things can happen, everything's going good,
you've got all the laws, it looks very good,
and then all of a sudden some strange phenomenon occurs in some corner.
–R. Feynman, The Rules of The Game (1981)

This chapter covers the design of a hydrodynamic spiral groove thrust bearing. We begin with the basis for selection of this type of thrust bearings and present previous insights from literature. The developed theoretical model, formulated mainly from Muijderman [47], is used to optimized the design for the thrust bearing load capacity. Analysis indicates the need for a hybrid hydrostatic-hydrodynamic mode for low speed operation. The design of this hybrid bearing is also discussed. This chapter concludes with a discussion of stability considerations, rarefaction effects and other selected challenges.

4.1 Conceptual Development of Spiral Groove Bearing

4.1.1 Why a spiral groove bearing

The current hydrostatic inherent-restrictor thrust bearing requires large external pressurizations for the microturbine to be operational. Typical pressures for the hydrostatic thrust bearings range between 40 to 70psig depending on the desired stiffness and load. For the actual MicroEngine to achieve self-sustained operation (such that necessary bearing pressures could be tapped from the compressor exhaust pressure[1]), new thrust bearing designs needs to be explored.

As a historical note, hydrostatic thrust bearings were chosen initially for the MicroEngine because they provide high stiffness and high load capacity independent of rotational speed. In addition, a hydrostatic mode allows the axial position of the rotor to be controlled relatively easily, an important feature when the turbine and journal bearing operations are of initial concern.

The consequence of employing hydrostatic thrust bearings is the need for relatively high pressures. This is because the stiffness and load capacity is derived, with external pressurization, from two restrictors in series—an "orifice compensation" and a "film" restrictor[2]. This is depicted in Figure 4-1. With an increase in load on the thrust bearing, the bearing gap will decrease. This increases the net flow resistance and decreases the mass flowrate, resulting in a lower pressure drop across the "orifice compensation" restrictor. This leads to a larger pressure drop at the "film" restrictor and thus produces the restoring force. Hydrostatic thrust bearing are well-documented in literature by Vohr [69], Optiz [53], Hamrock [34] and many other authors. Specifically, our hydrostatic thrust bearing designs were simulated, designed and tested by Jacobson [35], Orr [54] and Lin [40].

[1]The combustor inlet pressure is the maximum available static pressure for the bearings.
[2]In an electrical analogy, the two restrictors could be treated as a simple voltage divider.

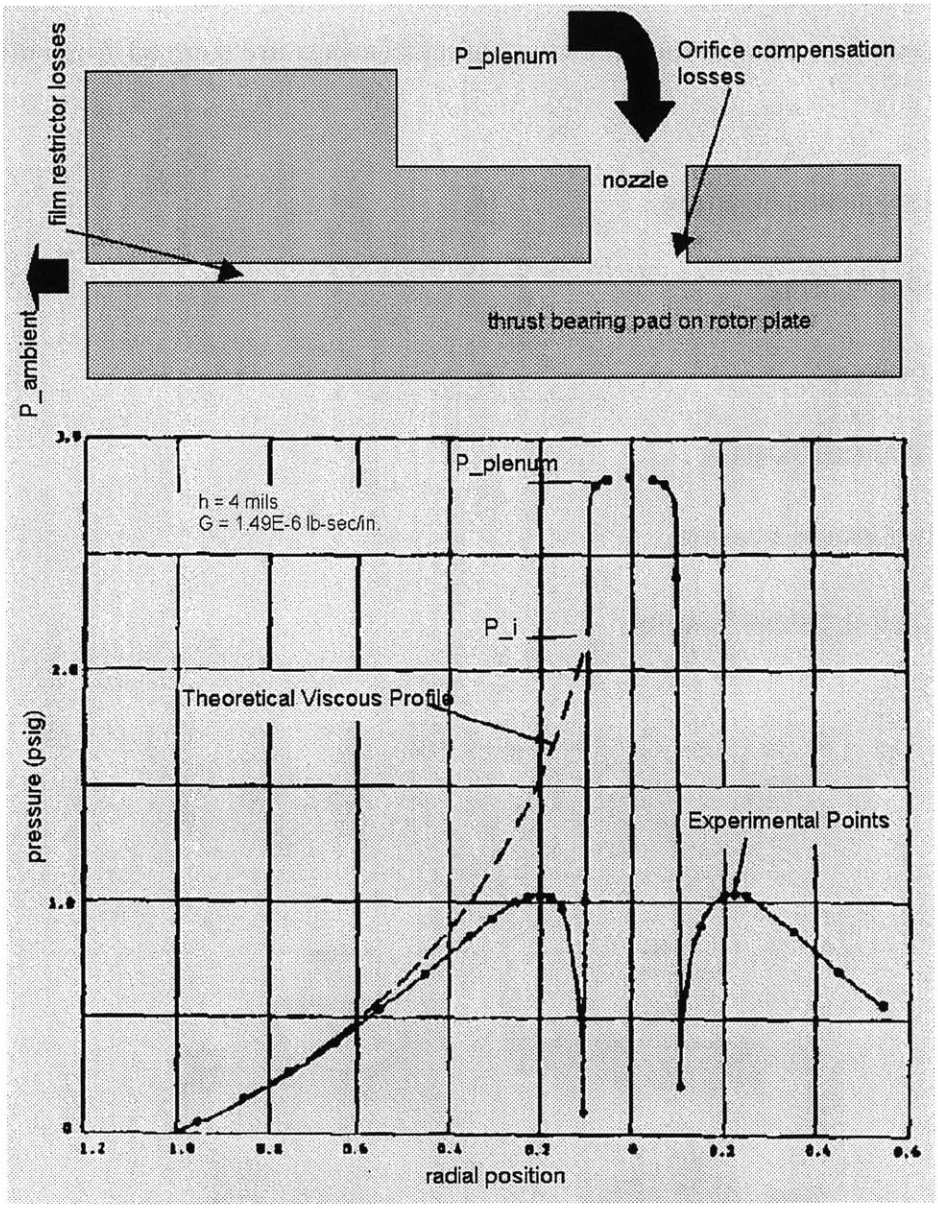

Figure 4-1: Concept of the hydrostatic thrust bearing (adapted from Vohr [69, 54])

To achieve a much lower pressurization of the thrust bearing, however, several choices of gas-lubricated self-acting thrust bearings are possible. Using primarily the concept of hydrodynamic squeeze film effects, the following thrust bearings are sourced from literature [34, 47, 62, 42]:

- Parallel-step slider bearing
- Taper-land bearing
- Pocket bearing
- Spherical thrust bearing
- Flat spiral groove bearing
- Conical spiral groove bearing.

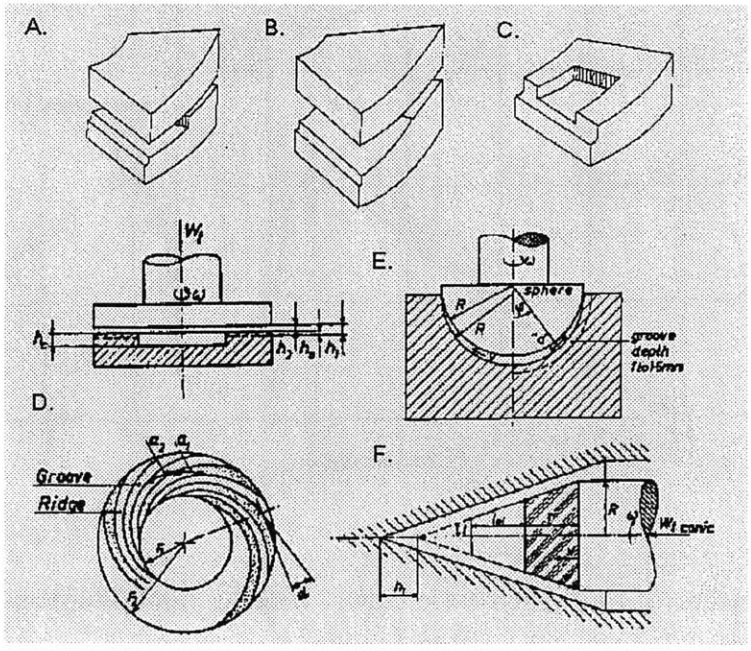

Figure 4-2: Other kinds of self-acting thrust bearings (adapted from [42, 55]): A. Taper-land, B. Step, C. Pocket, D. Spiral Groove, E. Spherical, F. Conical spiral groove.

These thrust bearings, many simply named after their geometry, are shown here in Figure 4-2. Numerical solutions for these bearings under gas-lubrication are summarized by Hamrock [34]. Of these bearings, the spiral groove bearings and the parallel-step slider bearing have extensive design and experimental data in literature. Parallel-step slider bearings, however, require a "feed groove" that is a few orders of magnitude larger than the bearing gap [34], leading to possible anisotropic deep-etch fabrication difficulties. Conical spiral groove bearing designs are also rejected because of the difficulty of achieving three-dimensional features in the planar semiconductor microfabrication environment. Given the availability of experimental data and fabrication constraints, we therefore focused our design to the family of spiral groove bearings.

Though spiral groove bearings essentially requires no additional external pressurization, it adds drag to the turbine and there might be issues with stability. These issues of drag and stability are to be considered when selecting a final configuration from the family of flat (planar) spiral groove bearings as listed here:

1. Full flat spiral groove bearing without transverse flow
2. Herringbone flat bearing
3. Partially grooved flat spiral groove bearing.

They are depicted in Figure 4-3 for reference. Of these three possible designs, a full flat spiral groove bearing without transverse flow provides the largest load capacity compared to the other two.

Herringbone flat bearings and partially grooved flat spiral groove bearings are especially suitable if the inner chamber inside radius r_1 is not closed. The opening of the inner chamber will result in a transverse flow, creating a pressure drop at the inner chamber and hence a lower load-carrying capacity. This is the reason why Herringbone flat bearings and partially grooved flat spiral groove bearings (even when optimized) are unable to compete with full flat spiral groove bearings without transverse flow.

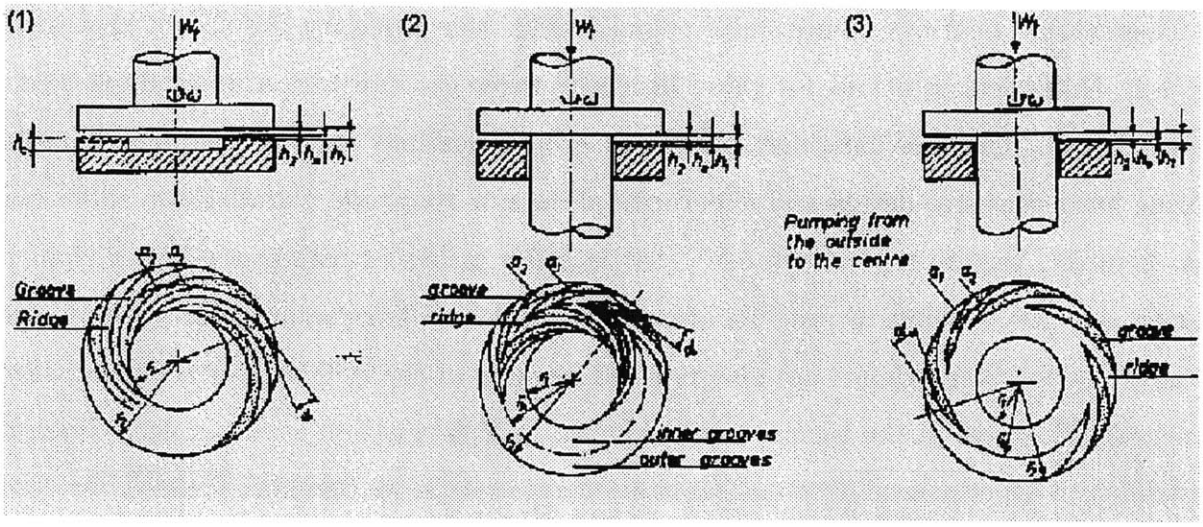

Figure 4-3: Other spiral groove bearings configurations (adapted from[47]): (1)Full flat spiral groove bearing without transverse flow, (2)Herringbone flat bearing, (3)Partially grooved flat spiral groove bearing.

A Herringbone flat bearing reduces the transverse flow with its geometric design by placing the highest pressure at the center of the spiral groove length. A partially grooved flat spiral groove bearing increases its load capacity by virtue of the inner ungrooved raised height which prevents the pressure from falling off to zero at the ends of the spiral grooves. They are particularly useful if there is transverse flow in the thrust bearing.

Without transverse flow, therefore, a full flat spiral groove bearing surfaces as the best choice since the inner chamber for the MicroEngine can afford to be closed. This is because the journal bearing is designed to be radially outside the thrust bearing, leading to the absence of the inner chamber shaft as seen in Figure 4-3. A spiral groove bearing in this work from hence will thus refer to a full flat spiral groove bearing.

4.1.2 Historical layout

Spiral groove bearings were first readily accounted theoretically by Whipple [71] in 1949 (the report remained classified until 1957). It was also in 1957 when a paper by Ford, Harris

and Pantall [30] was published on a flat axial gas-lubricated spiral groove thrust bearings. Independently, Boon and Tal [8], in 1959, reported on viscoseals which were modeled similarly with a parallel groove pattern. In 1956, Woodsworth [75] also published his 1952 theoretical work on spiral groove thrust bearings.

However, both the Whipple and Woodsworth models had the common assumptions that *(1)* the grooves are considered narrow enough such that the end effects can be neglected, and *(2)* the pressure distribution across the grooves can be regarded as linear. These assumptions turned out to be questionable when experimental work by Whitley and Williams [73] depicted serious differences between the theoretical predictions and experimental values.

E.A. Muijderman[47], in 1966, performed a more comprehensive modeling and predicted results that coincided well with the experimental data. Muijderman formulated his model by solving the simplified Reynolds equation, the energy equation for Newtonian fluid and the continuity equation analytically. He found that the assumption of linear pressure distribution across the grooves is valid, except at the groove ends. Muijderman then included an empirical correction for the end effects of spiral groove bearings since the analytical solution of the groove ends were difficult to obtain[3]. Besides the analytical solution, he was also able to arrive at approximate solutions to capture the pressure distribution and the frictional forces. The approximate solutions were based on a linear pressure distribution in an incompressible fluid across the grooves, and predicted the experimental results adequately.

4.1.3 Physical concept of the spiral groove bearing

The physics of the spiral groove bearing can be explained by simply considering the respective flow resistances. Since the flow resistance along the grooves is smaller than the resistance across the groove, an adjacent plate (to the spiral grooves) in motion will induce a flow along the grooves. The induced flow, if the adjacent plate moves in the direction of the incline of the spirals, will be inwards. This inward-induced flow will then cause a pressure

[3]Employing these empirical corrections for our modelling would thus require a validation of the scaling effects in the microscale.

rise (above ambient) as we transverse toward the center of the bearing. This basic concept is now explained in more detail.

Consider the fluidic element shown in the Figure 4-4, with the top member moving the positive x-direction (Figure 4-5) [47]. From the generalized Reynolds equation[18] and imposing the following assumptions:

- time-invariant incompressible fluid
- all other velocity components, except in the x-direction, are zero (see Figure 4-5)
- a planar surface of the spiral grooves

we simplify the expression of the pressures in the spiral groove bearing into the following partial differential equation

$$\frac{\partial}{\partial x}(\rho\frac{\partial p_i}{\partial x_i}) + \frac{\partial}{\partial z}(\rho\frac{\partial p_i}{\partial z_i}) = 0, \tag{4.1}$$

where the subscript i represents distribution in the groove or above the ridges, ρ the density, and p the pressure.

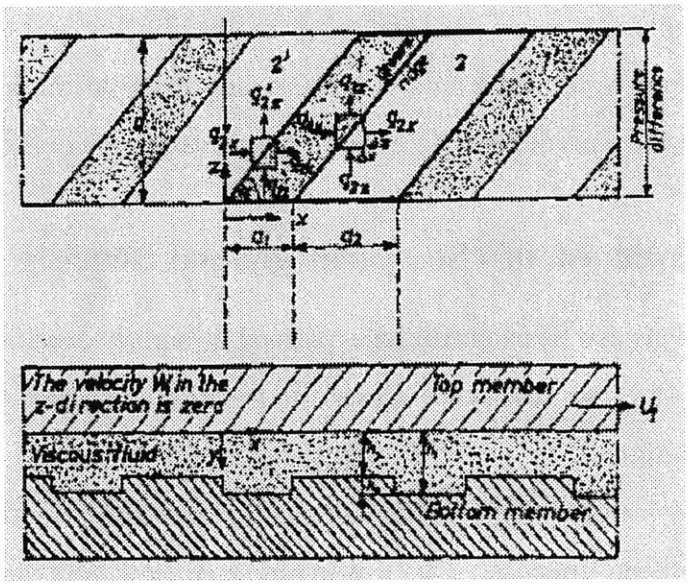

Figure 4-4: Fluidic Element, showing nomenclature for derived expressions.

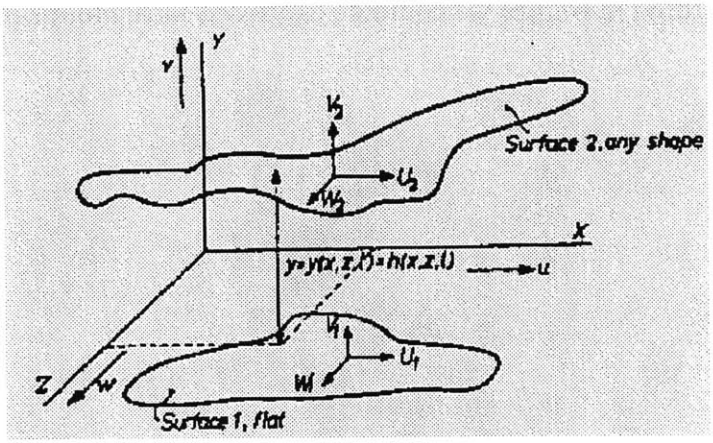

Figure 4-5: Coordinate system in Muijderman[47], showing nomenclature for derived expressions.

With an approximated linear pressure distribution, Muijderman derived the solution of Equation 4.1, leading to the pressure build-up as illustrated in Figure 4-6. The top member moves in the positive x-direction to generate the shown pressure distribution. We note that this approximate pressure build-up does not yet include the end effect of the grooves.

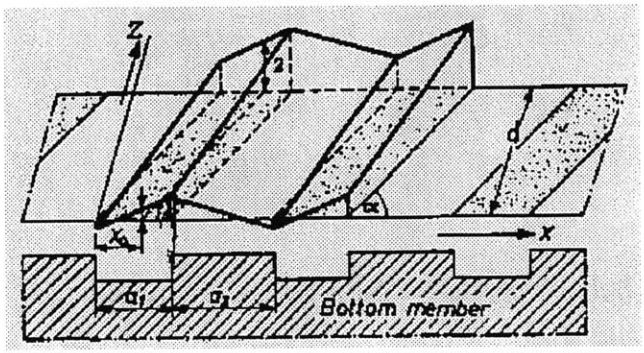

Figure 4-6: Approximate Pressure Build-up in grooves and ridges.

The pressure "waves" at the interface of the groove and the ridge increase toward the thrust bearing center and provide the load capacity of interest. Section 4.2 investigates the pertinent characteristics of the spiral groove bearing within our design space.

Also of concern are the resultant mass flow rates in the spiral grooves. The mass flows of

each element (as illustrated in Figure 4-4 could be expressed in the following non-dimensional forms [47]:

$$\bar{q}_{1x} = \bar{\rho}\left(K\frac{\partial \bar{p}_1}{\partial \bar{x}} + 1\right) \tag{4.2}$$

$$\bar{q}_{2x} = \bar{\rho}\left(H^3 K\frac{\partial \bar{p}_2}{\partial \bar{x}} + H\right) \tag{4.3}$$

$$\bar{q}_{1z} = \bar{\rho}K\frac{\partial \bar{p}_1}{\partial \bar{z}} \tag{4.4}$$

$$\bar{q}_{2z} = \bar{\rho}H^3 K\frac{\partial \bar{p}_2}{\partial \bar{z}} \tag{4.5}$$

where the subscript *1* depicts position in the grooves and subscript *2* depicts position above the ridges. The nondimensionless terms in the above Equations (4.2)-(4.5) are defined as the following:

$$\bar{x} = \frac{x}{d},\ \bar{z} = \frac{z}{d},\ \bar{\rho} = \frac{\rho}{\rho_0},$$

$$\bar{p_{1,2}} = \frac{p_{1,2}}{p_0} \quad , \quad H = \frac{h_2}{h_1},$$

$$\bar{q}_{1x} = \frac{2q_{1x}}{U_1 h_1 \rho_0} \quad , \quad \bar{q}_{1z} = \frac{2q_{1z}}{U_1 h_1 \rho_0},$$

$$\bar{q}_{2x} = \frac{2q_{2x}}{U_1 h_1 \rho_0} \quad , \quad \bar{q}_{2z} = \frac{2q_{2z}}{U_1 h_1 \rho_0},$$

$$K = -\frac{h_1^2 p_0}{6\eta U_1 d}.$$

These massflow rates are only of theoretical interest since experimental values for comparison would be difficult to obtain.

4.2 Models: Muijderman, Pan and Malanoski

Muijderman[47] derived the exact solution to Equation 4.1 analytically. This was for a model that did not include the end effects of the spiral grooves. The solution for the pressure

difference is:

$$p_{exact} = \frac{12\eta\omega r_2^2}{h_0^2}\lambda^2(\cot\alpha)\{1-\exp^{(2\pi\sin 2\alpha)/m}\}\frac{\{(2\pi\sin\alpha\cos\alpha)/m+\ln\lambda\}^2}{\sin\alpha} \times \frac{m}{\pi\sin\ 2\alpha}\{\sum_{n=1}^{\infty}\frac{1-(-1)^n e^{(2b\sin\alpha)/c}}{4(b/c)^2(\sin^2+n^2\pi^2}(\sin\alpha)+\frac{c}{4b}\}, \tag{4.6}$$

where

$$b/c = -\frac{2\pi}{m}\frac{(\sin\alpha\cos\alpha)+(m\ln\lambda)/2\pi}{\sin\alpha}, \tag{4.7}$$

p_{exact} as the pressure difference between the inner radius and outer radius of a spiral groove, and the other terms described in the nomenclature section (page 17) and shown in Figure 4-7.

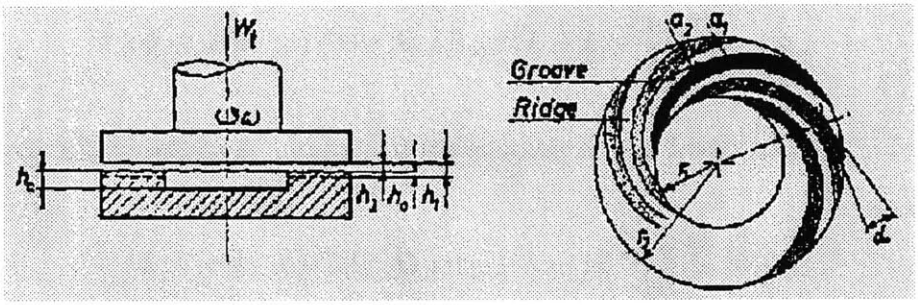

Figure 4-7: Nomenclature of terms in the sprial groove bearings.

In order to include the end effects[4], Muijderman took an alternative approach[5] to solving Equation(4.1). He imposed a linear pressure approximation profile and, using an electrical analogy (instead of analytically), obtained the "effective" spiral groove end radii r_{1eff}, r_{2eff} experimentally. They are expressed as

$$r_{1eff} = r_1\, e^{\frac{\pi}{m}(1-\frac{\alpha}{90})(\tan\alpha)}\frac{2}{1+\gamma}\frac{1-H^3}{1+H^3}\frac{A_1\prime\cot\alpha}{A_1\prime\cot\alpha+C_1\prime} \tag{4.8}$$

$$r_{2eff} = r_2\, e^{-\frac{\pi}{m}(1-\frac{\alpha}{90})(\tan\alpha)}\frac{2}{1+\gamma}\frac{1-H^3}{1+H^3}\frac{A_2\prime\cot\alpha}{A_2\prime\cot\alpha+C_2\prime} \tag{4.9}$$

where α is expressed in degrees and the coefficients $A_{1,2}\prime, C_{1,2}\prime$ are also listed in the nomen-

[4]The end effect is a drop in pressure at the edges of the spiral grooves.

[5]The analytic form was difficult to evaluate and might not lead to a closed-form solution

clature section. And, to use these experimentally-derived coefficients, this equality must be satisfied to match Muijderman's experimental condition:

$$k > (2.5(\sin^2\alpha)\,\frac{2}{1+\gamma} + \frac{1}{2}\sin 2\alpha)\,\frac{\pi}{-\ln\lambda}, \tag{4.10}$$

where k is the number of grooves in the spiral groove bearing. This ensures that the length of the groove is at least 2.5 times the groove width.

Thus, adding in these experimentally obtained end effect corrections, Muijderman arrived at a more-detailed set of expressions for the pressure build-up, load-carrying capacity, and frictional torque. The pressure build-up p_{r1}(above ambient pressure) is represented in

$$p_{r1} = \frac{3\eta\omega r_{r2}^2}{h_2^2}\,(1-\lambda^2)\,g_1(\alpha, H, \gamma)\,C_1(\alpha, H, \gamma, \lambda, k), \tag{4.11}$$

where g_1 and C_1 are expressed in the nomenclature section. And the load-carrying capacity W_t computes as

$$W_t = \frac{3\pi\eta\omega r_2^4}{2h_2^2}\,(1-\lambda^4)\,g_1(\alpha, H, \gamma)\,C_2(\alpha, H, \gamma, \lambda, k), \tag{4.12}$$

where C_2 is also described in the nomenclature section.

The factor g_1 accounts for the optimal geometric design, depending on the spiral groove angle, the film height above the ridges and the groove depth. Typical g_1 values range from 0.01 to 0.09. In addition, the factors C_1 and C_2 account for the end effect pressure losses and are thus called "end effect correction factors". The end effect correction factors not only depend on the spiral groove angle, the film height above the ridges and the groove depth, but also on the number of grooves, the inner and outer spiral groove radii, and the widths of the groove and ridges. The computation of these factors in our model is listed in Appendix D.2 and counter-checked against Muijderman[47].

Finally, the frictional torque, which was used to compute the drag, is found from

$$M_t = \frac{\pi\eta\omega r_2^4}{2h_2}\,(1-\lambda^4)\,g_2(\alpha, H, \gamma), \tag{4.13}$$

where M_t is the frictional torque due to the spiral groove bearing[6] and g_2 as listed in the nomenclature reference (Section , page 17).

Pan and Malanoski [41](Mechanical Technology Incorporated) in 1965 also published their results independently from Muijderman. The results between Pan and Malanoski and Muijderman were similar—Muijderman gave more details on the derivation of his model and included the end-effects; Pan and Malanoski included a discussion of the static and dynamic stability of the hydrodynamic thrust bearings.

4.3 Axial Thrust Balances

To predict the required design load capacity of the spiral groove bearings, the axial forces on the rotor due to the air pressures (except the thrust bearings) must be computed. The downward forces on the rotor are due to: *(A)* pressure drop across the turbine, *(B)* momentum change of these main air out of the exhaust. In addition, the upward forces on the rotor are: *(C)* pressurization of the journal bearings, *(D)* shear flow of the bearing air, *(E)* pressurization across the seal of the journal bearing, *(F)* momentum change of the Motor Outer Plenum air as it enters the aft side of the rotor, *(G)* pressurization of the Motor Outer Plenum across the generator gap, *(H)* momentum change of the Motor Outer Plenum into the exhaust. This is illustrated below in Figure 4-8.

A simple computation shows the order of magnitude from momentum change and shear flow as relatively small compared to pressurization forces, and thus can be neglected from axial load computations.

Without the thrust bearings, typical operation[7] of the Microbearing rig results in a net axial force downwards at lower rotational speeds, and upwards at higher rotational speeds. This is shown in Figure 4-9. We note, of course, that if the operating conditions of the

[6]Frictional torque due to the inner chamber is negligible since the inner chamber is recessed into a deeper depth.

[7]The schedule followed in a 'typical' operation of the Microbearing rig allows for stability of the hydrostatic journal bearings, in order for the device to spin up to high rotational speeds.

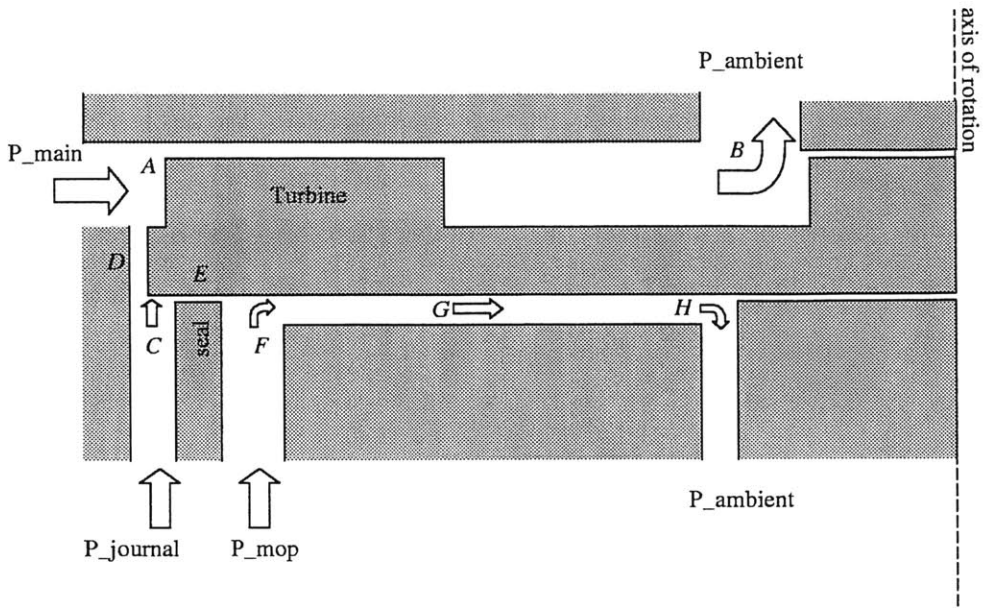

Figure 4-8: Schematic of forces acting on rotor.

Microbearing rig changes (such as with less journal bearing pressure) then the net axial force would change accordingly. Figure 4-9 below is for the operation of the Microbearing rig following a pressurization schedule that has worked well so far. The Matlab script for this computation is included in Appendix A.1.

This suggests that the design thrust bearings must be able to support an downward-pushing rotor at below approximately 300,000rpm and an upward-pushing rotor above that speed. The current build of the Microbearing, using hydrostatic thrust bearings, has the aft thrust bearing with a larger diameter than the forward thrust bearings[8]. With the net force pushing upwards on the rotor at high speeds, there is an incentive to design the forward thrust bearings with a larger diameter than the aft. However, as an initial device to test the operation of the hydrodynamic spiral groove thrust bearings, a symmetrical set of thrust bearings would teach us more of the spiral groove bearing effects—especially when different configurations of hydrodynamic and hydrostatic thrust bearings are involved[9].

[8]This is to accommodate the additional attraction force from the electrical motor at the aft side.

[9]Detailed description of the experimental matrix of hydrodynamic and hydrostatic thrust bearings is listed in Section 5.2.1.

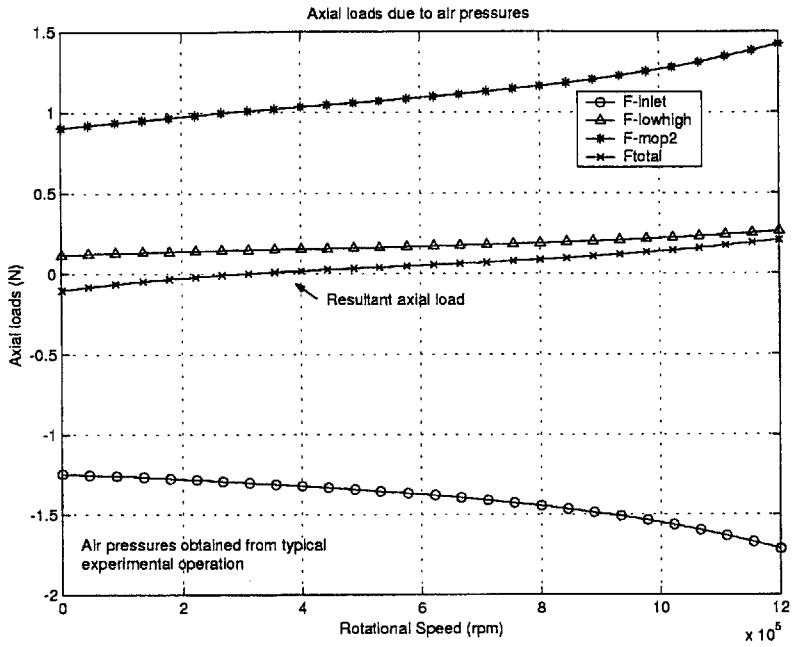

Figure 4-9: Axial load on rotor versus rotational speed. The resultant load is pushing downwards on the rotor at low speeds, but upwards at speeds above 310,000rpm.

4.4 Optimized Design

With the required load capacity of the spiral grooves determined, the geometry of the spiral grooves bearings was manipulated for optimal load capacity and stiffness. It was basically a seven degrees of freedom design space where the variables are: (1) number of grooves k, (2) outer radius of spiral r_2, (3) inner radius of spiral r_1, (4) depth of groove h_o, (5) gap of thrust bearing h_2, (6) spiral groove angle α, (7) ratio of groove-ridge width γ. Other performance "indicators" such as drag and axial natural frequency[10] were also investigated.

Working from Equation 4.12, a parameter sweep was peformed—the resulting load capacities, from varing a single parameter at one time, are shown in below Figure 4-10. Parameters that might affect each other are coupled together in the investigation. The following observations can be made:

[10]Computed as a linear spring-mass system from the stiffness coefficient.

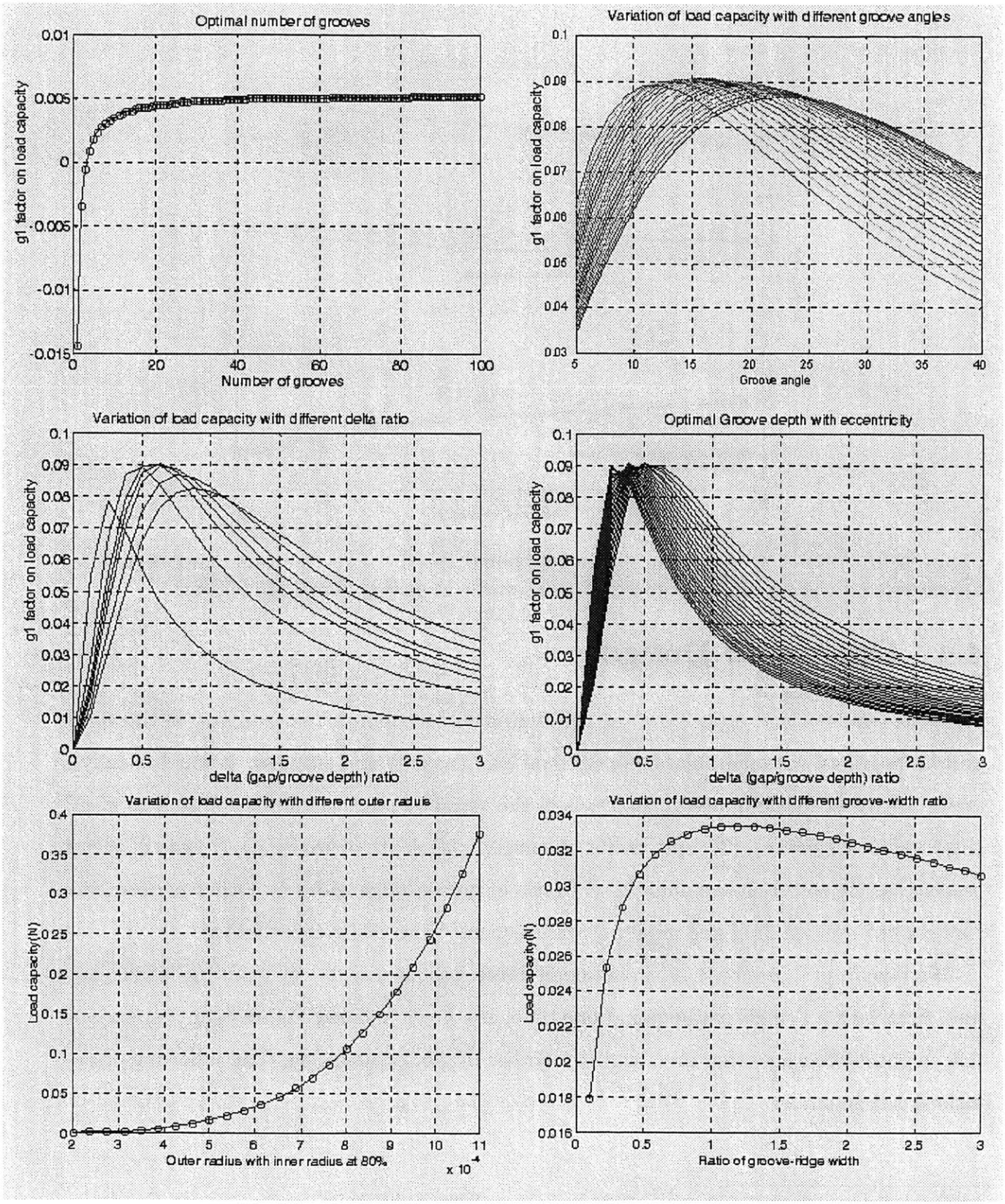

Figure 4-10: Variation of design geometries on the load capacity

- Increasing the number of grooves k increases the load capacity, while increasing the number above 50 does not have much effect.
- The optimal groove angle α, when individually varied, peaks off at about 26^o—an increase above that results in lower load capacity. An optimal α of 16^o is later chosen considering other design parameters.
- Optimized δ lies within the 0.3 to 0.9 range, depending on the groove angle α. Figure 4-10 seems to suggest δ at 0.63.
- Different eccentricities of the bearing leads a different optimized δ. To keep the load capacity relatively large for differnt eccentricities, we would instead pick δ at 0.42.
- Decreasing the bearing gap h_2 increases the load capacity significantly, since W_t is proportional to $\frac{1}{h_2^2}$. As small a gap as can be tolerated (page 103) should be incorporated.
- Increasing the outer radius r_2 of the spiral leads to a quartic increase in the load capacity. Inner radius r_1 should be kept at 80% of the outer radius for stability issues (Section 4.6).
- The optimal groove-to-ridge width γ lies at about 1.2 for our design.

Our only geometric constraint here is the forward thrust bearing radius, which is kept at the current radii of 700um to reduce the number of changes[11] to the current MicroBearing device. The aft thrust bearing radius, on the other hand, could be modifed with less mask changes. With the intent of maximizing the load and maintaining the stiffness at a respectable level(Figure 4-14), the optimized geometry is summarized here:.

- number of grooves $k = 50$;
- $\alpha = 16^o$;

[11] Changing the forward thrust bearing radius would mean changing all the masks for the top three wafers, and would result in different operating conditions.

- $\delta = 0.42$;
- h_2 minimal = 1um $\Rightarrow h_0 = 2.4$um;
- $r_2 = 700$um $\Rightarrow r_1 = 560$um for λ fixed = 0.80 (for stability) (Section 4.6);
- $\gamma = 1.2$.

We note again that, in our design, both forward and aft thrust bearings are identically symmetrical as a baseline design to investigate the effects of the spiral grooves.

Comparison of these optimized design values to others in literature [55, 47] places us in the mid-range between these studies—α between 14 to 17.5 and γ at 1.05 to 1.60. We found δ to be at 0.42 for our optimal value, compared to the previous authors' values of 0.33 to 0.35. This is because we kept λ at 0.80 as a simple gage into stability[12] ([55], MTI Figure 6.3.9), whereas the authors have optimized their values at λ between 0.4 to 0.7.

The specific resulting performances are computed in Appendix D.1, along with the optimized design, for reference. We illustrated here, in Figure 4-11, a graphical representation of its performance and, in Figure 4-12, a collapsed 2-d form of the load capacity. We observed that there is no load capacity at zero eccentricity because of the symmetric thrust bearings. For a given speed, there is an increased load capacity[13] for increased eccentricity—this increase in load capacity becomes more prominent at high eccentricities[14]. The increase in load capacity with rotational speed suggests a stronger thrust bearing as we operate at higher speeds.

[12]Dynamic stability issues presented in Section 4.6.

[13]On the order of a quadratic increase between 50% and zero eccentricity, with approximately 0.38N at 50% eccentricity and at 1.2million rpm.

[14]Unlike the journal bearing modeling, we chose to limit ourselves to "high" eccentricities of 0.50, given that our thrust bearing gap is 1-2um, for precaution against rarefaction effects.

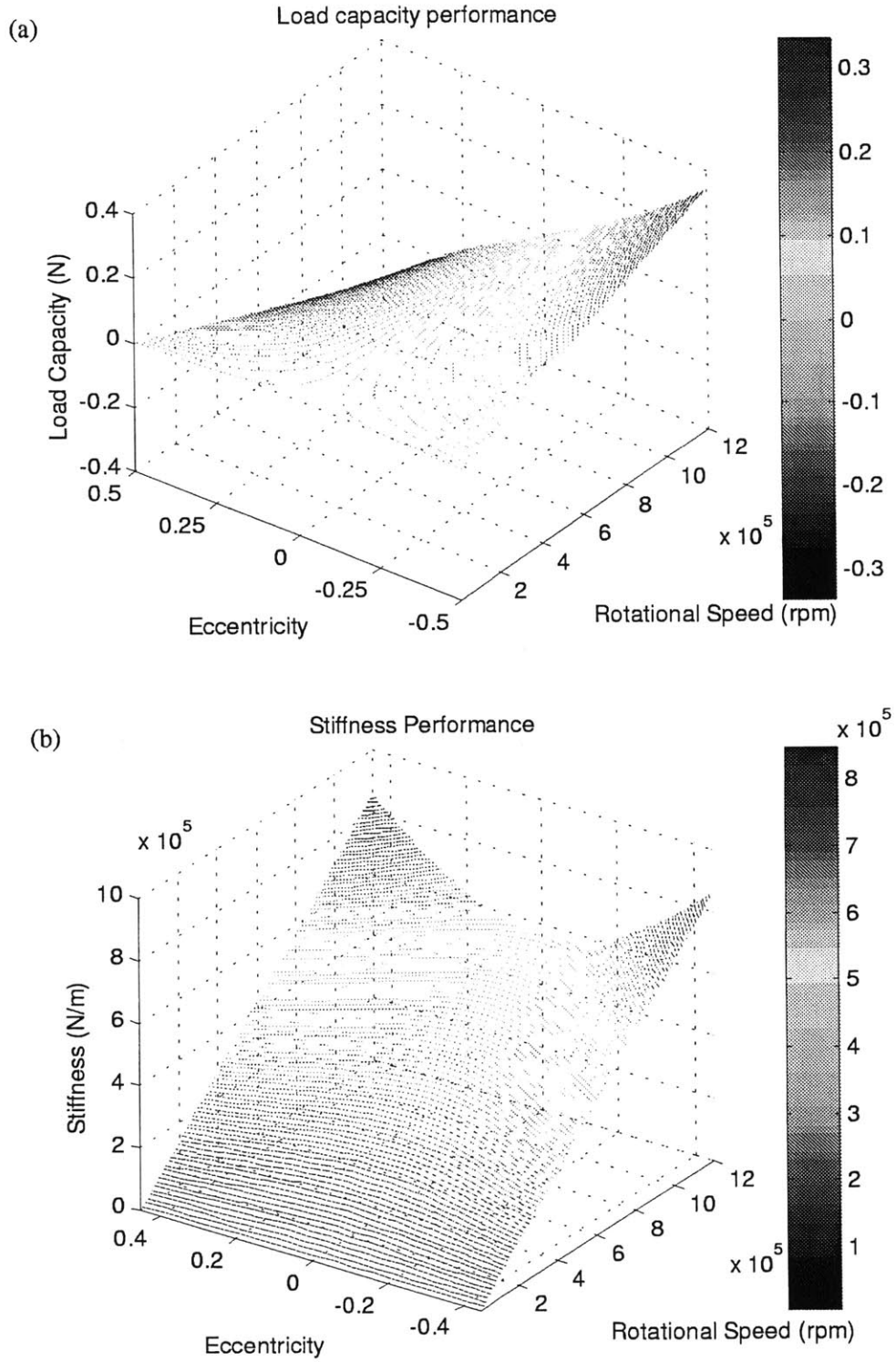

Figure 4-11: Optimized design performance of load capacity and stiffness.

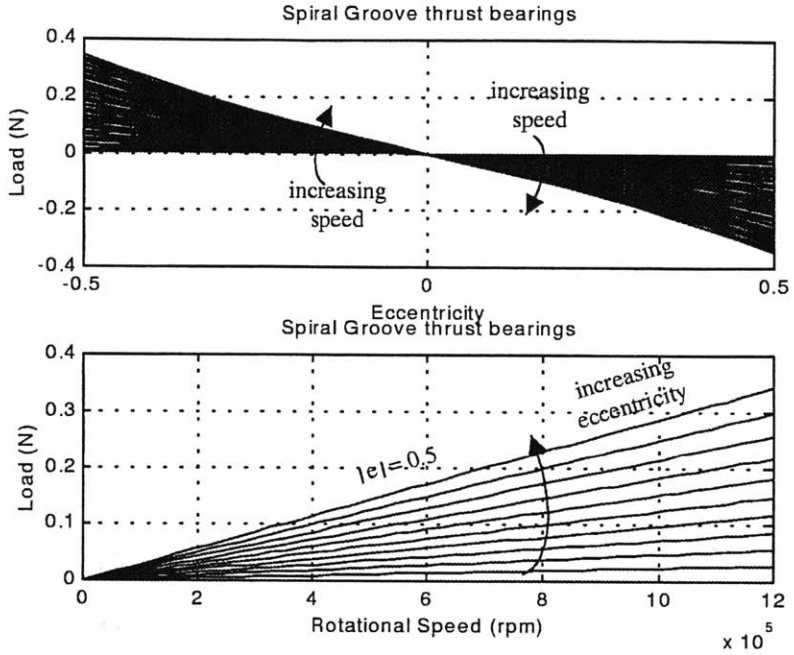

Figure 4-12: Optimized design performance against operating conditions.

Furthermore, other performance indicators predicted are the stiffness, the natural frequency from an associated linear spring-mass system, and the drag. This is appended in Figure 4-13. Note that the drag increases quadratically with speed (per Equation 4.13). In addition, the natural frequency drops to less than twice the rotational speed above 925,000 rpm, though it is still above the critical speed. The stiffness is relatively weak at low speeds, suggesting a possible need for providing stiffness through other means during the spin-up[15]. Figure 4-14 shows a comparison of the stiffness from hydrodynamic spiral grooves with the hydrostatic thrust bearings. The hydrostatic stiffness is dependent on the external pressures, although independent on the rotational speed. On the contrary, the hydrodynamic stiffness increases with rotational speed and has the potential of achieving a larger stiffness than a hydrostatic stiffness (of 73psig external pressuization) at above 860,000rpm. We also note the similarity of our hydrodynamic stiffness computation to that suggested by Hamrock [34, 33].

[15]Section 4.5 discusses means for possibly achieving this transition.

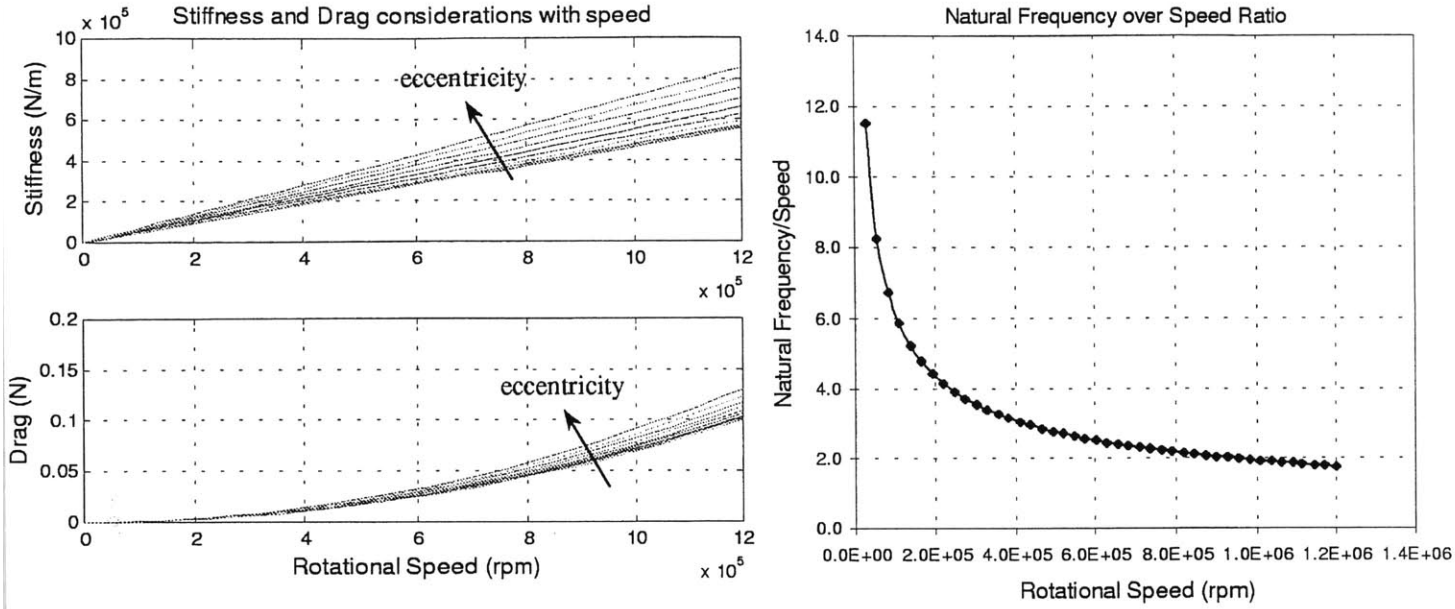

Figure 4-13: Stiffness, Natural Frequency and Drag of the optimized design.

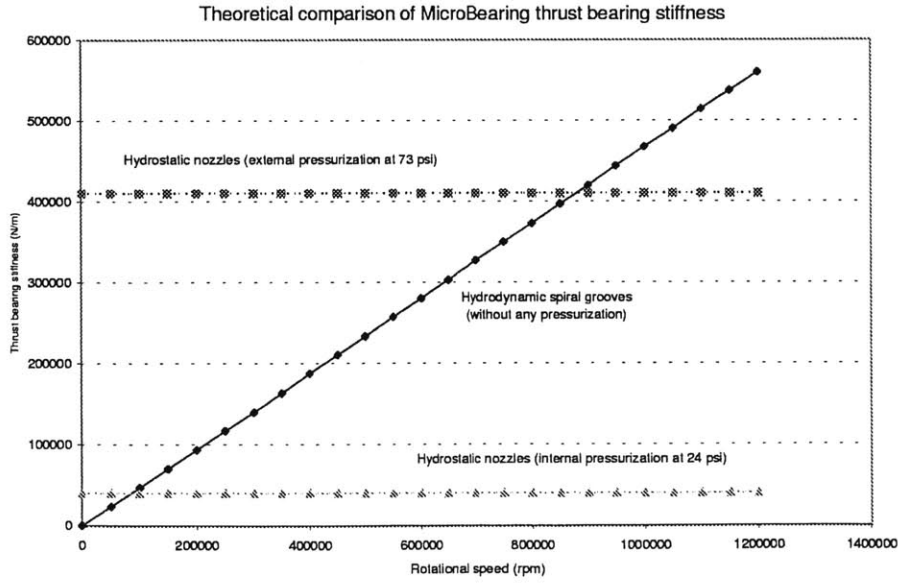

Figure 4-14: An overview of hydrostatic and hydrodynamic thrust bearing stiffness.

The main correction factor g_1 and the end correction factors $C_{1,2}$ are presented in Appendix D.2 as a check against Muijderman [47]. A sample source code for the hydrodynamic spiral grooves computation is listed in Appendix A.2.

Thus given our optimized geometry and performance indicators, the "lift-off" speed—at which the spiral grooves would provide the required axial thrust (Section 4.3)—is determined as seen in Figure 4-15. This lift-off speed is determined to be approximately at 164,500 rpm. This rotational speed is relatively achievable with the current Microbearing devices amd thus comfortable for a first demonstration of hydrodynamic spiral grooves on microdevices.

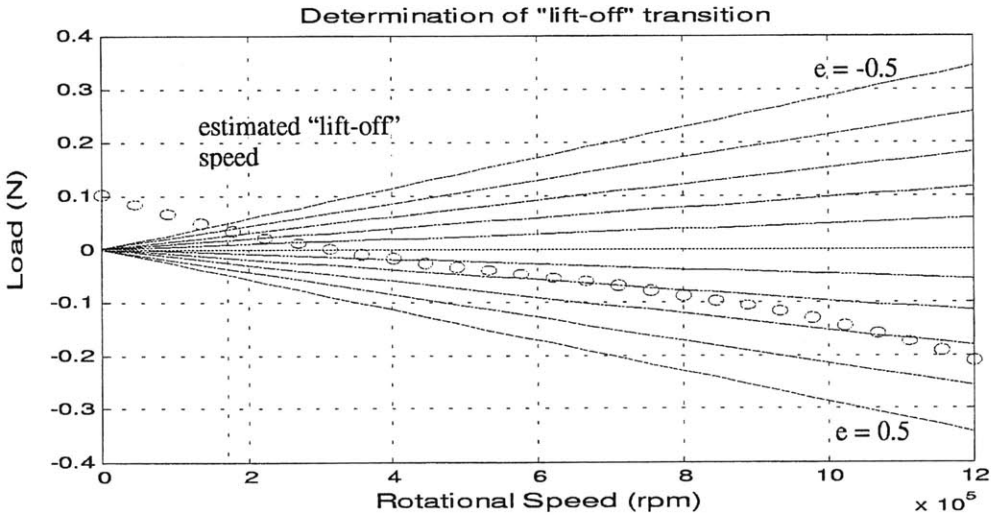

Figure 4-15: The ovals represent the net experimental axial load on the rotor without the thrust bearings; the lines represent the theoretical load capacity from the spiral groove thrust bearings. The "lift-off" speed is checked when the experimental axial load falls within the theoretical load capacity of the thrust bearings at 50% eccentricity.

4.5 Hybrid mode

To allow operation at low speed and to ensure the ability to reach "lift-off" speed, the bearings were designed to include an externally pressurized stiffness. This external pressurization can be valved off for transition into a pure hydrodynamic mode once the required "lift-off"

speed is reached.

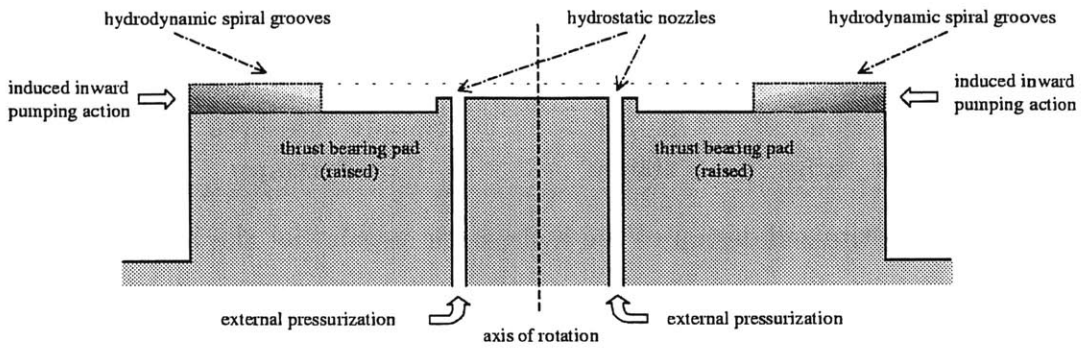

Figure 4-16: Cross-sectional illustration of the hybrid mode.

To provide this additional stiffness initially, a hydrostatic inherent restrictor thrust bearing (identical to the hydrostatic bearing in previous devices) is added to the hydrodynamic thrust bearing. This then creates the hybrid mode that allows us to validate the operation of the hydrodynamic spiral grooves. The modeling of the hydrostatic thrust bearing is achieved using a model provided by Jacobson. This model formulates three serial restrictors—orifice, inherent orifice, and radial—to model the pressure profile in the flow. Other codes developed by Orr [54] and Walker[16] have also modeled the hydrostatic thrust bearing.

Positioning the hydrostatic nozzles at the location in previous pure hydrostatic designs would place the nozzles at the middle of every other groove. This might affect the flow passage as it enters the spiral grooves. Instead, we opted to position the nozzles at an inner radial location (closer to the center of the thrust bearing pad) from the spiral grooves. The original depth (at the center of the thrust bearing pad) of a purely hydrodynamic spiral groove is $3.2\mu m$. However, in order for an adequate hydrostatic stiffness and load, we raised the center of the thrust bearing pad back up to approximately $1\mu m$ for an appreciable stiffness. The resulting cross-sectional view of the hybrid mode is illustrated in Figure 4-16. The raised height at the center of the thrust bearing might again affect the performance of

[16]Dr. Richard Walker of CS Draper Lab employed a code by Mechanical Technology Incorporated for the computation.

Parameter	*Optimized result*	*Parameter*	*Derived results*
Length	100um	Axial Load Capacity	0.199N
Diameter	10um	Stiffness	131,400N/m
Number of orifices	20	Flowrate	32.5sccm
Bearing film depth	1.5um	% Press drop at orifice	35%
Orifice radial location	350um	Supply Pressure	58.78psig
Thrust bearing pad radius	400um	Exit Pressure	21.75psig

Table 4.1: Optimized design of the hydrostatic nozzles for the hybrid mode.

the spiral grooves—we thus chose a radial diameter of the center raised height as small as possible, while not deviating too much from the current design.

Given these general guidelines, we employed Jacobson's model and iterated through the matrix of possible designs. The resulting optimized design is summarized in Table 4.1. A note[17] in using the model is that the circumferential distance between the nozzles should be significantly smaller than the radial outflow length in order for a uniform radial pressure profile at the nozzle location to be valid. In addition, we set the exit pressure at $21.75psig$, instead of at ambient, due to the pressure buildup from the spiral grooves.

We note the stiffness is highly dependent on the thrust bearing gap and, hence, the need for a different depth from the $1.0\mu m$ overall shallow etch across the thrust bearing pad. Finally, as will be discussed in Section 5.2.1, we also incorporated a purely hydrodynamic and a purely hydrostatic design into the final fabrication for reasons of testing and calibration.

4.6 Spiral grooves stability

4.6.1 "Absolute" Stability from MTI

In the 1972 design notes—"Design of Gas Bearings"—by the Mechanical Technology Incorporated [42], Malanoski and Pan [55] listed a chart that suggests an "absolute" stability

[17]Personal communication with Jacobson.

for hydrodynamic spiral grooves. While the authors did not include the derivation of this stability curve (Figure 4-17) in the MTI publication, the analysis seems to be follow from their earlier work in 1965 [41]. As a general guide for the first iteration of the design, we follow along this chart while refining our stability computation later in Section 4.6.2.

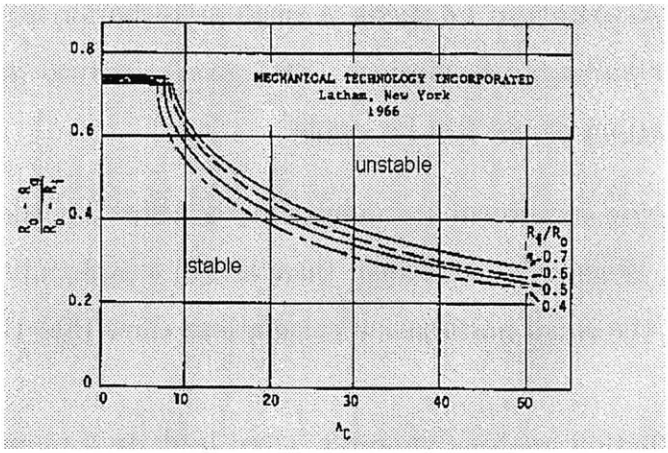

Figure 4-17: Conditions for stability as suggested by Mechanical Technolgoy Incorporated (adapted from Malanoski and Pan [55]).

With the ratio of spiral groove radii plotted against the compression number Λ_c, the required radii for absolute stability of the spiral groove thrust bearings are denoted. Our design has $R_i = 0$ and compression number Λ_c at 33.8[18] for rotational speed at 1.2 million rpm. These compression numbers thus point to the radii ratios at less than 0.5 for stability. We pick conservatively the $\frac{R_o - R_g}{R_o - R_i}$ ratio at 0.2 as a design constraint—this leads to $\frac{r_1}{r_2}$ of 0.8 for our device.

4.6.2 Dynamic Stability

To further investigate the stablity issues of an inward pumping spiral groove thrust bearings, we look into the 1987 and 1990 publications by Constantinescu and Galetuse [14, 15]. They provide two stability methods which are used as a check:

[18]Compression number Λ_c is linearly proportional to rotational speed; therefore at 14.1 for 500,000rpm.

Air-hammer analysis This computes a compression number[19] limit $\Lambda_c^\star$ such that the bearing is unconditionally stable [13, 39]. The main approximation in this method is that of the instantaneous pressure distribution retaining the same form as the static distribution[20].

Standard small perturbation analysis A small perturbation is included and the system analyzed under harmonic oscillations. This gives a critical mass number $\bar{M}_{cr}$ under which the vibrations would still be stable.

Thus, when the bearing compressiblity number Λ_c is below $\Lambda_c^\star$, the bearing would be unconditionally stable. When $\Lambda_c^\star$ is exceeded, there is still a probability for the bearing to be stable—this is when the small pertubation calculations show that the mass is smaller than $\bar{M}_{cr}$.

The small perturbation analysis, however, often leads to a required mass that is much smaller than of practical interest [14]. For example, a sample calculation on the Microbearing rig shows Λ_c at 33.84 for 1.2 million rpm. Our previous optimized design parameters (Section 4.4) has λ at 0.80 and $1/H$ at 3.4. From the charts in Constantinescu [14], this gives a $\bar{M}_{cr}$ of approximately 0.01, translating to a critical mass M_{cr} of 0.13μg. Our device already has a mass of 11.3mg, implying that our device is unstable at high speeds and a much smaller mass is required for stability.

Alternative, we can use the air-hammer analysis to determine *when* the spiral groove would become unstable. A critical compression number$\Lambda_c^\star$ obtained by Constantinescu analytically is expressed as:

$$\Lambda_c^\star = \frac{4A_{0,i}}{f_0 f_{s0} |\cos\beta| (A_{1,i}A_{2,i} - A_{3,i}A_{4,i})} \tag{4.14}$$

[19]Malanoski and Pan had Λ_c as the compression number and not compressiblity number. We use here the former for consistency in this work.

[20]Constantinescu and Galetuse [15], Appendix II.

Parameter	*Derived result*	
	Config a	Config b
$\Lambda_c^\star$	22.78	41.87
Speed at which $\Lambda_c^\star$ was exceeded	819,000 rpm	1,494,000 rpm

Table 4.2: Derived results on stability parameters.

where the terms $A_{n,i}$ represent the Constantinescu and Galetuse coefficients for $n \epsilon [0, 4]$ and

$$i = \begin{cases} a & \text{outer spiral groove with center chamber raised} \\ b & \text{outer land area with inner spiral groove, including shaft at inner chamber.} \end{cases}$$

The expressions for the coefficients can get quite lengthy and is listed in the nomenclature reference (page 17). The terms f_u and f_{s0} are also parameters listed in the nomenclature section. The derived results, as summarized in the Table 4.2, for the two configurations previously mentioned suggests the speed at which the bearing goes unstable. We note here that, while dynamic stability is computed with two configurations of spiral grooves, our design (primarily that shown in Muijderman) is not identically the same as the configurations presented[21]. Therefore, these two configurations serve to give us a design range where dynamic stability would be an issue.

In addition, a fully optimized geometry spiral groove bearing leads to the smallest Λ_c (i.e. easier to become unstable). To further improve on the stability range for future designs, we would consider departing (again) from the optimized geometry by decreasing the groove depth h_o at the expense of load capacity.

Lastly, we also bring up that an outward pumping design has a much smaller h_o and thus the compression parameter Λ_c (proportional to h_o^{-2}) is significantly larger, although $\Lambda_c^\star$ would only be slightly larger [15]. An inward pumping design would thus still be preferred on stability issues.

[21] Very similar to configuration $(i = a)$, we have the center land lowered and raised again for the hydrostatic thrust bearings.

4.7 Further remarks on hydrodynamic thrust bearing design

4.7.1 Rarefaction Effects

Using continuum analysis for a $1um$ micro-channel requires a check on the rarefaction effects on the gas. Typically, the Knudsen number serves as a simple check and is given by [7]:

$$Kn = \frac{\lambda}{L} \tag{4.15}$$

where λ here is the mean free path and L the characteristic length in question. The mean free path λ is expressed in terms of effective molecular diameter d, thermodynamic temperature T, pressure P, Boltzmann's constant κ, and gas molecular number density n, as:

$$\lambda = \frac{1}{n\sqrt{2}\pi d^2} = \frac{\kappa T}{P\sqrt{2}\pi d^2}. \tag{4.16}$$

At standard conditions, the air molecular number density[22] n is $2.68699 \times 10^{25}\, m^{-3}$ and the effective molecular diameter[23] d is $3.7 \times 10^{-10}\, m$. This puts the mean free path λ of equilibrium air at $6.1 \times 10^{-8}\, m$—at the increased pressures of our spiral grooves of between $1.38\, atm$ and $4.08\, atm$, the new λ stands at $4.42 \times 10^{-8}\, m$ and $1.50 \times 10^{-8}\, m$ respectively. This yields the Knudsen number at between 0.015 and 0.04 for our $1um$ micro-channel. Since this means the mean free path λ is small compared with unity[24], we neglect the effects of rarefaction and assume the continuation of the continuum assumption.

In addition, the mean molecular spacing δ is obtained quite simply with:

$$\delta = n^{-\frac{1}{3}}. \tag{4.17}$$

[22]When this molecular number density is expressed in per cm^3, the resulting number is known as Loschmidt's number n_0 [7].

[23]From the theoretical hard elastic sphere assumption.

[24]A usual paramemter to use is for Kn < 0.1 for the continuum assumption to be valid.

The mean molecular spacing δ under standard conditions is, as commonly stated, $3.3 \times 10^{-9}\, m$. The ratio of δ/d at 8.9 holds the dilute gas assumption as valid[25] and the ratio of L/δ at approximately 300 puts us in the zone where there should be insignificant fluctuations[26] of the macroscopic quantities.

Nevertheless, to avoid the dangers of rarefaction (or the "lock-up" hydrostatic effect that is not well-understood[27]), we kept our computation to a maximum eccentricity of 50% of the 1.0um gap, with the intention of operating within these bounds.

4.7.2 Helmholtz resonance and Rotor wobble

The necessity of including the hydrostatic nozzles during the spin-up operation creates a possible Helmholtz resonator with the thrust bearing plenums. The Helmholtz resonator effect is commonly discussed [37, 5, 60] and a simple[28] form of the resonant frequency $W_{n,helmholtz}$ is computed as:

$$W^2_{n,helmholtz} = \frac{a_0^2 A_{orifice}}{V_{plenum} L_{orifice}} \tag{4.18}$$

where a_0 is the speed of sound under standard conditions, $A_{orifice}$ the area of the orifice, $L_{orifice}$ the length of the orifice, and V_{plenum} the volume of the thrust bearing plenum per nozzle. For an orifice of $5um$ radius-$100um$ length and a plenum of $500um$ radius-$350um$ depth (applicable to both current forward and aft thrust bearings), the resulting Helmholtz frequency is listed in Table 4.3.

Both methods, in Kerrebrock and in Beckwith, Marangoni and Lienhard, to compute the Helmholtz frequency give a similar result of approximately 19 to $20kHz$. This computation therefore suggests a possible failure at 1,140,000rpm where the rotational frequency, if rotation in a conical mode, is just about resonating at the Helmholtz frequency of $19kHz$.

[25] We require $\delta/d \gg 1$ for the dilute gas assumption [7].

[26] For our device under standard conditions, a L/δ of > 100 is sufficent [7].

[27] See Section 2.4.

[28] Another form is listed in Beckwith, Marangoni and Lienhard [5], but can be readily reduced to Equation 4.18.

	Orifice area (m^2)	*Plenum volume* (m^3)	$W_{n,helmholtz}$ [37] *(hz)*	$W_{n,helmholtz}$ [5] *(hz)*
Derived results	7.86×10^{-11}	5.99×10^{-12}	19785.03	19050.95

Table 4.3: Derived results of the Helmholtz resonance of the hydrostatic thrust bearing plenums. The resonant frequencies are computed from two slightly different methods.

Without affecting the stiffness of the hydrostatic nozzles in the hybrid thrust bearing, this frequency could be increased by decreasing the volume of the thrust bearing plenum drastically. Our initial device, as a feasiblity study of a hybrid mode for possible "lift-off" at low speeds, serves as an instrument to understand the interaction between the hydrostatic and hydrodynamic operating modes at very high speeds. In addition, the plenums might possibly be removed in future devices, eliminating the Helmholtz resonance altogether.

We accept, however, the possible Helmholtz resonance in our design since the aim of this initial device is to demonstrate the functioning of the spiral grooves. In addition, the plenums might possibly be removed in future devices, pending the experimental performance of the spiral grooves. This exercise therefore serves to investigate the resonant effects of the thrust bearing cavity (when attenuating the pressure effects) as a feasibility study of a hybrid mode at low speeds.

Here we note the hydrostatic thrust bearing in the previous Microbearing devices are also subjected to Helmholtz resonances since the plenums are present. The difference in the earlier devices is the presence of a continuous flowrate through the plenums which are absent in our hybrid thrust bearing when the external hydrostatic pressurization is switched off.

A short note on the rotor wobble: we refer here to the "gyroscopic stiffening" described in rigid body modelling [74, 11]. The tilt stiffess of an oblate rigid body increases very rapidly with rotational speed. The conical mode is significantly reduced with large angular momentum, though it is not immune to the large external torques. With our device at

Rotational Speed (rpm)	*Predicted effect*
164,500	"Lift-off" of rotor expected within ±50% ecccentricty
819,000	Dynamic stability becomes an issue
1,140,000	Helmholtz resonance works into appreciable range

Table 4.4: Operation summary, with predicted causes of failures at high speeds.

such high rotational speeds, we do not expect a problem with the tilt stiffness of the spiral grooves.

4.7.3 Summary and Further Improvements

We began this chapter with the rationale for creating a hydrodynamic thrust bearing and exploring the different kinds of hydrodynamic thrust bearings available to us. Showing the conceptual development of the spiral grooves, we went on to model the spiral grooves subjected to optimization of certain performance indicators. Section 4.3 cites the necessary loads for "lift-off" of the rotor and indicates how the computation was carried out. The design is optimized for load capacity and stiffness within the imposed constraints. Drag and natural frequencies are also counterchecked in the final design. A "lift-off" speed is cited by performing a simple axial thrust balance.

Concerns with low load capacity at low rotational speed brought in the need for a hybrid mode (Section 4.5), wherein the included hydrostatic nozzles are also optimized for stiffness. Moreover, stability analysis showed that, while the initial stability computations from Malanoski and Pan (Section 4.6.1) indicate a λ of 0.8 would be sufficient, further analysis into dynamic stability suggests that the bearing would become unstable at approximately 819,000 rpm. Further improvements on stability could be achieved by decreasing the groove depth (and drifting further away from an optimal design). We also note the effects of rarefaction and Helmholtz resonance earlier in this section. The predicted operation of the hydrodynamic thrust bearings is summarized in Table 4.4.

To decrease the "lift-off" speed of the MicroBearing, we can increase the load capacity by increasing the thrust bearing pad radii. Equation 4.12 suggests the load capacity to be proportional to r_2^4. Increasing the thrust bearing pad radius r_2 has little negative effects on the thrust bearing except a probability of increasing imbalance load for the same front-to-backside etch misalignment. The only constrain, which we have to keep in mind when increasing the thrust bearing pad radius r_2, is to keep the inner radius r_1 at 80% of r_2 as a simple stability check[29].

As an initial device to prove the functionality of a spiral groove bearing, our design was chosen for maximum load capacity (within the bounds of our thrust bearing pad radius) and stiffness to enable an achievable "lift-off" speed. This "lift-off" speed has to be one for which the current MicroBearing rig can achieve. The possibility of the thrust bearings failing at high speeds due to stability and Helmholtz resonance issues could be designed around by moving away from the optimal design and changing the size of the hydrostatic plenums respectively. In order to effect minimal changes to the currently effective MicroBearing, the possible failures at high speeds are accepted, if not interesting to observe.

[29] A check on the dynamic stability can be implemented as suggested in Section 4.6.2. Moving away from the optimal design geometries would improve dynamic stability.

Chapter 5

Hydrodynamic Thrust Bearing: Experiment

Even if there is only one possible unified theory, it is just a set of rules and equations. What is it that breathes fire into the equations and makes a universe for them to describe?
—Stephen W. Hawking, A Brief History of Time, 1988.

This chapter covers the fabrication and testing of the hydrodynamic thrust bearing. We begin with a discussion of the modified fabrication process flow and include the actual fabrication results for our devices. We follow with a portrayal of the experimental procedures. Finally, we present the operational results of a purely hydrodynamic thrust bearing and a hybrid thrust bearing.

5.1 Fabrication of the Spiral Grooves

The fabrication process is adapted from the initial development of the MicroBearing Rig by Lin [40] and the Motor-Compressor Bearing Rig by Fréchette [31]. Much assistance in making the masks was given by Fréchette. Assistance in fabrication was provided by Xin Zhang[76]. We will detail the modified process flow, the new challenges in fabrication and

describe the fabricated device in this section.

5.1.1 Fabrication Process Flow

In addition to the existing fabrication challenges mentioned in Section 3.1 (on page 41), building the hydrodynamic spiral grooves introduces two additional shallow etches on each thrust bearing—a total of four shallow etches for the thrust bearing wafers.

The first shallow etch, on the second and fourth wafers, is desired at $1.0\mu m$. This produces the gap between the rotor and the thrust bearings. As the load capacity of the spiral grooves is strongly dependent on this gap (Equation 4.12), fabrication of this gap must be well-characterized and have tight tolerances.

The second shallow etch, also on the second and fourth wafers, is at a design depth of $0.5\mu m$. This brings the hydrostatic thrust bearing gap, in the hybrid bearings, to a final gap of $1.5\mu m$. Deviation from this depth, as seen in Section 3.1, is predicted to result in a lower stiffness of the hydrostatic thrust bearing. Therefore, the first two shallow etches on the thrust bearing have tight tolerances to meet the performance criteria.

The third shallow etch produces the hydrodynamic spiral grooves. An optimal etch depth of $2.2\mu m$ is desired from the model, though an etch depth of 2.0 to $2.4\mu m$ is tolerable with similar predicted load capacity and stiffness.

The final shallow etch produces the blade clearance ($12.5\mu m$) for the rotor on the second wafer and a generator gap ($8.5\mu m$) on the backside of the rotor[1].

These shallow etches on the FEP and the AEP wafers are depicted in Figure 5-1 and a complete fabrication process flow is compiled in Appendix B.1. Furthermore, we supplement in Appendix B.2 descriptions of the additional masks for this new device.

[1]This gap is increased from the initial specifications to reduce the drag on the rotor.

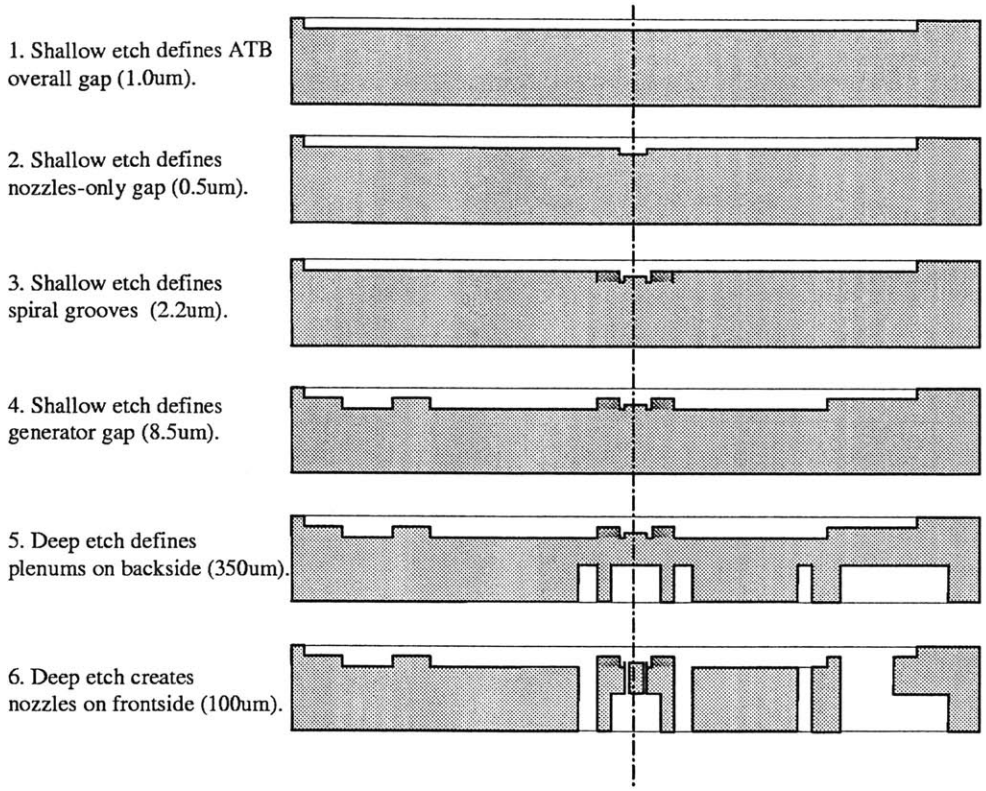

Figure 5-1: Fabrication process flow of Aft Thrust Bearing.

5.1.2 Fabrication Challenges of the Hydrodynamic Thrust Bearing

With the gap of the thrust bearing at only $1.0\mu m$ for the spiral grooves and the need to fabricate shallow etches to $0.5\mu m$, we explored two main concerns:

Wafer bow and total thickness variation Our commercial 4" n-type <100> $450\mu m$ wafers specifies a total thickness variation of less than $35\mu m$, and a bow of less than $205\mu m$. Measured experimentally, our batch of wafers has a thickness variation[2] of $4.25\mu m$. This translates to $0.045\mu m$ per mm diameter, if the thickness variation is monotonic and linear. For our thrust bearing diameter of 1.4mm, we would then expect a thick-

[2]Averaged across 25 measured wafers.

ness variation of $0.065\mu m$ across the thrust bearing. While this is adequate for our shallowest etch gap in question (of $1.0\mu m$), the thickness variation may not be linear nor continuous. We therefore decided to chose the wafers with the least thickness variation, typically on the order of $2\mu m$ for fabrication of our thrust bearings.

Achievability and Repeatability We need to achieve tight tolerances and high repeatability. Using the wealth of data built up from using the Applied Materials Precision 5000 (AME5000), we were able to achieve the $0.5\mu m$ and $1.0\mu m$ "shallow" etches fairly accurately and repeatedly. The required depths were etched to between $\pm 0.035\mu m$ and $\pm 0.15\mu m$ variations (depending on the critical need) by careful local characterization on the AME5000. Each depth was followed by an immediate depth measurement before proceeding with the next etch.

Figure 5-2 illustrates the spiral grooves and the hydrostatic thrust bearing nozzles in a hybrid mode on a single device wafer. We note the hydrostatic thrust bearing nozzles are on a raised pad to reduce the thrust bearing gap.

The remaining challenges of the fabrication process flow are the journal bearing etch and the final fusion bonding of the five wafers. While previously done in the MicroEngine program, the final step of fusion bonding—bonding a previously-bonded pair of wafers with the remaining three wafers—failed in our first attempt. The cause was determined to be due to a poor bond surface caused by warping (and thus a resultant unevenness) in one of the surfaces. Thorough inspection of surface flatness would be necessary before each fusion bonding attempt.

As the unevenness is rather large (on the order of 50-$100\mu m$), we proceeded with a second build of all the wafers. In this second attempt, we did not experience warping of the surfaces and we performed an extended-time pressing of the five wafers, along with raising the temperature to 500^oC for 10 hours, before thermal annealing. This extended-time pressing aided in improving the contact between the bond surfaces.

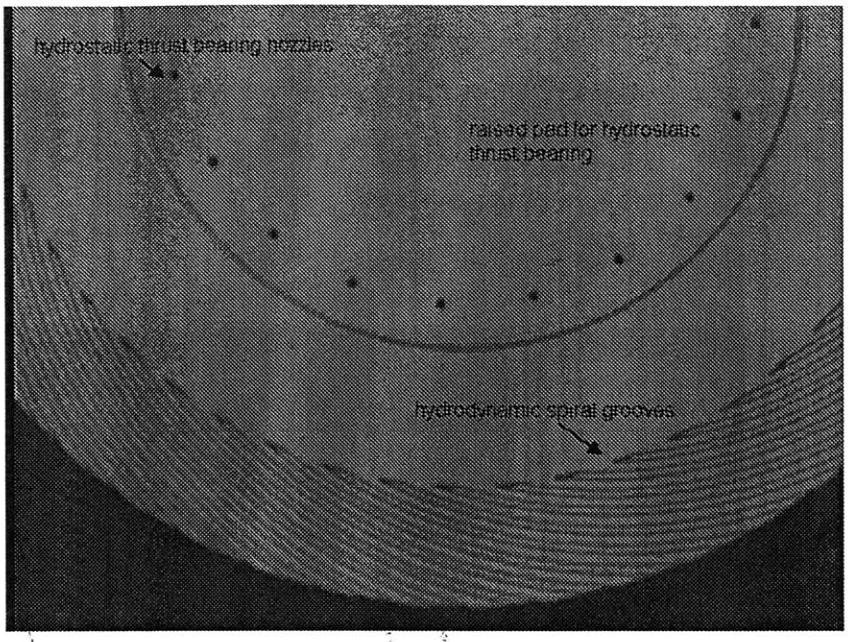

Figure 5-2: The spiral grooves and hydrostatic nozzles for testing in the hydrodynamic mode of operation. The nozzles are approximately $10\mu m$ in diameter and the groove width $35\mu m$.

Initial testing of the devices, however, showed that the journal bearing was not etched completely through in this second attempt. Though we even extended the etching time on the standard recipe by 45mins and an inspection for complete etching of the journal bearing was performed in several locations that provided visual access[3], the last $15\mu m$ of the journal bearing was still not etched away. The cause, determined to be the slower etch rate of the DRIE machine under heavy use, could be prevented by characterizing the etch rate just before the critical etch.

In the third attempt, we successfully completed the journal bearing etch[4] and employed the extended-time pressing to bond the wafers. Figure 5-3(d) shows the final results. In this third build, the location of the hydrostatic nozzles is at a larger diameter, $550\mu m$, instead of the desired $350\mu m$. This is because we used a previously completed forward thrust bearing

[3]Visual inspection, with backlighting of the journal bearing, could also be mistaken for complete etching with the thin $15\mu m$ Si remaining.

[4]This was done when the DRIE machine was under little use and, hence, at the usual quoted etch rate.

wafer in order to shorten the fabrication time[5]. The wafer, however, did not have the hydrodynamic spiral grooves on the front side and would not allow us to test hybrid thrust bearings on both the forward and aft sides. The spiral grooves at only the aft side will still allow us to test its characteristics during operation, where we would expect an additional load (from the spiral grooves) on the rotor.

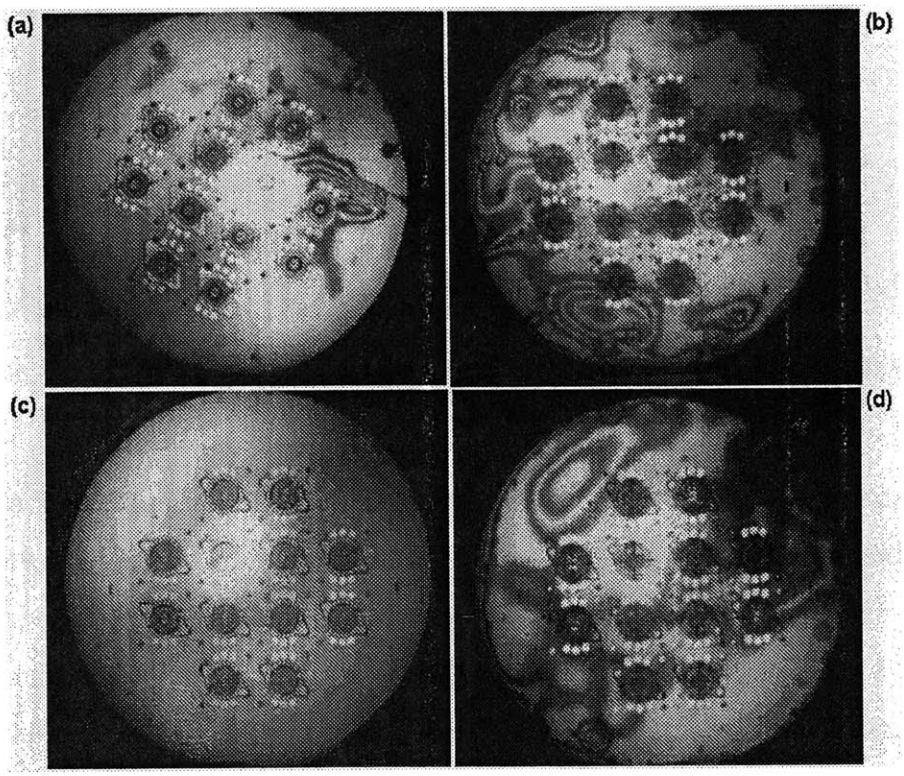

Figure 5-3: Results of wafer bonding in the hydrodynamic thrust bearing devices. The observed fringes are the "Newton rings" which are suggestive of the gap between two wafer surfaces. (a) Bonding between FTB wafer and rotor wafer, second attempt. (b) Final bonding between all five wafers, second attempt. (c) Bonding between FTB wafer and rotor wafer, third attempt. (d) Final bonding between all five wafers, third attempt.

[5]This greatly shortened the fabrication process time, as we would have to start from a blank wafer for the forward thrust bearing wafer, if we were to use the actual designed diameter.

		ATB		
		HS	HB	HD
FTB	HS	√	√	√
	HB		√	
	HD			

Table 5.1: Experimental combinations of hybrid configurations chosen for step-wise validation of funtionality of hydrodynamic spiral grooves. "HS" denotes hydrostatic, "HB" hybrid, and "HD" hydrodynamic.

5.2 Experiment

This section describes the initial tests on the device. We began with a description of the experimental matrix desired for testing, and the procedures to determine the hydrodynamic spiral grooves performances.

5.2.1 Experimental Matrix

With the possible inclusion of a hybrid hydrostatic-hydrodynamic thrust bearing, we examined the combinations of forward and aft thrust bearings that will enable us to demonstrate the functionality of the spiral grooves. The combinations chosen are shown in Table 5.1.

Each combination is chosen for a specific reason:

- **Hydrostatic-Hydrostatic**(I)**:** These dies act as an instrument to learn the operation of the modified MicroBearing Rig, and the characteristics of the new thrust bearing. They also serve as a control for this experiment.

- **Hydrostatic-Hybrid**(II)**:** These allow us to demonstrate the effects of spiral grooves on a single side of the rotor. We expect the forward thrust bearing flowrate to decrease (more rapidly than the above control experiment) as we spin up in speed.

- **Hydrostatic-Hydrodynamic**(III)**:** The configuration is fabricated in case of possible failure of the hybrid mode due to interactions of the hydrostatic inherent restrictors

and the hydrodynamic spiral grooves. It also allows us to "float" the rotor with just the hydrostatic forward thrust bearing and the aft Motor-Outer-Plenum, while observing the effects of the spiral grooves as we spin up in speed.

- **Hybrid-Hybrid(IV):** A final configuration for the ultimate testing of the spiral grooves with "lift-off" speed predicted at 164,500rpm, whereupon the hydrostatic external pressurization would be physically switched off.

Figure 5-4 shows the layout of each of these configurations in the MicroBearing build. The configurations are spread out in the wafer, in case of fabrication difficulties affecting a region on the wafer.

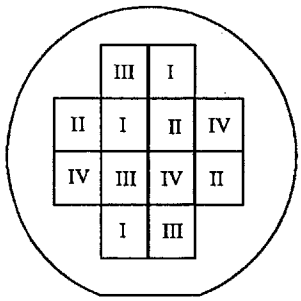

Figure 5-4: Planned wafer locations of different configurations for testing.

5.2.2 Estimating the Bearing stiffness

To estimate the spiral grooves stiffness, a control experiment was performed with a purely hydrostatic aft and forward thrust bearings device. Figure 5-5 shows the run-up of the control device. With the forward thrust bearing pressure fixed at 50psig throughout the test, the decrease in the flowrate (in a step-wise behaviour) was due to the rotor location moving upwards. This was because of increase in the journal bearing pressure from the aft side necessary to follow the operating schedule as we increase in speed. More importantly, we also notice a consistent slight increase in flowrate with rotational speed. This is due to

the additional turbine inlet pressure neccessary for the speed increase, a pressure that acts downwards on the rotor. This leads to a slightly larger gap in the forward thrust bearing and hence the increase in flowrate.

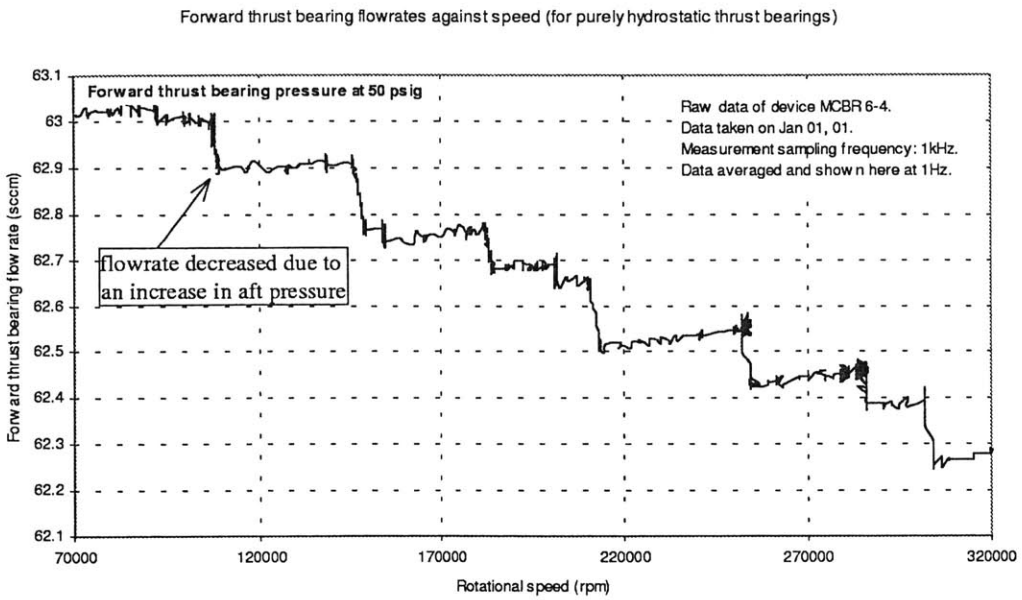

Figure 5-5: Operation of a purely hydrostatic forward and aft thrust bearing device as a comparison against devices with spiral grooves. The speed range displayed here is of interest for the spiral groove experiments.

We repeat the same operating conditions for the device with a hybrid aft thrust bearing. Both hydrostatic thrust bearing pressures and the externally pressurized Motor Outer Plenum[6] (MOP) are kept consistent with the previous experiment—the forward thrust bearing kept at 50psig and the MOP from 0.2psig to 1.4psig, depending on the speed. Figure 5-6 shows the FTB flowrates for the hybrid device. Here we note that the flowrate in Figure 5-5 is in the range of 62sccm as opposed to 12sccm as shown in Figure 5-6. However, we observe a 60sccm flow in the control device even when the forward thrust bearing gap is fully closed[7].

[6]This allows an independent control of the axial position. A schematic illustrating the position of the MOP is presented in Section 4.3 in Figure 4-8 for reference.

[7]The forward thrust bearing gap is fully closed when we apply a 100psig pressure on the aft thrust bearing and only about 20psig on the forward thrust bearing. This is because we observe no change in the forward thrust bearing flowrate when increasing the aft thrust bearing presssure (at pressures around 70psig onwards).

This suggests that there is a leak in the forward thrust bearing as often observed in our devices and that the large difference in the flowrates between the two experiments is not due to actual differences in thrust bearing gaps. However, this "off-set" difference between the control and hybrid thrust bearing devices makes it difficult to compare them on the same basis.

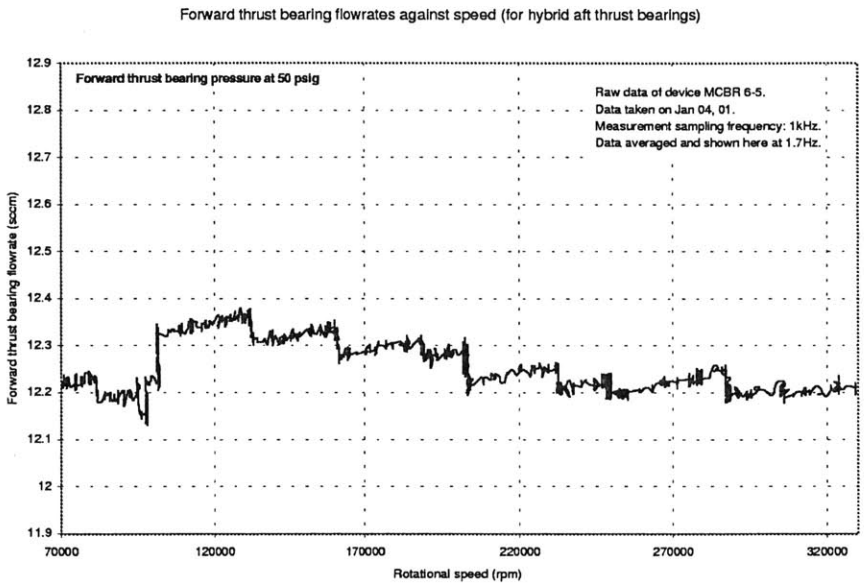

Figure 5-6: Forward thrust bearing flowrates for a hybrid aft thrust bearing during operation. Operation conditions are kept similar to the control experiment as shown in Figure 5-5.

Working with just the hybrid device, however, we could detect apparent changes in the flowrates. In Figure 5-7, we ran the experiment on the hybrid device with the forward thrust bearing at 36psig instead of 50psig. We noticed the change in flowrate is larger in each step. For example, at 270,000rpm, the change in thrust bearing flowrate is approximately 0.05sccm (at 50psig) and 0.10sccm (at 36psig) for the same device. The difference is small but real since the flowrate measurements, each as an averaged datapoint of 200 samples (sampled at 1000 Hz), have a standard deviation of 0.014sccm[8]. The larger flowrate change

[8]Calculated over 168 datapoints, the standard deviation is found to be 0.007sccm and we pick a two standard deviation for an approximated 95% confidence interval.

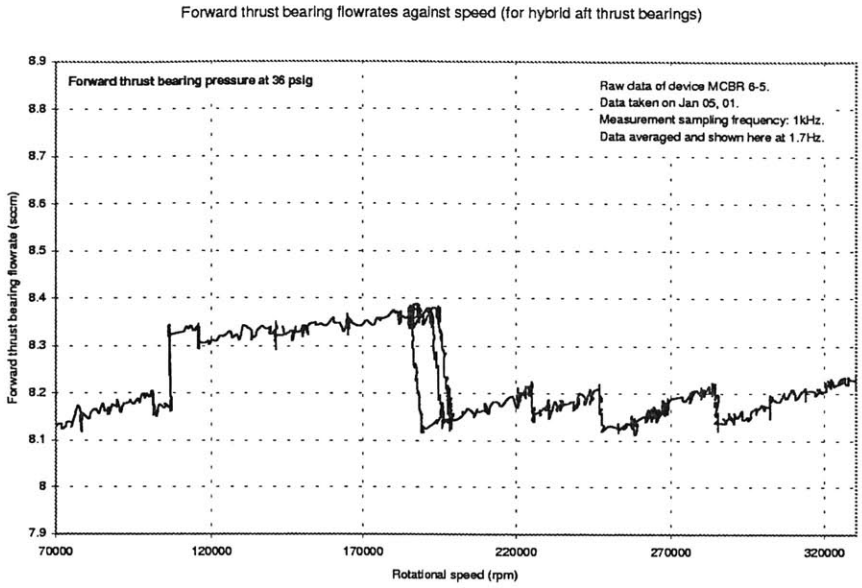

Figure 5-7: Forward thrust bearing flowrate against speed for the hybrid device, under a lower external pressurization (36psig) of the forward thrust bearing.

is due to the decrease in the overall axial stiffness (and of the forward thrust bearing) such that the rotor is displaced further to provide the necessary load capacity and, hence, the larger change in flowrate when increasing in speed. The decrease in stiffness due to the lower pressurization (of 50psig to 36psig) is estimated to be on the order of 25,500N/m from the theoretical model[9].

This method to estimate the additional stiffness due to the spiral grooves could be employed by comparing the difference in flowrate changes between a purely hydrostatic thrust bearing and hybrid thrust bearing. That is, by following the same operating schedule, we compare the change in flowrate as we increase up in speed. This change in flowrate can be mapped against the change in flowrate (for a specific device, say, the hybrid device) when the hydrostatic stiffness is deliberately lowered by supplying a lower pressure. However, with the leakage in the forward thrust bearing on our hydrostatic device, it was difficult to make comparisons between the flowrates. Other methods to estimate the stiffness include comparing

[9]We employed a hydrostatic thrust bearing model developed by Stu Jacobson.

the pressure-flowrate relationship for the hydrostatic mode with the experimental results, or comparing the change in forward thrust bearing flowrate as we increase the journal bearing pressure on the aft side. The first method was attempted; however, we observe that we could not implement it for a large range of pressures[10] due to the larger forward thrust bearing which has stronger response for increases in pressure. The second method is subjected to the same dependence on flowrate measurements as the current procedure. There is an intent to build a second batch of hybrid thrust bearing devices to characterize the hydrodynamic stiffness at different operating eccentricities and speeds.

5.2.3 Operation with a purely hydrodynamic thrust bearing

We next proceed to operate a purely hydrodynamic thrust bearing device. Given the larger measured thrust bearing gap in the device ($1.53\mu m$ instead of the design value of $1.0\mu m$), the hydrodynamic spiral groove model is computed again to refine the "lift-off" speed (as first discussed in Section 4.4, page 97) in a purely hydrodynamic mode. The lower stiffness, due to the larger than desired thrust bearing gap, results in the new "lift-off" speed around 190,000rpm instead of 164,000rpm. This is illustrated in Figure 5-8. The maximum eccentricity is set to $\pm$ 0.50 as an estimate and we note the experimental net axial forces (without the thrust bearings) is also predicted to exceed the load capacity of the spiral grooves at approximately 600,000rpm due to the larger fabricated thrust bearing gap. With the lowered stiffness and if we were to follow the previous experimental spin-up schedule, this then sets the upper limit for our hydrodynamic operation[11].

Figure 5-8 also shows, at low speeds, an insufficient load capacity to support the rotor—an expected result as the performance of the spiral grooves depends on rotational speeds. However, as we increase up in speed, the load capacity increases. To provide the initial load capacity, we had planned to employ MOP pressurization to correct for the downward

[10]This range experimentally attempted was between 37psig to 55psig; while theoretical plots suggest a larger range of pressure in order to see the shape of the pressure-flowrate relationship.

[11]Our current spiral grooves were designed to "contain" the axial loads up to 1.2 million rpm as shown in Figure 4-15.

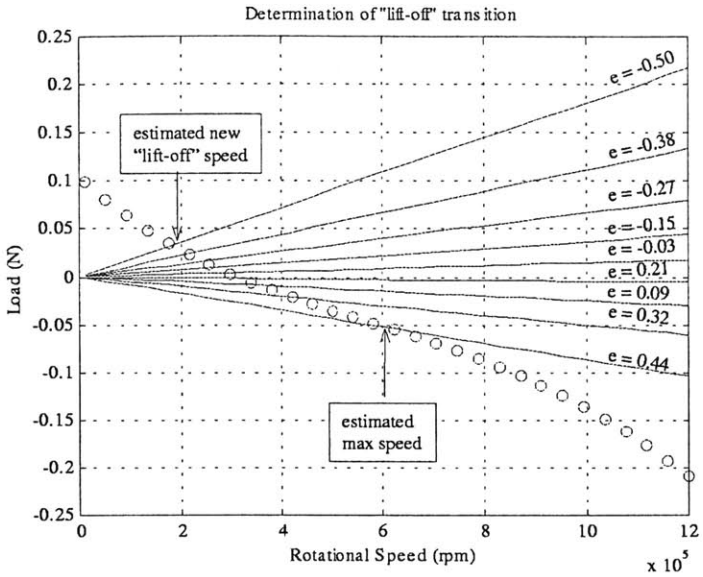

Figure 5-8: Model prediction of "lift-off" speed for a $1.53\mu m$ thrust bearing gap, instead of the $1.0\mu m$ design value. The dots depict the experimental net axial load without the thrust bearings forces, and the lines show the theoretical spiral grooves load capacity at different eccentricities.

force. Externally pressurized MOP was used in the initial experiments; however, we observed that, even when the valve was completedly closed off, there was a measured pressure in the MOP. More observations, including changing the valves and completely unplugging possible upstream pressure sources[12], showed a detectable pressure in the MOP when no external sources were possible. This pressure build-up was found to be due to a leakage between the MOP and the journal bearing through the MOP seal, and is present during spin-up of our MicroBearing devices[13]. This leakage is helpful in providing the required load capacity during low speeds and supports the net downward force due to the larger forward thrust bearing.

Figure 5-9 shows the spin-up operation with a purely hydrodynamic aft thrust bearing. We notice the rotational speed is relatively unstable between the 30,000 to 40,000rpm[14]. The

[12]The MOP piping to the device package was completely disconnected, except connections to the pressure transducer.

[13]A quick check on earlier devices also show this effect.

[14]We have also noticed this in our earlier purely hydrostatic devices and attribute this to excitation near

plateaus are the durations when more data is acquired, or when the journal bearing differential pressure is increased in order to facilitate increases in speed. The device eventually reached 100,000rpm in this operation before the device is finally spun down. This device spun up to 233,000rpm in later runs.

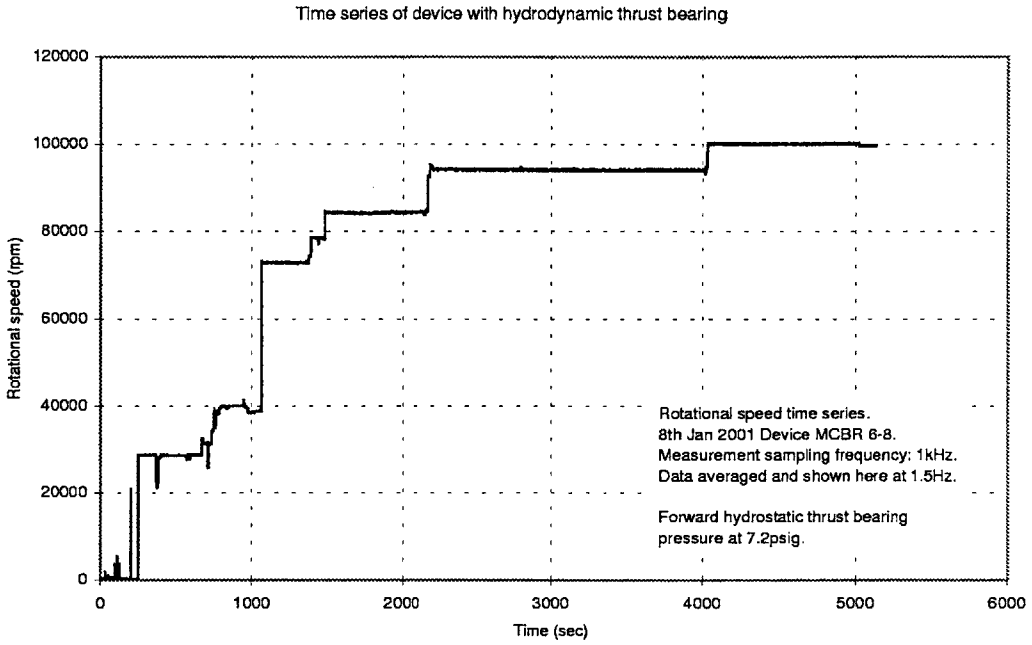

Figure 5-9: Time-series of a purely hydrodynamic thrust bearing operation. In this operation, the Motor Outer Plenum is completely shut-off and there is no aft hydrostatic thrust bearing.

The spin-down was performed because the hydrostatic forward thrust bearing in this device was leaky[15] and provided very low stiffness (and load capacity). Earlier characterizations suggest the leaky forward thrust bearing as the cause of difficulty in spinning up the device as main inlet pressure must be employed[16] to push the rotor down before the device

the journal bearing natural frequency.

[15]The forward thrust bearing flowrate reached the maximum of 200sccm at about only 7.4psig. This characteristic has been observed previously in the devices. This cause of leakage is suspected to be either incomplete bonding between the forward thrust bearing wafer and the rotor wafer, or a leakage through the thinnest part of the device internal piping wall (about 100um) due to over-etching. A simple flow test with a Si block in the device packaging showed no leakage, suggesting adequate o-rings and no leakage in the external piping.

[16]In the usual operation, a minute amount of main inlet pressure is enough to spin the device. Situations where the rotor begins without main inlet pressure are also very common.

begins to spin. In fact, during the initial experiments, the device crashed at low speeds when we decreased the main inlet pressure. The leaky forward thrust bearing and the lack of an aft flowrate also made it difficult to estimate the eccentricity of the rotor.

The device eventually ran up to 233,000rpm in a separate test designed to test rotor operation with only the aft thrust bearing. The computations, in Figure 5-8, show the net axial loads as downwards on the rotor at speeds below 300,000rpm. It was suggested to switch off the forward thrust bearing at sufficiently high speeds to demonstrate rotor operation with only the hydrodynamic aft thrust bearings. In our test, we attempted to switch off the forward thrust bearing at 100,000rpm. However, as the forward thrust bearing pressure is decreased to 3.5psig (from 7.1psig initially), the rotor began to decrease in speed drastically. We then steadily increased the speed and noticed that this "critical" forward thrust bearing pressure (in which the speed decreases drastically) fell to 2.7psig at 200,000rpm. At 233,000rpm, however, the device finally crashed as we were attempting to decrease the forward thrust bearing pressure to zero. We note, though, at 233,000rpm, the rotor was operating steadily at 2.7psig but crashed at around 2.4psig and thus the trend of decreasing "critical" pressure with increasing speed held. This trend could be due to changes in the axial thrust balance. Figure 5-8 shows the net downward axial force (without the thrust bearings) as decreasing with speed. With the spiral groove bearing at the aft side, the crashes could be due to an insufficient load on the front side when the forward thrust bearing is switched off. However, the crashes could also be due to an insufficient stiffness from the spiral grooves when the forward thrust bearing is switched off.

Due to fabrication difficulties (as mentioned in Section 5.1) wherein devices with spiral grooves on both forward and aft sides were not completed, we note that we were unable to test the functioning of hydrodynamic thrust bearings on *both* the forward and aft sides. Testing of hydrodynamic operation on both thrust bearings will allow us to understand its implications for the MicroEngine program. The concern of insufficient load capacity at low speeds can be addressed by employing dry friction to spin up the rotor quickly through the low speeds. Other possibilities to counter the low load capacity include designing of hybrid

thrust bearings, employing a temporarily supplied external pressurization like the MOP on both sides, or using leakages from essential pressures to provide the load capacity (as in our aft thrust bearing situation) for the rotor.

5.2.4 Operation with a hybrid hydrodynamic thrust bearing

Having tested a purely hydrodynamic thrust bearing device, we proceed to test the effects of a hydrostatic-to-hydrodynamic transition. A test scheme similar to a purely hydrodynamic thrust bearing mentioned above is used. In Figure 5-10, we plot the rotational speeds against time for a series of aft thrust hydrostatic bearing "shutdown" experiments. The shutdown is performed by closing off the pressure regulator, effectively venting the hydrostatic thrust bearing to ambient. In Run 1, we attempted a shutdown at a relatively low speed of 22,000rpm to gauge its effects. The device, as expected, immediately stopped. In Run 2, we performed the same procedure with a shutdown at 80,000rpm. While the rotor did indeed stop, we noticed that the decrease in speed to a final stop was not immediate—a slow decrease in speed for about 18 seconds was apparent before a sudden drop in speed. The increase in drag is due to the smaller thrust bearing gap; the slow time response is likely to be due to the slow decrease in pressures in the hydrostatic aft thrust bearing. In Run 3, at 119,000rpm, a much longer decrease in speed was observed—the rotational speed decreased slowly for about 247 seconds (with the thrust bearing already shutdown) before dropping drastically, whereupon we immediately increased up the aft thrust bearing pressure. We then proceeded to Run 4 wherein we shutdown the aft thrust bearing at 169,500rpm. This time there was a slight decrease in rotational speed, but it maintained rotation at 168,300rpm.

Figure 5-11 plots the corresponding aft thrust bearing pressures during the series of experiments. These shutdown experiments was later repeated and extended up to 400,000rpm. This device finally crashed at 450,000rpm during a shut-down procedure. The reason for the final crash is suspected to be due to the large increase in net axial force downwards as illustrated earlier in Figure 5-8.

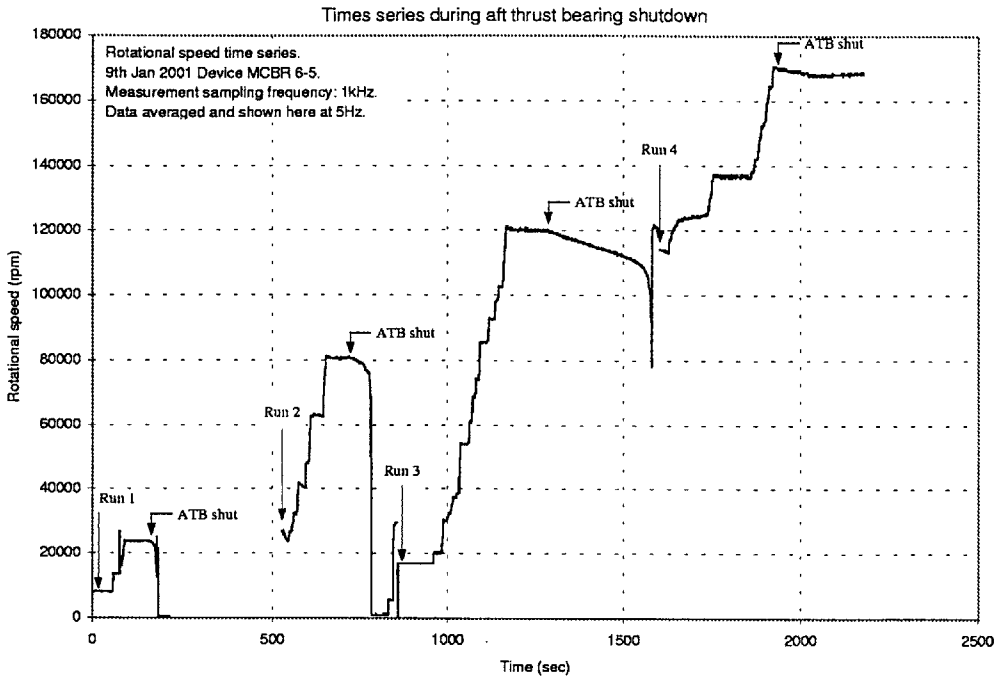

Figure 5-10: Time-series depicting a series of aft thrust bearing shutdown experiments where the eventually successful shutdown was achieved at 169,000rpm. Of interest is also the time delay in the speed decrease, suggesting increasing drag at higher speeds and larger eccentricities.

The characteristics of the drag could be used to determine the effects of the spiral grooves. If the position of the rotor could be determined accurately, we can compare the experimentally-obtained drag against the theoretical viscous drag in the hydrostatic thrust bearing and the modeled additional drag from the spiral grooves. Characterization of the experimental drag versus axial position relationship could also point to the relative effects of hydrodynamic spiral grooves.

5.3 Further remarks

Characterization of our hydrodynamic stiffness is only reported as a function of speed. However, hydrodynamic stiffness performances at various eccentricities would be interesting and helpful in mapping out the operating space. An expectation of increasing stiffness with

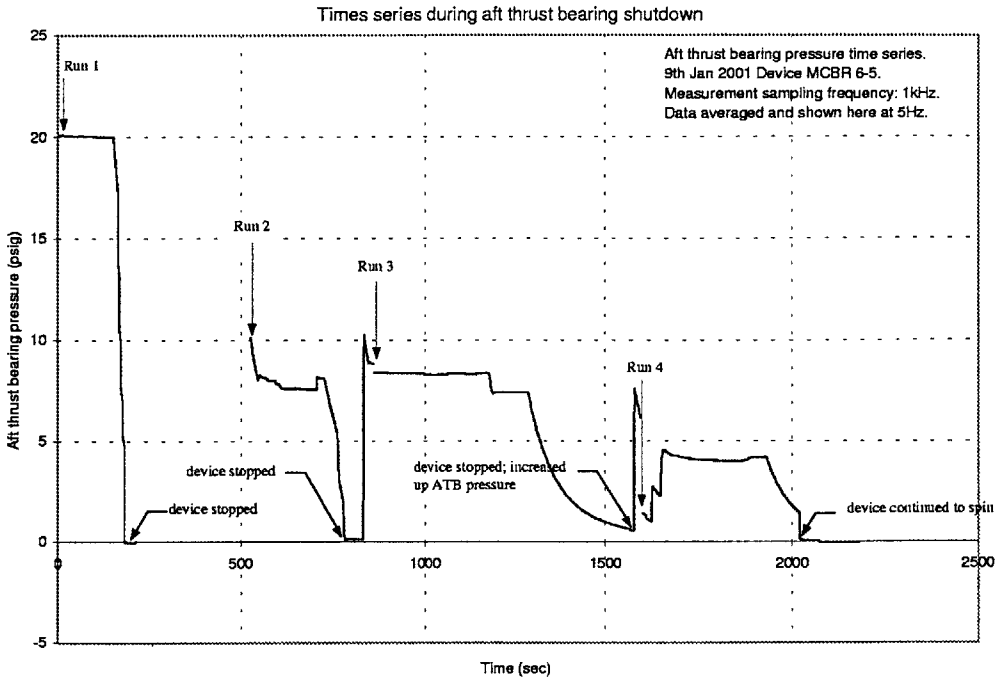

Figure 5-11: Time-series depicting a series of aft thrust bearing shutdown experiments where the eventually successful shutdown was achieved at 169,000rpm. Of interest is also the time delay in the speed decrease, suggesting increasing drag at higher speeds and larger eccentricities.

eccentricity could be explored. Current axial position measurement of the rotor is only estimated from the hydrostatic thrust bearing model, wherein we match the flowrates to predict the eccentricity. While the procedure to determine the eccentricity is fairly accurate (to an estimated 0.1 eccentricity[17]), we were not able to do so for the device tested. This is because, for this specific device, we did not see clear transitions between the maximum and minimum flowrates, like such in Figure 3-8 for our previous devices, when varying the pressure on either side during device rotation. In addition to eccentricity effects, measurements of the internal spiral groove pressures would also be interesting as a comparison with the theoretical model and existing literature [65].

There is also the possibility of placing the spiral grooves at a larger diameter[18] if a new

[17]Matching the flowrates to the hydrostatic thrust bearing model, we estimate this uncertainty from our calibrated model.

[18]Section 4.2, Equation 4.12, highlights the quartic increase in load capacity with spiral groove radius.

design on the thrust bearings is permitted. Currently, we were limited to minimal changes to the current device; however, if the spiral grooves were shifted out to a larger diamter, this allows much of the aft (or forward) side to reach a higher pressure[19] to produce the larger load capacity and stiffness. The additional concern would be the increased drag on the rotor.

Future incorporation of the spiral grooves into other devices could easily be possible, once an understanding of the axial forces in the specific device is achieved. With hydrodynamic thrust bearings, independent control of the stiffness during device operation is not possible except by varying speed, and external control of axial position is lost if only hydrodynamic thrust bearings are implemented on both forward and aft sides. However, the spiral grooves would eliminate the need for external pressurization, providing a possible self-contained bearing for the MicroEngine. The considerations of low stiffness and load capacity at low speeds can be addressed by primarily increasing the spiral groove diameter if space is not a limiting concern.

This suggestion is also pointed out by Professor Epstein.

[19]This is especially so with a larger spiral groove length.

Chapter 6

Conclusions

Day after day he appeared before us incomparably faithful to the illusions of the stage, and at sunset the night descended upon him quickly, like a falling curtain. The seamed hills became black shadows towering high upon a clear sky; above them the glittering confusion of stars resembled a mad turmoil stilled by a gesture; sounds ceased, men slept, forms vanished–and the reality of the universe alone remained—a marvellous thing of darkness and glimmers.
–J. Conrad, Heart of Darkness (1990 ed.)

This chapter summarizes the design, fabrication and experimental testing of the hydrostatic journal bearing and the hydrodynamic thrust bearing development process, along with analysis and recommendations for future work.

6.1 Hydrostatic Journal Bearing Concluding Remarks

Given the modeling and initial testing by the previous researchers, there existed a need to test the current devices and develop a better understanding of the MicroBearing test rig. We began this work with a sampling of theoretical work with the hydrostatic journal bearing, followed by fabrication improvements, experimental testing of the device in hydrostatic operation, and end with an analysis of the cause of failure with a proposed plan-of-action for future developments.

Hydrostatic Journal Bearing Theory A comparison of predicted hydrostatic stiffness by Piekos, Breuer and Orr suggested good coherence between the models. Variation in the model parameters, such as geometry, discharge coefficients, and eccentricity, was investigated to see the effects on the models. Design charts for optimal hydrostatic stiffness was presented, depicting our currently fabricated device at near the optimal, though slight improvements should be made. A look into the rotational effects on the axial-through flow stiffness brought out a $\frac{Re^2}{Ta}$ parameter that suggested negligible rotational effects. However, there exists a discrepancy between the experimental results and the theoretical predictions. A more complete hydrostatic journal bearing model is necessary to model the bearing characteristics.

Improved Fabrication of MicroBearing device With imbalance reduction suggested as the key to high-speed operation in a hydrostatic mode[1], we optimized the fabrication process to reduce the etch non-uniformity across the rotor of each device. Other fabrication work involves near-perfect straight DRIE on aspect ratios of 30 and above, and achievement of critical nozzle sizes in parallel with larger features. Future work includes a better understanding of the bonding process—an especially important step with the final device wafers but often with low yield—and improving the imbalance through further etch non-uniformity and misalignment reduction.

Experimental Testing Extensive experimental data was collected in the testing of the MicroBearing device. This includes pre-testing flow results and repeated operation of the MicroBearing devices in the vicinity of 300 m/s in tip speeds. Hydrostatic whirl natural frequency data is obtained and analyzed in this work—suggesting operation at a whirl ratio below 2 at high speeds[2]—to produce a characterization of the MicroBearing device. In addition, the failure of the thrust bearings in a specific device, due to the larger microfabricated

[1] In a hydrodynamic mode of operation, we also desire a reduction in imbalance. This is because we operate at high eccentricities in the hydrodynamic mode and, thus, an inversion with significant imbalance will lead to a crash.

[2] Whirl ratios several times larger than 2 are observed at low speeds

nozzles, is depicted. Future work could include a scheme to reduce the imbalance by static balancing [3], exploring the thermal effects, and further understanding of the dynamic orbits in the MicroBearing device.

Analysis of Hydrostatic Journal Bearing Operating Results Analysis of the hydrostatic whirl natural frequencies suggest a much larger whirl natural frequency than predicted. In addition, the effects of rotational speed and hysteresis are observed on the stiffness in the hydrostatic journal bearing. An exploration into the sideload and flowrates of the journal bearing suggests the devices moving into an off-centered position, possibly exciting hydrodynamic instabilities before a final crash. Development of an eccentricity sensor would be helpful in understanding the position and orbits of the rotor during operation, providing a confirmation of the suggested natural frequencies. Investigations into other hydrostatic journal bearing designs are also desirable to improve the stiffness of the hydrostatic journal bearing.

6.2 Hydrodynamic Thrust Bearing Remarks

Apart from the theoretical and experimental work on a hydrostatic journal bearing operation, it is desirable to implement a self-sustained MicroBearing device. As the hydrostatic thrust bearing pressurizations are currently significantly larger than the main turbine pressurization, development of a hydrodynamic squeeze-film thrust bearing was thus pursued. This consists of designing the spiral grooves with considerations of stability, inclusion of the features into the MicroBearing device and actual fabrication implementation. Finally, we present initial experimental results on the hydrodynamic thrust bearings.

Design considerations of a spiral groove Given the current hydrostatic journal bearing operational schedules, we designed the hydrodynamic thrust bearings to provide enough

[3] An "in-situ static balancing scheme" is employed by Orr [54] for the macro Bearing device.

stiffness and load capacity for "lift-off" during low speeds. This involved an optimization of the hydrodynamic spiral groove design geometry, inclusions of a hybrid hydrodynamic-hydrostatic thrust bearing mode, and investigations into the hydrodynamic stability during operation. Throughout the design process, the general intent is to incorporate the spiral grooves with minimal changes to the current MicroBearing device.

Fabrication and Testing of a hybrid thrust bearing The current fabrication process flow is modified to include several configurations of the new thrust bearings. Actual fabrication of the spiral grooves was successfully demonstrated. Final thermal fusion bonding of the Si wafers saw several difficulties and was finally successful only on the third attempt. Initial testing demonstrated the spiral grooves working in tandem with the hydrostatic thrust bearings. Effects of the spiral groove stiffness are, however, difficult to estimate without an adequate comparison with a control experiment. A purely hydrodynamic aft thrust bearing is then shown to work within the constrains of the current device, eliminating the need for external aft thrust bearing pressurization. Finally, a series of experiments with a hybrid thrust bearing is performed, in which we observe a large increase in drag due to changes in rotor axial position, and eventual shutdown of the aft thrust bearing is successfully demonstrated. Future work includes a calibration of the stiffness at different eccentricities and measurements of the internal pressures above the spiral grooves to better understand the characteristics of the spiral grooves. In addition, development of hybrid bearings on both the forward and aft sides would allow us to definitively test the effects of the spiral grooves.

Appendix A

Source code

A.1 Axial Thrust Balance for Spiral Grooves

```
%computeAxialForces.m

function [Fmain, Flowhigh, Fmop, Fmop2, Fmass, Ftotal]
= computeAxialForces(speed, P_ambient, rotor_mass)

%Created by Chee Wei Wong
%First edition: 12/21/99
%Second edition: Now changed solely for comparison purposes.
%Third edition: 3/12/2000. ironed out bugs.
%Four edition: 3/14/2000. Pointed out by Stu that force by Pinlet
%should be (Pinterrow+Pambient)/2

%This module computes the axial force on the rotor. There are nine
%recognizable sources of axial forces on the rotor:
%(1) due to P_inlet at the blades: Fmain
%(2) due to Plow/Phigh at the first restrictor: Fhighlow
%(3) due to Pmop (vertical): Fmop
%(4) due to Pmop (horizontal): Fmop2
%(5) due to Pambient on (a) the top side of the rotor,
% (b) right above the exhaust
%(6) due to momentum change on Pinlet upwards
%(7) due to shear forces on the Plow/Phigh moving upwards
%(8) due to the Plow/Phigh hitting the tiny part of the rotor vertically
%(9) due to the momentum change of Pmop moving downwards.
%
```

```
%Assumption:
%1.Forces of (6)-(9) are treated as negligible compared to forces (1)-(5).
%2.Assume pressure distribution is linear. Therefore, forces could be
%  calculated  as (Pressure_average * area).
%3.We use empirical experimental relationships to determine the desired
%  pressures for a certain speed. While experimental results here have
%  shown that these pressures are indeed what we want
%(for actual operation) we have not reached the design speed
%of 2.4E6. Therefore, we may have to refine the empirical
%relationships later in the time.
%
%Comments:
%1. This computation only serves as a approximation of the order of
%   magnitude of the axial forces.
%2. All units in SI; measurements are given as radius.
%3. Notation is upwards as positive forces.
%4. Reconverted as check with Stu's spreadsheet.
%
```

```
for i = 1:size(speed,2)

spd = speed(i)/100000; %so that the correlations will have a better fit.
%computing the downward force by the Pinlet--------------------------
%area of pressure can be treated as a RING as pressure acts equally down
minBladeRadialPosition = 1.276E-3;
maxBladeRadialPosition = 2.100E-3;
forwardThrustBearingRadius = 0.7E-3;
areaTopBlades = pi*(maxBladeRadialPosition^2
      - minBladeRadialPosition^2);
%assuming P_ambient at end of blades.
areaTopNoBlades = pi*(minBladeRadialPosition^2
- forwardThrustBearingRadius^2);
%here's the empirical correlation for speed to Pinterrow from MCBR 2-5 run.
Pinterrow_psi =0.0007*spd^4-0.0085*spd^3+0.0755*spd^2+0.3935*spd;
Pinterrow = (Pinterrow_psi+14.7)* 6894.8; %convert gaged psi to Pa
Fmain_blades = ((Pinterrow+P_ambient)/2) * areaTopBlades;
Fmain_topNoBlades = P_ambient * areaTopNoBlades;
Fmain(i) = - (Fmain_blades + Fmain_topNoBlades);
%downwards as negative by convention


%computing the upward force by low/high plenum leak---------------
tipSealOuterDiameter = 4.14E-3;
tipSealInnerDiameter = 3.96E-3;
areaTipSeal = pi*(tipSealOuterDiameter^2 - tipSealInnerDiameter^2)/4;
```

```
%here's the empirical correlation for speed to Plow/Phigh from MCBR
%MCBR 2-5 run. noticed that we're running hydrostatically so
%Plow/Phigh follow the same schedules.
Plowhigh_psi =-0.00009*spd^4 + 0.016*spd^3 - 0.1893*spd^2 + 1.8346*spd;
Plowhigh = (Plowhigh_psi+14.7)* 6894.8; %convert gaged psi to Pa

%here's the empirical correlation for speed to Pmop from MCBR2-5 run.
Pmop_psi = 0.0003*spd^4 + 0.004*spd^3 - 0.0816*spd^2 + 1.2838*spd;
Pmop = (Pmop_psi+14.7) * 6894.8; %convert gaged psi to Pa
Pave_seal = (Pmop + Plowhigh)/2;
Flowhigh(i) = Pave_seal * areaTipSeal;

%computing the upward force by Pmop direct "hit"----------------------
mopOuterDiameter = tipSealInnerDiameter; %it's the same wall!
mopInnerDiameter = 3.88E-3;
areaMOP = pi*(mopOuterDiameter^2 - mopInnerDiameter^2)/4;
Fmop(i) = Pmop * areaMOP;

%computing the upward force by Pmop horizontal flow with linear pressure
%distribution. Assumption that exhaust is all the way Pambient.
%can assume ambient at exhaust as seen from experiemental runs-------
exhaustPlenumOuterDiameter = 1.92E-3;
areaTravelToExhaust = pi*(mopInnerDiameter^2
- exhaustPlenumOuterDiameter^2)/4;
Pave_mop = (Pmop + P_ambient)/2;
Fmop2(i) = Pave_mop * areaTravelToExhaust;

%computing the areas on the lower side that is not included above;
```

```
exhaustPlenumInnerDiameter = 1.804E-3;
areaDirectExhaust=pi*(exhaustPlenumOuterDiameter^2
-exhaustPlenumInnerDiameter^2)/4;
F_exhaust(i)=P_ambient*areaDirectExhaust;
%for the area directly above the exhaust
areaBottomOutsideTipSeal=pi*((2*maxBladeRadialPosition)^2
-tipSealOuterDiameter^2)/4;
F_lowhigh_direct(i) = Plowhigh * areaBottomOutsideTipSeal;


%total sum of forces at the input speed, including mass
Fmass = - rotor_mass * 9.81; %downwards as negative by convention
Ftotal(i) = Flowhigh(i) +Fmop(i) +Fmop2(i) +Fmain(i) + Fmass
   +F_lowhigh_direct(i) +F_exhaust(i) ; %convention is upwards positive.

%compute the moments to check if it is indeed negligible.
%here we compute the sum of moments from the air pressures
%if the rotor is lateral displaced by 10um. this sum of
% moments can be used to check the wobble.
%For wobble effects, look also at ''Spaceflight dynamics''
%by William E. Wiesel, 1989.

%In addition, rotor flexure has also been considered earlier
%by other students/staff.

sumMomentsAirPressures = Flowhigh(i)*((tipSealOuterDiameter...
   +tipSealInnerDiameter)/2 +10E-6)...
   +Fmop(i)*((mopOuterDiameter+mopInnerDiameter)/2 +10E-6)...
```

```
+Fmop2(i)*((mopInnerDiameter+exhaustPlenumOuterDiameter)/2 +10E-6)...
-Fmain(i)*((minBladeRadialPosition+maxBladeRadialPosition)/2 +10E-6);

end
```

A.2 Sample simulation for hydrodynamic spiral groove thrust bearings

A.2.1 Hierarchy of routines, programmed in Matlab scripts

Shown in Figure A-1, the hierarchy of the scripts improves modularity of this simulation. Each arrow, of course, represents information passing into the subroutine and information passing back into the parent subroutine.

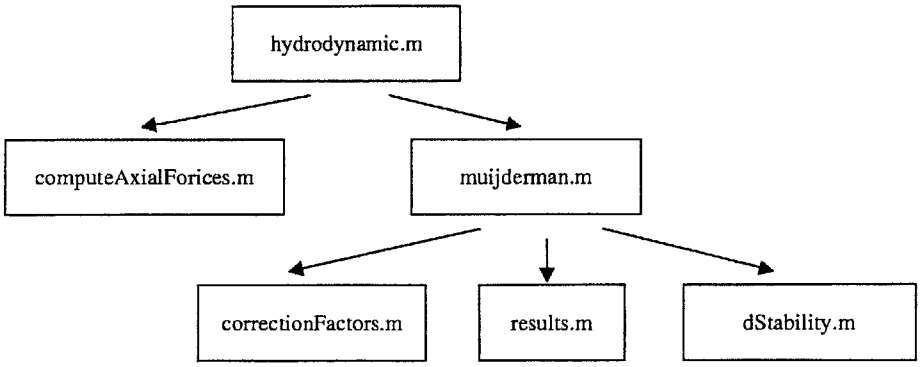

Figure A-1: Hierarchy of routines in hydrodynamic spiral grooves simulation

A.2.2 hydrodynamic.m

```
%This is the main file that calls "muijderman.m" which computes all the
%results for certain design parameters. Moreover, it calls
%"computeAxialForces.m" to compute the axial forces on the rotor due to
%the pressures from the low and high pressure plenums, M.O.P, etc.
%
%Created by Chee Wei Wong
%First version: 12/21/99
%Second version: 03/04/00
%Third version: 03/06/00. Design parameters optimized.
%4th: 04/21/00. Reworked with new axial load comparison computation.
%5th: 05/18/00. Included Constantinescu and Galetuse's stability.
%6th: 07/03/00. Included storage of unstable speed from stablity.

%Assumption:
%1. that moment created (when rotor is lateral displaced) is negligible
%
%Comments and Notes:
%1. design parameters are stored in "muijderman.m" file.



%declaration of operation ("fixed") variables
clear all; close all;
temp = 300;
P_ambient = 101400;
```

```
rotor_mass = 11.3E-6;
viscosity =0.000001458*temp^1.5/(temp+110.4);  %Sutherlands law

%define solution space & number of inerations (different speeds) here
numberOfIterations = 45;
speed = linspace(1000,1.2E6,numberOfIterations);
unstableSpeed = -1; %as a flag and counter.

%doing the computation
for i=1:numberOfIterations
   [forceAtEachSpeed, eccentricity, stiffnessAtEachSpeed,dragAtEachSpeed,
compress_crit1_fwd, compress_crit2_fwd, compress_crit1_aft,
compress_crit2_aft, centerPressureRatio_fwd, centerPressureRatio_aft,
unstableSpeed] = muijderman(speed(i), P_ambient, rotor_mass,...
viscosity,unstableSpeed);
   forceThrustBearingsMatrix(:,i) = forceAtEachSpeed';
   stiffnessMatrix(:,i) = stiffnessAtEachSpeed';
   dragMatrix(:,i) = dragAtEachSpeed';
end

%compute the axial forces on the rotor from the pressures
for l=1:numberOfIterations
   [Fmain, Flowhigh, Fmop, Fmop2, Fmass, Ftotal] = computeAxialForces
   (speed(l), P_ambient, rotor_mass);
   axialForces(:,l) = [Fmain; Flowhigh; Fmop; Fmop2; Fmass; Ftotal];
end

%extracting "lift-off speed" & checking if needs beyond 0.33 eccentricity
```

```
takenOff =0; moreThanEccen = 'False';
for j=1:numberOfIterations
  if axialForces(6,j) >0 %pressures pushing it upwards
      %therefore, check positive eccentricity
      if (abs(forceThrustBearingsMatrix(size...
         (forceThrustBearingsMatrix,1),j)) > axialForces(6,j))
         if takenOff==0
            liftOffSpeed = speed(j); takenOff =1;
         end
      else
         if takenOff==1
            moreThanEccen = 'True';
         end
      end
   end %endCase

   if axialForces(6,j)<0 %pressures pushing it downwards
      %therefore, check negative eccentricity
      if (abs(forceThrustBearingsMatrix(1,j)) > -axialForces(6,j))
         if takenOff==0
            liftOffSpeed = speed(j); takenOff =1;
         end
      else
         if takenOff==1
            moreThanEccen = 'True';
         end
      end
   end   %endCase
```

```
end %endFor

%output results on screen
compress_crit1_fwd,compress_crit2_fwd, compress_crit1_aft,...
 compress_crit2_aft
if (unstableSpeed~=-1)
   fprintf('Dynamic stability boundary exceeded. Unstable.\n')
   fprintf('Speed at which dynamic stability is exceeded is:')
   unstableSpeed
end
liftOffSpeed
moreThanEccen

%plotting the results
figure; %for simply the hydrodynamic thrust bearings
subplot(2,1,1)
for k =1:size(forceThrustBearingsMatrix,2)
   plot(eccentricity, forceThrustBearingsMatrix(:,k)); hold on;
end
grid on; title('Spiral Groove thrust bearings')
xlabel('Eccentricity'); ylabel('Load (N)');

subplot(2,1,2)
for j=1:round(size(forceThrustBearingsMatrix,1)/2)
   plot(speed, forceThrustBearingsMatrix(j,:)); hold on;
end
grid on; title('Spiral Groove thrust bearings')
xlabel('Rotational Speed (rpm)'); ylabel('Load (N)');
```

```
figure; %for determining the "lift-off" speed
subplot(2,1,1)
plot(speed, axialForces(1,:),'*-',speed,axialForces(2,:),'*-',speed,...
      axialForces(4,:),'*-',speed,axialForces(6,:),'o-');
hold on; grid on; title('Axial loads due to air pressures')
ylabel('Axial loads (N)'); %xlabel('Rotational Speed (rpm)');
legend('F-inlet', 'F-lowhigh', 'F-mop2', 'Ftotal');

subplot(2,1,2)
for j=1:2:size(forceThrustBearingsMatrix,1)
   plot(speed, forceThrustBearingsMatrix(j,:)); hold on;
end
plot(speed,-axialForces(6,:),'o');
grid on; title('Determination of "lift-off" transition')
ylabel('Load (N)'); xlabel('Rotational Speed (rpm)');

figure; %for getting the stiffness, Frequency ratio, and drag charts
stiffnessPlot = stiffnessMatrix(round(size(stiffnessMatrix,1)/2),:);
FrequencyDimensional = (sqrt(stiffnessPlot./rotor_mass))/(2*3.142);
%simple linear spring-mass assumption.
FrequencyRatioOverRotationalSpeed = FrequencyDimensional./(speed/60);
subplot(2,1,1)
plot(speed, stiffnessMatrix)
grid on; title('Stiffness and Drag considerations with speed');
ylabel('Stiffness (N/m)'); %xlabel('Rotational Speed (rpm)');

%subplot(3,1,2)
```

```
%plot(speed(1,2:numberOfIterations), FrequencyRatioOverRotationalSpeed...
    (1,2:numberOfIterations),'o-')
%eliminating first solution from the plot 'cos it's not useful.
%grid on; %title('Natural Frequency with speed');
%ylabel('Frequency/Speed'); %xlabel('Rotational Speed (rpm)');

subplot(2,1,2)%
%plot(speed,dragMatrix(round(size(dragMatrix,1)/2),:));
%single eccen representation
plot(speed, dragMatrix) %different eccens
grid on; %title('Drag with speed');
ylabel('Drag (N)'); %xlabel('Rotational Speed (rpm)');
xlabel('Rotational Speed (rpm)')
%end of main module
```

A.2.3 muijderman.m

```
function [force, eccentricity,stiffness,drag, compress_crit1_fwd,
compress_crit2_fwd, compress_crit1_aft, compress_crit2_aft,...
        center_pressure_ratio_fwd, center_pressure_ratio_aft,...
   unstableSpeed] = muijderman(inputSpeed,P_ambient,...
rotor_mass, viscosity, unstableSpeed)

%This module is to design the hydrodynamic thrust bearings as indicated
%by E.A. Muijderman. This spiral groove hydrodynamic thrust bearings
%has also been covered in Hamrock in "Fundamentals of Fluid Film
```

```
%Lubrication (1994)".
%Initial stability calculations from Pan and Malanoski.
%Later included stability calculations from Constantinescu and Galetuse.

%This model is compiled from a previous model by Professor Kenny Breuer,
%with the excel workbook "micro bearing rig HD analysis.xls" in 1998.
%
%Created by Chee Wei Wong
%First version: 12/21/99. Initial version
%Second version: 03/04/00. Searching design space.
%3rd: 03/06/00. Design parameters optimized, included Pan and Malanoski.
%Fourth version: 05/15/00. Finalized design.
%5th: 05/19/00. Included Constantinescu and Galetuse's stability.
%6th version: 07/03/00. Corrected expression of compression number of
%   Malanoski and Pan.
%
%Comments and notes:
%1. All units in SI.
%2. Variable names are named after Muijderman's notation.
%3. "(variableName)_fwd" denotes forward thrust bearing;
%   "(variableNamne)_aft" denotes aft thrust bearing.
%4. Notation is upwards for positive eccentricity, displacement.
%5. Notation is upwards for positive force.
%6. "compressionNumber_fwd" and "compressionNumber_aft" numbers
%are found in Pan and Malanoski, and Constantinescu and Galetuse.
%

fprintf('\nNew computation set at muijderman.m')
```

```
%Declaration of operation ("design") variables
speed_rpm = inputSpeed;
speed_hz = speed_rpm/60;
speed_radsec = speed_hz * 2*pi;

%Design parameters for FORWARD THRUST BEARING
k_fwd = 50;          %number of grooves
h2_fwd = 1.0E-6;      %bearing gap
h0_fwd = 2.4E-6;      %groove depth
r2_fwd = 700E-6;    %outer radius of spiral
r1_fwd = 560E-6;    %inner raduis of spiral
alpha_fwd = 16;     %spiral angle
gamma_fwd = 1.2;      %ratio of ridge width/groove width
%compressionNumber_fwd =3*viscosity*speed_radsec*(r2_fwd^2-r1_fwd^2)/...
(P_ambient*h2_fwd^2)
%above formula wrong seems r1_fwd^2 should NOT be included.
%See Malanoski and Pan's notes on R_i.
compressionNumber_fwd =3*viscosity*speed_radsec*(r2_fwd^2)/...
(P_ambient*h2_fwd^2)
stabilityParameter_fwd = (r2_fwd-r1_fwd)/r2_fwd

%Design parameters for AFT THRUST BEARING
k_aft = 50;
h2_aft = 1.0E-6;
h0_aft = 2.4E-6;
r2_aft = 700E-6;
r1_aft = 560E-6;
```

```
alpha_aft = 16;
gamma_aft = 1.2;
%compressionNumber_aft =3*viscosity*speed_radsec*(r2_aft^2-r1_aft^2)/...
(P_ambient*h2_aft^2)
compressionNumber_aft =3*viscosity*speed_radsec*(r2_aft^2)/...
(P_ambient*h2_aft^2)
stabilityParameter_aft = (r2_aft-r1_aft)/r2_aft

%Now the loops for different displacements and different speeds
for i=1:21
   disp(i) = -0.5E-6 + (i-1)*0.05E-6;
   eccentricity(i) = 2*disp(i)/(h2_fwd+h2_aft);

   %Forward Thrust Bearing
   operating_gap_fwd = h2_fwd-disp(i);
   H_fwd = operating_gap_fwd/(operating_gap_fwd+h0_fwd);
   delta_fwd = operating_gap_fwd / h0_fwd;
   lambda_fwd =r1_fwd / r2_fwd;
   [C1,C2,g1,g2] = correctionFactors(alpha_fwd, H_fwd, gamma_fwd,...
     lambda_fwd, k_fwd);
   [center_pressure_ratio_fwd,load_capacity_fwd,stiffness_metric_fwd,...
    torque_fwd, power_fwd] = results(P_ambient,viscosity,...
    speed_radsec,r2_fwd,lambda_fwd,operating_gap_fwd,g1,g2,C1,C2);
   %Nondimensional Forward Thrust Bearing Results
   ratioLoadOverWeight_fwd = load_capacity_fwd/(rotor_mass *9.81);
   ratioStiffnessGapOverWeight_fwd = stiffness_metric_fwd*...
operating_gap_fwd/(rotor_mass*9.81);
```

```
   %Aft Thrust Bearing
   operating_gap_aft = h2_aft+disp(i);
   H_aft = operating_gap_aft/(operating_gap_aft+h0_aft);
   delta_aft = operating_gap_aft / h0_aft;
   lambda_aft =r1_aft / r2_aft;
   [C1,C2,g1,g2] = correctionFactors(alpha_aft, H_aft, gamma_aft,...
     lambda_aft, k_aft);
   [center_pressure_ratio_aft,load_capacity_aft,stiffness_metric_aft,...
   torque_aft, power_aft] = results(P_ambient,viscosity,...
   speed_radsec,r2_aft,lambda_aft, operating_gap_aft,g1,g2,C1,C2);
   %Nondimensional Aft Thrust Bearing Results
   ratioLoadOverWeight_aft = load_capacity_aft/(rotor_mass *9.81);
   ratioStiffnessGapOverWeight_aft = stiffness_metric_aft*...
operating_gap_aft/(rotor_mass*9.81);
   %Overall results
   force(i) = load_capacity_aft - load_capacity_fwd;
   nonDimensionalForceOverWeight = force(i)/(rotor_mass*9.81);
   drag(i) = power_fwd + power_aft;

end

%calculating the differential stiffness values
if i<3
   fprintf('no differential stiffness can be calculated\n')
   fprintf('because there are too few displacement iterations.\n')
else
   %stiffness = abs(diff(force,2)./diff(disp,2))
```

```
   for j=2:i-1
     stiffness(j-1) = abs((force(j+1)-force(j-1)) / (disp(j+1)-disp(j-1)));
     %this stiffness is a differential stiffness;
     %note that we have (n-2) terms
     naturalFreqOverRotationalSpeed(j-1) = (sqrt(stiffness(j-1)/...
rotor_mass)/(2*pi))/speed_hz;
  end
end

%here: check if number of grooves is greater than the minimum number
%for Muijderman's end effect correction to be correct. If not, then
%his end effect correlation is slightly-off and should not be used.
%From Equation 4.42, Muijderman, page 57.
testNumberGrooves_fwd = 2.5*((sin(alpha_fwd))^2 *(2/1+gamma_fwd)...
 +.5*sin(2*alpha_fwd))*(pi/-log(lambda_fwd));
if k_fwd > testNumberGrooves_fwd
   fprintf('Forward number of grooves are sufficient.\n');
   fprintf('Muijderman end-effect-correction correctly used.\n');
else
   fprintf('Forward number of grooves insufficient!');
end
testNumberGrooves_aft = 2.5*((sin(alpha_aft))^2 *(2/1+gamma_aft)...
 +.5*sin(2*alpha_aft))*(pi/-log(lambda_aft));
if k_aft > testNumberGrooves_aft
   fprintf('Aft number of grooves are sufficient.\n');
   fprintf('Muijderman end-effect-correction correctly used.\n');
else
   fprintf('Aft number of grooves insufficient!');
```

```
end


%Dynamic stability calcution
%ideally, this should be outside this script since it'sran many times.
%but i wanted to keep the design parameters in this chart, instead of a
%separately loaded file.
%from Constantinescu and Galetuse, 1987 and 1990.


[compress_crit1_fwd, compress_crit2_fwd] = dStability(h2_fwd,h0_fwd,...
alpha_fwd,gamma_fwd,r2_fwd,r1_fwd, k_fwd);
[compress_crit1_aft, compress_crit2_aft] = dStability(h2_aft,h0_aft,...
alpha_aft,gamma_aft,r2_aft,r1_aft, k_aft);

if (unstableSpeed == -1)
   %forward thrust bearing
   %note that the compression number (for C.&G.) is identical to
   % that from Pan and Malanoski.
   if (compressionNumber_fwd>compress_crit1_fwd) | ...
(compressionNumber_fwd>compress_crit2_fwd)
      fprintf('Dynamic stability boundary exceeded in Forward Thrust...
 Bearing. Unstable.\n')
      %fprintf('The speed at which dynamic stability is exceeded is:')
      unstableSpeed = speed_rpm
      compressionNumber_fwd
   end
```

```
   %aft thrust bearing
   %note that the compression number (for C.&G.) is identical to
   %that from Pan and Malanoski.
   if (compressionNumber_aft>compress_crit1_aft) |...
 (compressionNumber_aft>compress_crit2_aft)
      fprintf('Dynamic stability boundary exceeded in Aft Thrust...
 Bearing. Unstable.\n')
      %fprintf('The speed at which dynamic stability is exceeded is:')
      unstableSpeed = speed_rpm
      compressionNumber_aft
   end
end
```

A.2.4 correctionFactors.m

```
function [C1,C2,g1,g2] = correctionFactors(alpha,H,gamma,lambda,k)

%This method returns the four correction factors suggested by
%Muijderman. These correction factors are also tabled by Hamrock (1994)
%in Figure 16.7 (page 348).
%
%This method supports the main module "hydrodyamic.m"
%Created by Chee Wei Wong
%12/21/99

%the below variables are for testing the model
```

```
%alpha = 17;
%H = .43;
%gamma = 1;
%lambda = .80;
%k = 50;

C1 =(exp(-(2/(1+gamma))*(1+gamma*H^3)/(1+H^3)*pi/k*(1-alpha/90)*...
   tan(pi*alpha/180)) - lambda^2*exp((2/(1+gamma))*(1+gamma*H^3)/...
   (1+H^3)*pi/k*(1-alpha/90)*tan(pi*alpha/180)))/(1-lambda^2);

C2 =(exp(-2*(2/(1+gamma))*(1+gamma*H^3)/(1+H^3)*pi/k*(1-alpha/90)*...
   tan(pi*alpha/180)) - lambda^4*exp(2*(2/(1+gamma))*(1+gamma*H^3)/...
   (1+H^3)*pi/k*(1-alpha/90)*tan(pi*alpha/180)))/(1-lambda^4);

g1 =(gamma*H^2*(1/tan(alpha*pi/180))*(1-H)*(1-H^3))/(((1+gamma*H^3)*...
    (gamma+H^3))+(H^3*(1/(tan(alpha*pi/180))^2)*(1+gamma)^2));

g2 =((gamma+H)+(3*gamma*H*(1-H)^2*(1+gamma*H^3))/((1+gamma*H^3)*...
    (gamma+H^3)+H^3*(1/(tan(alpha*pi/180))^2)*(1+gamma)^2))/(1+gamma);
```

A.2.5 results.m

```
function [center_pressure_ratio,load_capacity,stiffness_metric,...
torque,power] = results(P_ambient,viscosity,speed_radsec,...
r2,lambda,operating_gap,g1,g2,C1,C2)
```

```
%This method computes the dimensional values form Muijderman.
%The values are found from "Chapter 5: Formulae for various types
%of spiral groove thrust bearings" at "Spiral Groove Bearings" by
%Muijderman, 1966. Reference is at page 63-65.

%This method supports the main module "hydrodyamic.m"
%Created by Chee Wei Wong
%12/21/99



%Here's the formulaes

%pressure at inner radius r1 (with outer radius fixed at ambient)
center_pressure_ratio = (P_ambient+(3*viscosity*speed_radsec*r2^2*...
(1-lambda^2)/operating_gap^2)*g1*C1)/P_ambient;

%load capacity of spiral grooves
load_capacity = (3*pi*viscosity*speed_radsec*r2^4/(2*operating_gap^2...
))*(1-lambda^4)*g1*C2;

%stiffess of spiral grooves
stiffness_metric = 2*load_capacity/operating_gap;
%not much reason for the factor of 2.

%resulting torque or power/drag on rotor.
torque = 1E6*pi*viscosity*speed_radsec*r2^4*(1-lambda^4)*g2/...
(2*operating_gap); %torque in [Nmx10^6]
```

```
power = torque*speed_radsec/1E6;
```

A.2.6 dStability.m

```
function [compress_crit1, compress_crit2] = dStability(h2,h0,alpha,...
    gamma,r2,r1,k)

%This simulation is from Constantinescu and Galetuse (C.&G)
%Journal Of Tribology Jan 1987 Vol.109/183 and
%Journal Of Tribology Oct 1990 Vol.112/734.
%
%First created by Chee Wei Wong, May 19th 2000.
%Comments:
%compress_crit1 is the compression number for a partially-grooves
%spiral groove bearing. compres_crit2 is the compression number for a
%spiral groove bearing with transverse flow. Our designed SPG provides
%more load and stiffness than these two models.

%And, since the compression_crit of (spiral groove bearing with
%transverse flow)is also larger than (partially-grooves spiral groove
%bearing) and the load& stiffness is better, we MIGHT expect our model
%to have a larger compression_crit than both, since our model has more
%load and stiffness than both these models.

%getting the rest of the geometries
h1 = h0 + h2; %groove depth + thrust bearing gap
```

```
h1b = h1/h2; %h1_bar in Constantinescu and Galetuse
h2b = h2/h2; %(equals to one,
     %under static conditions for calculation in C.&G)
b = 2*3.142*r2/k; %total groove and ridge width
b1 = b/(1+gamma); %groove width
b2 = b-b1; %ridge width
b1b = b1/b; %b1_bar in Constantinescu and Galetuse
beta = (180-alpha)*3.142/180;
%spiral angle in Constantinescu and Galetuse, in radians.
delta_b = h1b-h2b;
Rgb = r1/r2;
Rib = 0.6*r2/r2; %taking the hydrostatic nozzles at slightly inside
 %the inner of the spiral grooves. therefore, 60%

%testing these equations with C.&.G's plots.
%beta = 2.836; b1b=0.6;Rgb=0.475;

%computing the co-factors
fro = (h1b^3 + b1b*(1-b1b)*(h1b^3-1)^2 * sin(beta) * sin(beta)) /...
      ((1-b1b)*h1b^3 + b1b);
fso = (h1b^3-1)/ ((1-b1b)*h1b^3 + b1b);
fu = 2*b1b * (1-b1b) * delta_b * sin(beta);
fse = -3 * (delta_b * (1+delta_b)^2)/ ((1-b1b)*(1+delta_b)^3 +b1b)^2;
temp1 = (1+delta_b)^2*(b1b+(1-b1b)*(1+delta_b)^4);
temp2 = (1-b1b)*(1+delta_b)^8 - (2-b1b)*(1+delta_b)^6;
temp3 = 2*b1b*(1+delta_b)^5 + 2*(1-b1b)*(1+delta_b)^3 - (1+b1b)*...
(1+delta_b)^2 +b1b;
A = 3*(temp1 + b1b*(1-b1b)*sin(beta)*sin(beta)*(temp2 + temp3));
```

```
fre = A /( (1-b1b)*(1+delta_b)^3+b1b)^2;

%computing the A0, A1, A2, A3, A4 factors for partially-grooved
%inward pumping spiral groove bearing.
A0 = fro/(1-Rgb^4);
A1 = 1 + (b1b*delta_b*(1-Rgb^2)/(1+Rgb^2));
A2 = (fre/fro) - (fse/fso);
A3 = 1;
A4 = 1;
compress_crit1 = (4*A0) / (fu*fso*abs(cos(beta))*(A1*A2-A3*A4));

%computing the A0, A1, A2, A3, A4 factors for inward pumping
%spiral groove bearing with transverse flow.
A0 = ((0.3*Rib*fro/(Rgb-Rib)) + 1/(1-Rgb^2)) * (1-Rib^2);
A1 = 1-Rgb^2 + ((Rgb-Rib)*(7.2*Rgb+3.2*Rib)/6) + (2/3)*b1b*delta_b*...
     (Rgb-Rib)*(1.8*Rgb+0.8*Rib);
temp4 = fre + 10*(Rgb-Rib)/(Rib*(1-Rgb^2));
temp5 = fro + 3.33*(Rgb-Rib)/(Rib*(1-Rgb^2));
A2 = (temp4/temp5 - fse/fso)*Rib^2;
A3 = 1-Rgb^2 + (Rgb-Rib)*(7.2*Rgb+3.2*Rib)/6;
A4 = (0.3*Rib*fro + (Rgb-Rib)/(1-Rgb^2)) / (0.7*fro + Rgb*(Rgb-Rib)/...
     (1-Rgb));
compress_crit2 = (4*A0) / (fu*fso*abs(cos(beta))*(A1*A2-A3*A4));
```

Appendix B

MicroBearing Rig Fabrication and Experimentation

B.1 Modified Fabrication Process Flow

[Adapted from Fréchette's Version 1.3 and 1.4]

Fabrication Process Flow for Motor-Compressor Bearing Rig, ver 1.5

Differences from ver 1.3: Last updated 24/05/00

Updated rotor flow based on tethered-motor and bearing-rig: Chee Wei: Edited from Luc Frechette's and CC Lin's initial process flow

Oxide protection against STS back side pitting; Modified rotor flow

Photoresist back coat protection against AME5000 scratching ; More complete process information (Stator and STS recipes)

New FEP and AEP masks to prevent effect of pitting and side-wall etching

Differences from motor-compressor, ver1.4:

Adapted motor-compressor process flow ver 1.4 for bearing rig:

Shift shallow etches from rotor plate to AEP; Ready for journal-first approach, but using FEP-RP snap-off tabs

Differences from micro-bearing, ver1.5:

Adapted motor-compressor process flow of bearing rig for hydrodynamic thrust bearings:

Added 10 masks for hybrid hydrodynamic or solely hydrodynamic thrust bearings.

Moved hydrostatic nozzles of hybrid hydrodynamic bearing rig inwards to give more action for spiral groove bearings.

Common process steps

Thick Photo (in TRL)	
HMDS	std: 17min
Coater: adapt spin speed for desired thickness	Resist: AZ4260 Spin: 9s @ 1700, 60s @ [speed], 10s @ 7000rpm Manual static dispense, finish w/ swab edge wipe
Pre-bake	1hr @ 90C
Ksaligner2: adapt time according to thickness	power: 6.0
Develop: adapt time according to thickness	AZ440 MIF
Post-bake	1hr @ 110C (small oven)
Thin Photo (in TRL)	
HMDS	std: 17min
Coater: adapt spin speed for desired thickness	Resist: OCG825 Spin: 6s @ 500, 6s @ 750, 30s @ 2500rpm (for 1um) Automatic dynamic dispense, finish w/ swab edge wipe
Pre-bake	0.5hr @ 90C
Ksaligner2: adapt time according to thickness	power: 6.0, 45sec for 1um
Develop: adapt time according to thickness	OGC934, 2-2.5min for 1um
Post-bake	0.5hr @ 120C
Alignment marks	
Thin Photo (or ICL photo)	standard thin photo-resist (1um)
Etcher-1 (or AME, but must then add back coat)	1-2um deep
Asher	
Bond handle wafer	Attach quartz handle wafer prior to postbake
Coater	Resist: AZ4260 Spin: 9s @ 1700, 60s @ [speed], 10s @ 7000rpm 1-2cm rim, w/ swab edge wipe and open channels across rim
Contact device wafer to quartz handle wafer (use jig)	
Compress rim area (pressing with a swab on each side)	
Post-bake	same bake step as device resist
Back coat	Protect the backside of wafer with PR during handling
After develop, before post-bake: spin standard thin resist on backside of wafer, using the teflon chuck	
Oxide protective coating	
Piranha	ICL
Concept 1	0.1um thick novellus oxide, unless otherwise noted
Densification (tube B6 in ICL)	1100 C for 1hr

Figure B-1: Fabrication Process Flow for Motor-Compressor Bearing rig Version 1.5—Common Process Steps. [Adapted from Fréchette [31]]

Forward Foundation Plate (A):	
Wafer: Silicon <100>, n-type prime, thickness=450um, double-side polished	
Measure wafer bow and thickness	
Alignment marks (front side) - expose all the mask for writing	*Mask A0-Marks-1;* expose all the mask
Alignment marks (back side)	*Mask A0-Marks-1;* expose only the alignment marks
Oxide protective coating (front side)	0.1 um (standard)
Deep Si etch through wafer: 450um (back side)	Mask A1b-Foundation-1 (dark field)
Thick Photo - IR (hide align. marks) + Handle wafer	TRL thick resist: AZ4620 12um thick
STS	450um (through wafer), MIT69 (~3:35) + MIT48 for last 10min
Piranha	
Forward End Plate (B):	
Wafer: Silicon <100>, n-type prime, thickness=450 um, double-side polished	
Measure wafer bow and thickness	
Alignment marks (front side)	*Mask A0-Marks-1;* expose only the alignment marks
Shallow Si etch for FTB overall gap: 1.0um (back side)	*Mask B1b-FTB-Gap (dark field)*
Thin Photo - IR (expose alignment marks) + coat back	standard thin photo-resist (1um)
AME5000 "UNDOPED-POLY-ETCH" 1.0um deep	(previous 1.5um was ~175s; use monitor to set time; time to be determined)
Piranha	ICL strip bath
Shallow Si etch for FTB hydrostatic-only gap: 0.5um (back side)	*Mask B7b-hd-hydrostatic-gap (dark field)*
Thin Photo - IR (expose alignment marks) + coat back	standard thin photo-resist (1um)
AME5000 "UNDOPED-POLY-ETCH" 0.5um deep	(previous 1.5um was ~175s; use monitor to set time; time to be determined)
Piranha	ICL strip bath
Shallow Si etch for FTB hydrodynamic spiral grooves: 2.0-2.4um (2.2 pre	*Mask B6b-hd-spiralgrooves (dark field)*
Thin Photo - IR (expose alignment marks) + coat back	photo-resist thickness to be determined
AME5000 "UNDOPED-POLY-ETCH" 2.2um deep	(previous 1.5um was ~175s; use monitor to set time; time to be determined)
Piranha	ICL strip bath
Shallow Si etch for Tip Clearance : 12.5um, (back side)	*Mask B2b-Tip-clearance (dark field)*
Thick Photo (hide alignment marks) + coat back	TRL thick resist: AZ4620 8um thick
STS "UNDOPED-POLY-ETCH" 12.5um deep	(~1450 s, use monitor to set time)
Piranha	ICL
Deep Si etch for collector and FTB plenum: 350um (front side)	*Mask B5-hd-Collector-3 (dark field)*
Thick Photo (hide alignment marks) + coat back (protect from residu	TRL thick resist: AZ4620 10um thick
STS	350um deep, MIT59 (~2h40)
Piranha	TRL
Oxide protective coating (front side)	Thicker then standard: >0.5 um to prevent back side pitting: 1um, 450C.
Deep Si etch for FTB orifices: 100um (back side)	*Mask B4b-hd-orifices-3 (dark field)*
Thick Photo (hide alignment marks) + handle wafer	TRL thick resist: AZ4620 6um thick
STS	100um deep, MIT59 (~1h45)
Piranha	TRL
Rotor Plate (C):	
Wafer: Silicon <100>, n-type prime, thickness=450um, double-side polished	
Measure wafer bow and thickness	
Alignment marks (front side)	*Mask A0-Marks-1;* expose only the alignment marks
Alignment marks (back side) - Send to EV for aligned exposure	*EV has a mask with the 3um wide, 72mm apart alignment marks*
Following steps may be modified for the journal-first approach:	
Deep Si etch for blades: 150um (front side)	*Mask C6-Turbine-2 (dark field)*
Thick Photo (hide alignment marks)	TRL thick resist: AZ4620 8um thick
STS	150um deep, MIT51 (~55min) - recipe used for ubearing rig
Piranha	TRL or ICL
Bond B-C to create rotor combo	
RCA clean in TRL	
EV aligner/bonder	Aligned and contact B to C; bond with "minustwo" recipe
Anneal in TRL tube A2	1100 C for 1hr
Deep Si etch for journal: 300um (back side)	*Mask C7-Journal (dark field)*
Thick Photo (hide alignment marks) + handle wafer and PR ring	TRL thick resist: AZ4620 10um thick
STS	300um deep, through wafer, tailored recipe
Piranha	TRL
BOE to remove the front side oxide on FEP	1min per 1000A

Figure B-2: Fabrication Process Flow for Motor-Compressor Bearing rig Version 1.5—Part 1. [Adapted from Fréchette [31]]

3

Aft End Plate (D)

Wafer: Silicon <100>, n-type prime, thickness=450um, double-side polished	
Alignment marks (back side)	*Mask A0-Marks-1;* expose only the alignment marks
Shallow Si etch for ATB overall gap: 1.0um (front side)	*Mask C1b-ATB-gap (dark field)*
Thin Photo - IR (expose alignment marks) + coat back	standard thin photo-resist (1um)
AME5000 "UNDOPED-POLY-ETCH" 1.0um deep	(previous 1.5um was ~175s; use monitor to set time; time to be determined)
Piranha	TRL or ICL strip bath
Shallow Si etch for ATB hydrostatic-only gap: 0.5um (front side)	*Mask D10-hd-hydrostatic-gap (dark field)*
Thin Photo - IR (expose alignment marks) + coat back	standard thin photo-resist (1um)
AME5000 "UNDOPED-POLY-ETCH" 0.5um deep	(previous 1.5um was ~175s; use monitor to set time; time to be determined)
Piranha	ICL strip bath
Shallow Si etch for ATB hydrodynamic spiral grooves: 2.0-2.4um (2.2 pre	*Mask D9-hd-spiralgrooves (dark field)*
Thin Photo - IR (expose alignment marks) + coat back	photo-resist thickness to be determined
AME5000 "UNDOPED-POLY-ETCH" 2.2um deep	(time to be determined, use monitor to set time)
Piranha	ICL strip bath
Shallow Si etch for pits: 8.5um gap (frontside)	*Mask C2b-Rot-pits (dark field)*
Thin Photo (hide alignment marks) + coat back	standard thin photo-resist (1um)
AME5000 or STS "UNDOPED-POLY-ETCH" 8.5um deep	process time to be determined.
Piranha	TRL or ICL strip bath
Deep Si etch for aft piping: 350um (back side)	*Mask D8b-hd-Piping-3 (dark field)*
Thick Photo (hide alignment marks)	TRL thick resist: AZ4620 10um thick
STS	350um deep, MIT59 (~2:15hrs)
Piranha	TRL
Oxide protective coating (front side)	Thicker than standard: >0.5um to prevent back side pitting
Deep Si etch for ATB orifices: 100um (front side)	*Mask D7-hd-Orifices-3 (dark field)*
Thick Photo (hide alignment marks) + handle wafer	TRL thick resist: AZ4620 6um thick (5000rpm)
STS	100um deep, MIT59 (~1:30 hrs)
Piranha	TRL

Aft Foundation Plate (E)

Wafer: Silicon <100>, n-type prime, thickness=450um, double-side polished	
Alignment marks (front side)	*Mask A0-Marks-1;* expose only the alignment marks
Alignment marks (back side)	*Mask A0-Marks-1;* expose only the alignment marks
oxide protection of back side (optional, aesthetic only)	0.1um (standard)
Deep Si etch for holes: 200um (back side)	*Mask E2b-Foundation (dark field)*
Thick Photo (hide alignment marks)	TRL thick resist: AZ4620 10um thick
STS	200um deep, MIT59 (~1h30)
Piranha	TRL
Deep Si etch for aft piping: 250um	*Mask E1-hd-Piping-2 (dark field)*
Thick Photo - (hide alignment marks)	TRL thick resist: AZ4620 10um thick
STS	250um deep, MIT59 (~2h00)
Piranha	TRL

Device assembly and completion

Bond entire stack in one process	(order of wafers can be inverted, if desired)
Asher in TRL	To completely clear photoresist from small features
Piranha	TRL
RCA clean	TRL
EV aligner, silicon-direct-bonding	Contact A-BC by inserting A first. Don't remove from aligner
EV aligner, silicon-direct-bonding	Contact ABC-D by resending ABC back in, then inserting D
EV aligner, silicon-direct-bonding	Contact ABCD-E by resending ABCE back in, then inserting E
EV Bonder (this step was not done on first 2 MCBR builds)	Bond stack with "minustwo" recipe, to improve contact
Inspect alignment visually before anneal	Speed sensor contacts, inlet tabs, ...
Anneal in TRL tube A2	1100 C for 1hr
Separate dies	
Die saw	
Rotor release	
Snap-off tabs	After flow characterization

Figure B-3: Fabrication Process Flow for Motor-Compressor Bearing rig Version 1.5—Part 2. [Adapted from Fréchette [31]]

B.2 New Mask Descriptions and Sample CAD Drawings

MCBR15 Mask Set Description **24/5/00**

Extension of MC14 masks set to include hybrid hydrodynamic thrust bearings

B6b-hd-spiralgrooves-df
Included spiral grooves for hydrodynamic action. From Matlab model. Etch depth of 2.0 to 2.4um with 2.2um preferred.

B5-hd-collector-3-df
Moved plenum inwards since hydrostatic nozzles moved inwards (positioned at 0.4mm radii).

B4b-hd-orifices-3-dfc
Move hydrostatic nozzles inwards so as to leave hydrodynamic action possible. Nozzle size still 7um on the mask.

B7b-hd-hydrostatic-gap-df
Second additional shallow etch to produce a different shallow etch depth from the gap of the spiral groove bearings. This etch is at 1.5um (total from new wafer) with tight tolerances.

B1b-ftb-gap-df
No change in mask except that etch depth is now 1.0um with very tight tolerance.

D10-hd-hydrostatic-gap-df
Similar to forward thrust bearings, a separate 1.5um (total, from new wafer) etch depth from hydrostatic modelling.

D7-hd-orifices-3-df
Similar to forward thrust bearings, moved nozzles inwards for sufficient place for hydrodynamic thrust bearing to function.

D9-hd-spiralgrooves-df
Similar to forward thrust bearings, a shallow etch of groove (2.0-2.4um, with 2.2um preferred).

D8b-hd-piping-3-df
Move ATB plenum since hydrostatic nozzles have moved inwards.

E1-hd-piping-2-df
Needed to move the deep etch for the exhaust since plenum moved too.

Figure B-4: Mask set description for MCBR15 that implements the hydrodynamic thrust bearing.

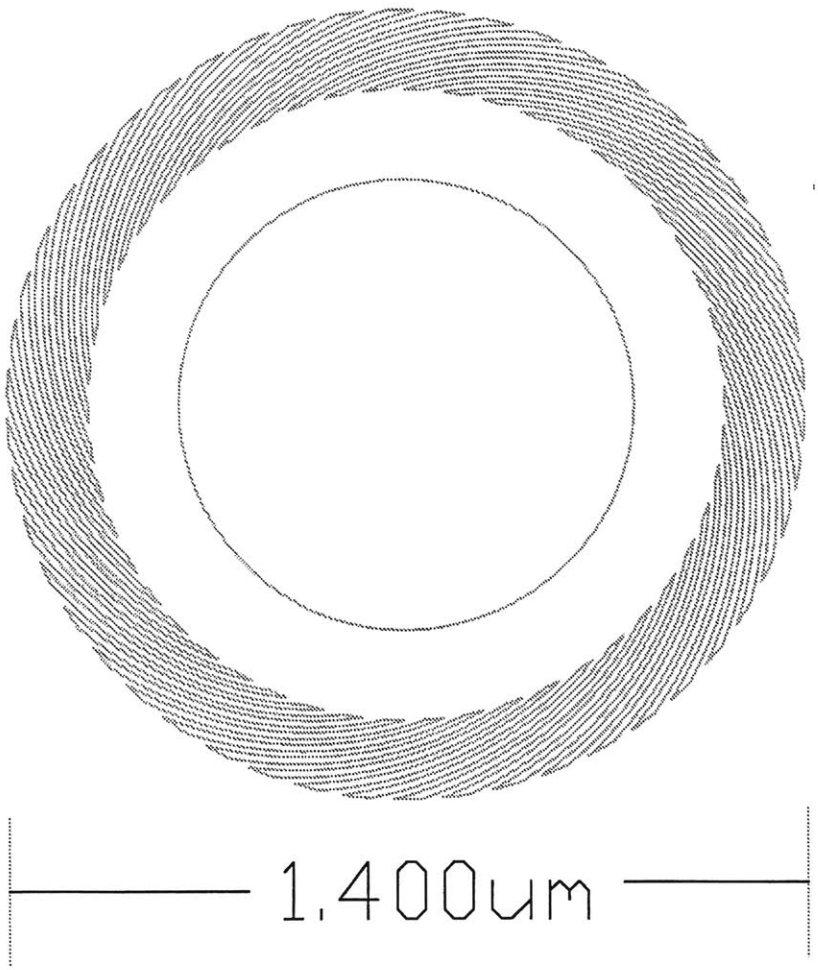

Figure B-5: Sample mask drawing: D9-hd-spiralgrooves-df—Spiral groove bearings on the aft thrust bearing.

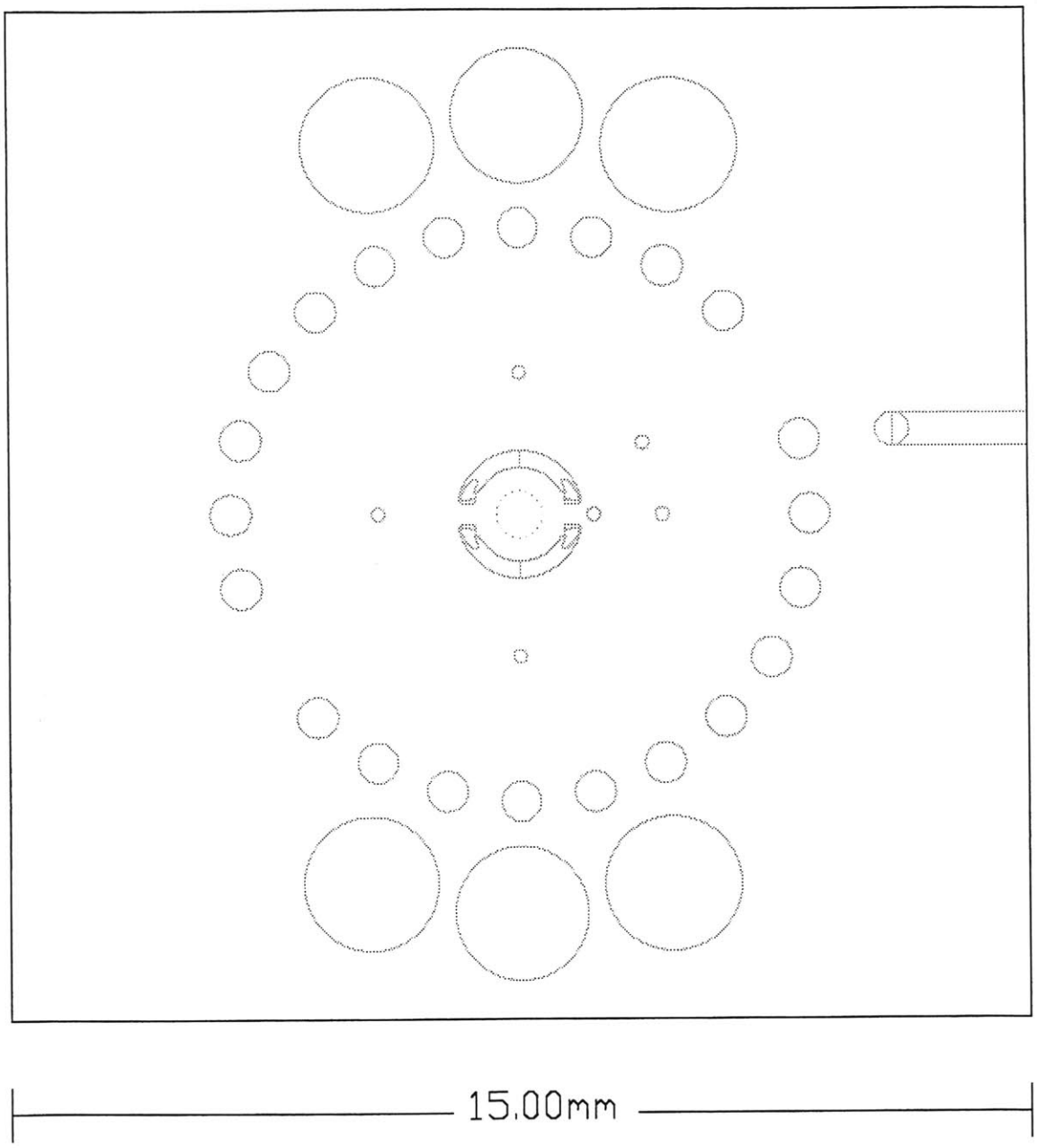

Figure B-6: Sample mask drawing: B4b-hd-orifices-3-df—Backside FEP with nozzles shifted (Adapted from Fréchette).

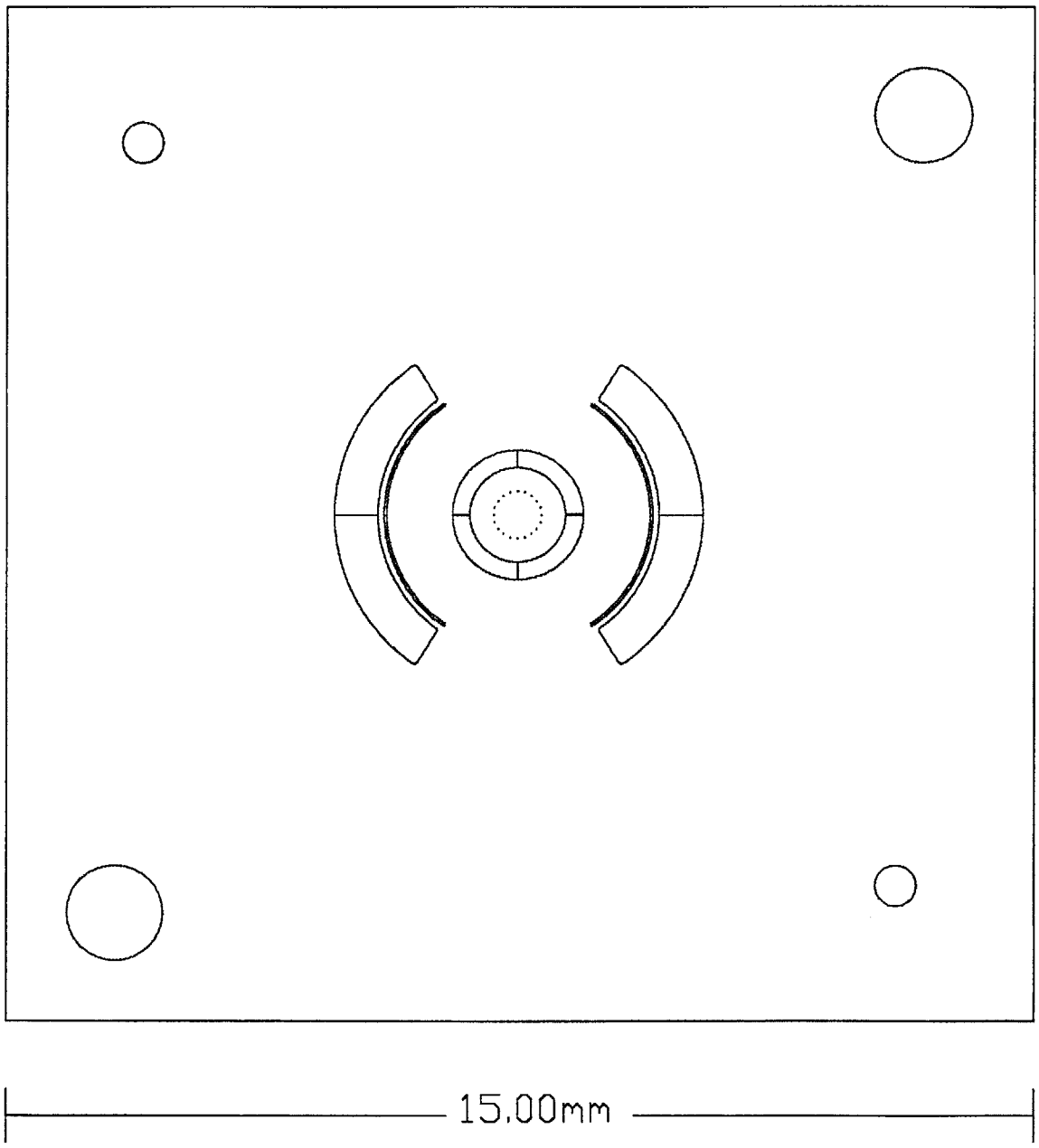

Figure B-7: Sample mask drawing: D7-hd-orifices-3-df—Frontside AEP with nozzles shifted (Adapted from Fréchette).

B.3 Fabrication checklists

Motor Compressor Bearing Rig Fabrication Summary Sheet
Build ____ ; Start Date ____ ; End Date ____

Wafer Level	ID number	Position in wafer box	Fabrication Status			Comments
			In Process	Completed	Selected for Build	
Forward Foundation Plate (FFP)						
Forward End Plate (FEP)						
Rotor Plate (RP)						
Aft End Plate (AEP)						
Aft Foundation Plate (AFP)						

Figure B-8: Wafers summary in fabrication.

Forward Foundation Plate Checklist

- ☐ Wafer: Silicon <100>, n-type prime, double-side polished, 450*um* thickness.
- ☐ Wafer ID number: ____ ; Position in box: _____
- ☐ Wafer Bow: _____ ; Wafer Thickness: _____
- ☐ Oxide Protective Coating (0.1*um*).

☐ Deep Etch—through-holes: 450*um*.

Forward End Plate Checklist

- ☐ Wafer: Silicon <100>, n-type prime, double-side polished, 450*um* thickness.
- ☐ Wafer ID number: ____ ; Position in box: _____
- ☐ Wafer Bow: _____ ; Wafer Thickness: _____
- ☐ Oxide Protective Coating (0.1*um*).

☐ First Shallow Etch for thrust bearing gap: (**1.0*um*** datum backside).

☐ For hydrodynamic hybrid: Second Shallow Etch for hydrostatic-only gap: (**1.5*um*** datum backside).

☐ For hydrodynamic hybrid: Third Shallow Etch for spiral grooves: (**3.4*um*** datum backside).

☐ Fourth Shallow Etch for tip clearance: (12.5*um* datum backside).

☐ Deep Etch for collector and plenum: (350*um* frontside) ; Deep Etch for nozzle: (100um backside).

☐ Nozzle size at **10.0*um*** (frontside) and **10.5*um*** (backside).

☐ All nozzles punched through.

- ➢ **Bold** dimensions indicate crucial dimensions for Motor Compressor Bearing Rig.
- ➢ All dimensions, otherwise stated, indicate depth or height.
- ➢ *"datum"* indicates from original surface of wafer before processing.

Figure B-9: Forward Foundation Plate and Forward End Plate checklists.

Rotor Plate Checklist

- ☐ Wafer: Silicon <100>, n-type prime, double-side polished, 450*um* thickness.
- ☐ Wafer ID number: ____ ; Position in box: _____
- ☐ Wafer Bow: _____ ; Wafer Thickness: _____
- ☐ Oxide Protective Coating (0.1*um*).

☐ (Frontside-Alignment-Mark) to (Backside-Alignment-Mark) misalignment: **±0.5*um***.

Frontside

☐ Blade (deep-etch; frontside) mask misalignment: **±1.0*um***

☐ Blade deep etch (150*um*) non-uniformity variation: **0.5*um*** center dies; **<2.0*um*** edge dies.

Backside

☐ Journal bearing (deep etch; backside) mask misalignment: **±1.0*um***

☐ No defects at journal bearing after photo and resist development.

☐ Journal bearing clearance: (**10.0*um*** frontside).

☐ Journal bearing straight vertical walls: **~0.2*um*** tapering for 100*um* deep etch.

➢ **Bold** dimensions indicate crucial dimensions for Motor Compressor Bearing Rig.

Figure B-10: Rotor Plate checklist

Aft End Plate Checklist

- ☐ Wafer: Silicon <100>, n-type prime, double-side polished, 450*um* thickness.
- ☐ Wafer ID number: ____ ; Position in box: _____
- ☐ Wafer Bow: _____ ; Wafer Thickness: _____
- ☐ Oxide Protective Coating (0.1*um*).

- ☐ First Shallow Etch for thrust bearing gap: (**1.0*um*** frontside).
- ☐ For hydrodynamic hybrid: Second Shallow Etch for hydrostatic-only gap: (**1.5*um*** datum frontside).
- ☐ For hydrodynamic hybrid: Third Shallow Etch for spiral grooves: (**3.4*um*** datum frontside).
- ☐ Fourth Shallow Etch for generator gap: (8.5*um* datum frontside).
- ☐ Deep Etch for collector and plenum: (350*um* backside).
- ☐ Deep Etch for nozzle: (100um backside, **10.0um** nozzle diameter).
- ☐ All nozzles punched through.

Aft Foundation Plate Checklist

- ☐ Wafer: Silicon <100>, n-type prime, double-side polished, 450*um* thickness.
- ☐ Wafer ID number: ____ ; Position in box: _____
- ☐ Wafer Bow: _____ ; Wafer Thickness: _____
- ☐ Oxide Protective Coating (0.1*um*).

- ☐ Deep Etch—aft-piping: 250*um* frontside.
- ☐ Deep Etch—holes: 200*um* backside.

- ➢ **Bold** dimensions indicate crucial dimensions for Motor Compressor Bearing Rig.
- ➢ All dimensions, otherwise stated, indicate depth or height.
- ➢ "*datum*" indicates from original surface of wafer before processing.

Figure B-11: Aft End Plate and Aft Foundation Plate checklists.

B.4 Experimental Preparation Checklist

Test Procedure for Motor Compressor Bearing Rig

- ☐ Motor Compressor Bearing Rig number: _____ ; Date started test preparation: _____

Wafer Die-Saw
- ☐ Follow die-saw procedures in handbook beside the die-saw machine.
- ☐ Without removing die-saw UV tape, wash out silicon slurry along each die's edges
- ☐ Remove die-saw UV tape after at least $30s$ UV exposure.

Static Flow testing
- ☐ Characterize Aft Thrust Bearing and Forward Thrust Bearing flowrates. Keep thrust bearings pressurized equally, if possible, to reduce stress on tabs.
- ☐ Characterize journal bearing flowrates.

Breaking-off Tabs
- ☐ All tabs fragments are visually seen outside package after breaking off tabs.
- ☐ All tab pillars at root.
- ☐ Inverted "blow-out" test to get rid of residual tab fragments.

Free flow testing
- ☐ Set both thrust bearings at equal increments for initial test (from 0-100psi).
- ☐ Characterize each thrust bearing, finding optimal equilibrium for "float" position.
- ☐ Seek operating limits for each thrust bearing.
- ☐ Characterize journal bearing free-rotor flowrates.

Before actual run
- ☐ Check N_2/air cylinder on 1st level GTL for possible 6-8 hours operation
- ☐ Check for fluidic leakage on the test rig piping.
- ☐ Check pressure transducers and mass flow controllers have the physical ranges as required, and that this is reflected on the data acquisition configuration. Supply voltage to these instruments at $8.0V$.
- ☐ Re-zero pressure transducers (with data acquisition system) and mass flow controllers/meters (with the zeroing knob on the controllers/meters.
- ☐ Position and insert optical sensor probe without strain on die; push sensor against entry hole if needed. Tune optical sensor supply voltage to $12.0V$.
- ☐ If using potentiometer for control of mass flow, set supply voltage to potentiometer at $5.0V$. Unplug main air piping to the rig and turn up potentiometer to set mass flow controller valve open. (There will be a sudden increase in mass flow.) Plug main air piping back.
- ☐ Seek favorable square-wave signal (by positioning optical sensor) and confirm signal response frequency.
- ☐ Calibrate frequency-to-voltage converter against spectrum analyzer signal, if needed. Switch to "hi-range" when speed above 100,000rpm.

After actual run
- ☐ Check calibration of mass flow controllers and pressure transducers, especially ones for low and high plenums of Motor Compressor Bearing Rig.

Figure B-12: Preparation checklist of fabricated dies for testing.

B.5 Data Acquisition modules

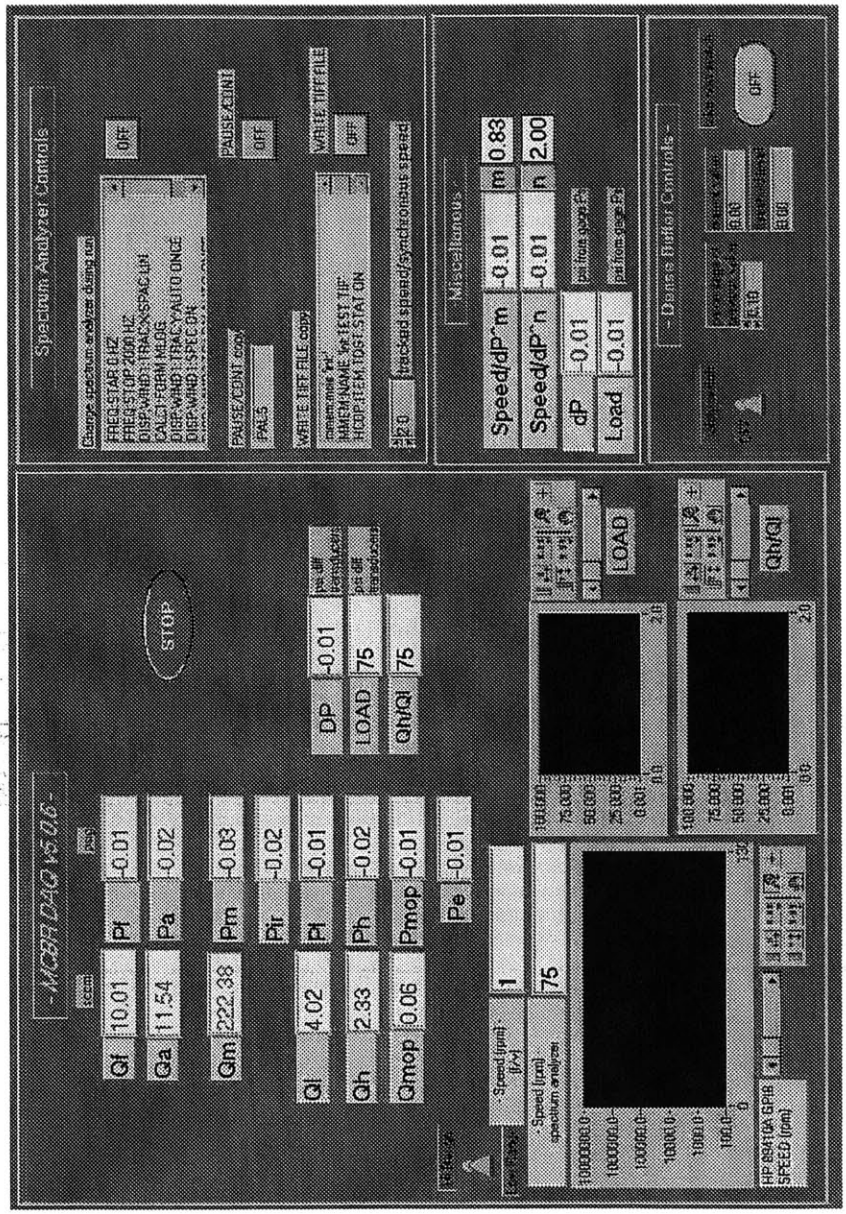

Figure B-13: Control panel of data acquisition module—Part 1.

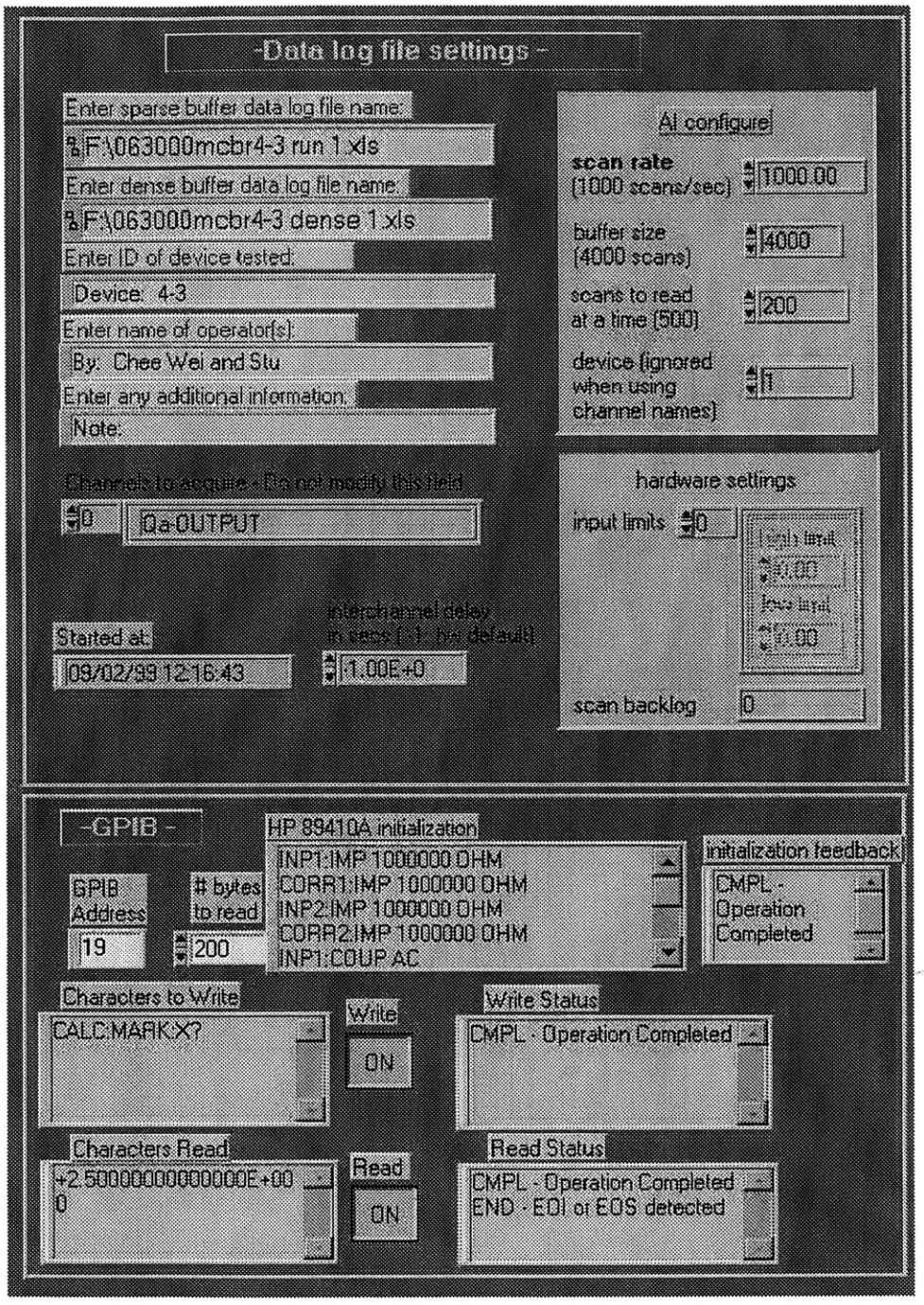

Figure B-14: Control panel of data acquisition module—Part 2.

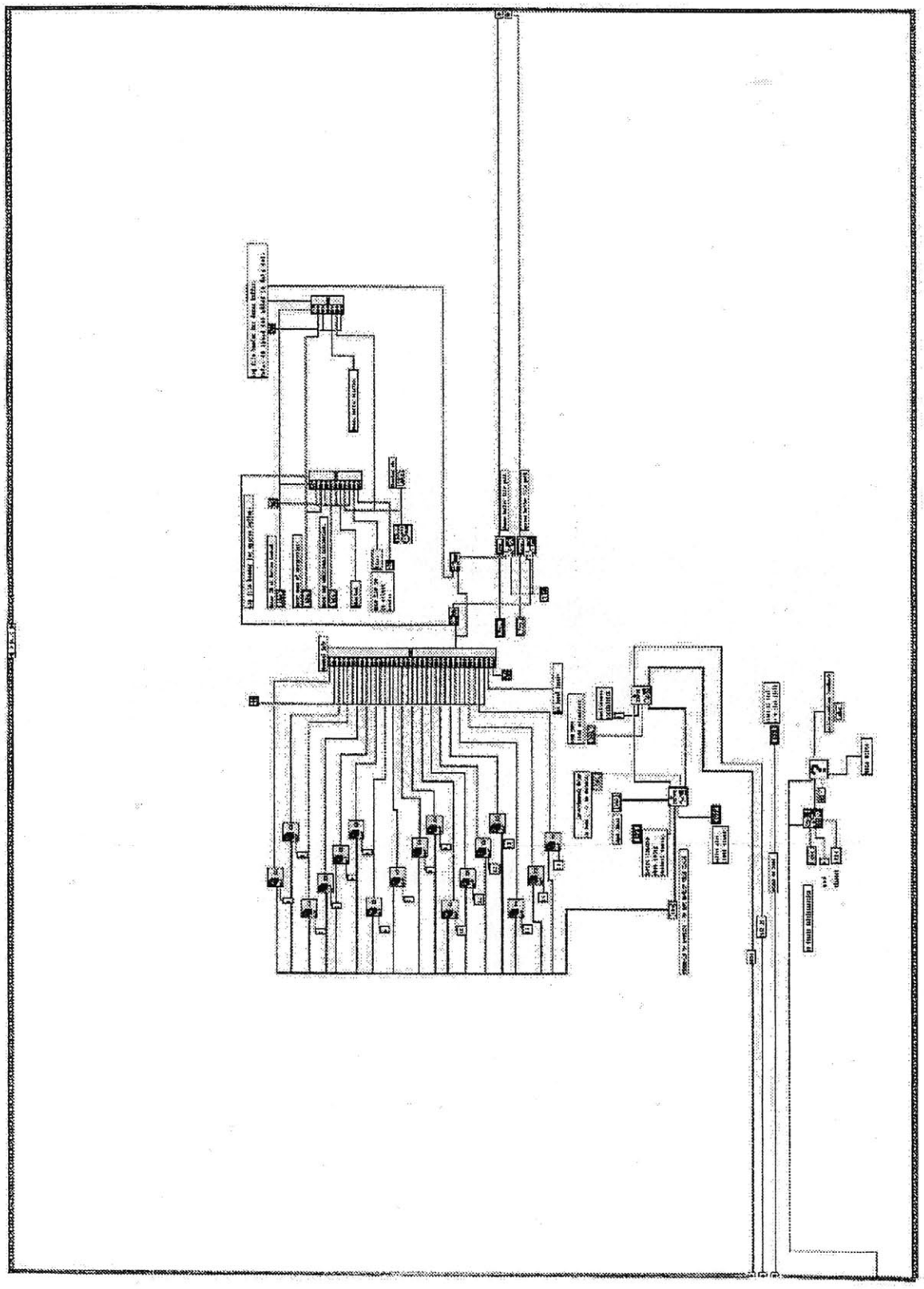

Figure B-15: General overview of the module to acquire low speed (1kHZ) run-time data—Frame 0.

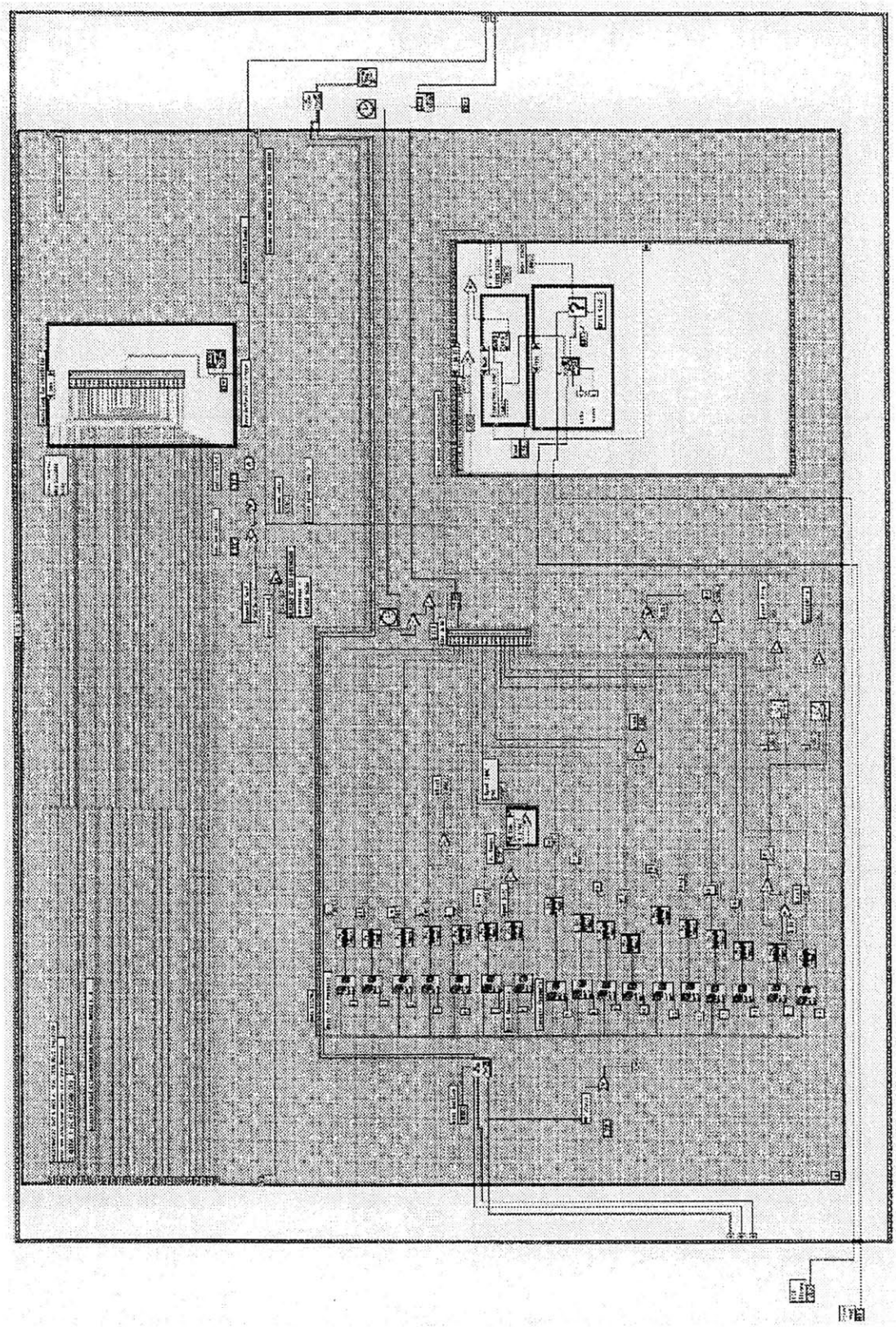

Figure B-16: General overview of the module to acquire low speed (1kHZ) run-time data—Frame 1.

Appendix C

Operation results of MicroBearing Rig

C.1 Static and Free flow testings of the MicroBearing Rig

Illustrated here is the summary of the static and free flow testing of the Microbearing rig before actual operation. We note that the flowrates of the thrust bearings in the many devices are similar to each other and, while flowrates in the Low/High plenums of the journal bearing may be dissimilar, this difference in flowrates sometimes do correct themselves out upon opeartion. Indeed, some dies have large differences in Low/High journal bearing flowrates, but spin up pretty well.

C.2 Sample natural frequency spectra of interest

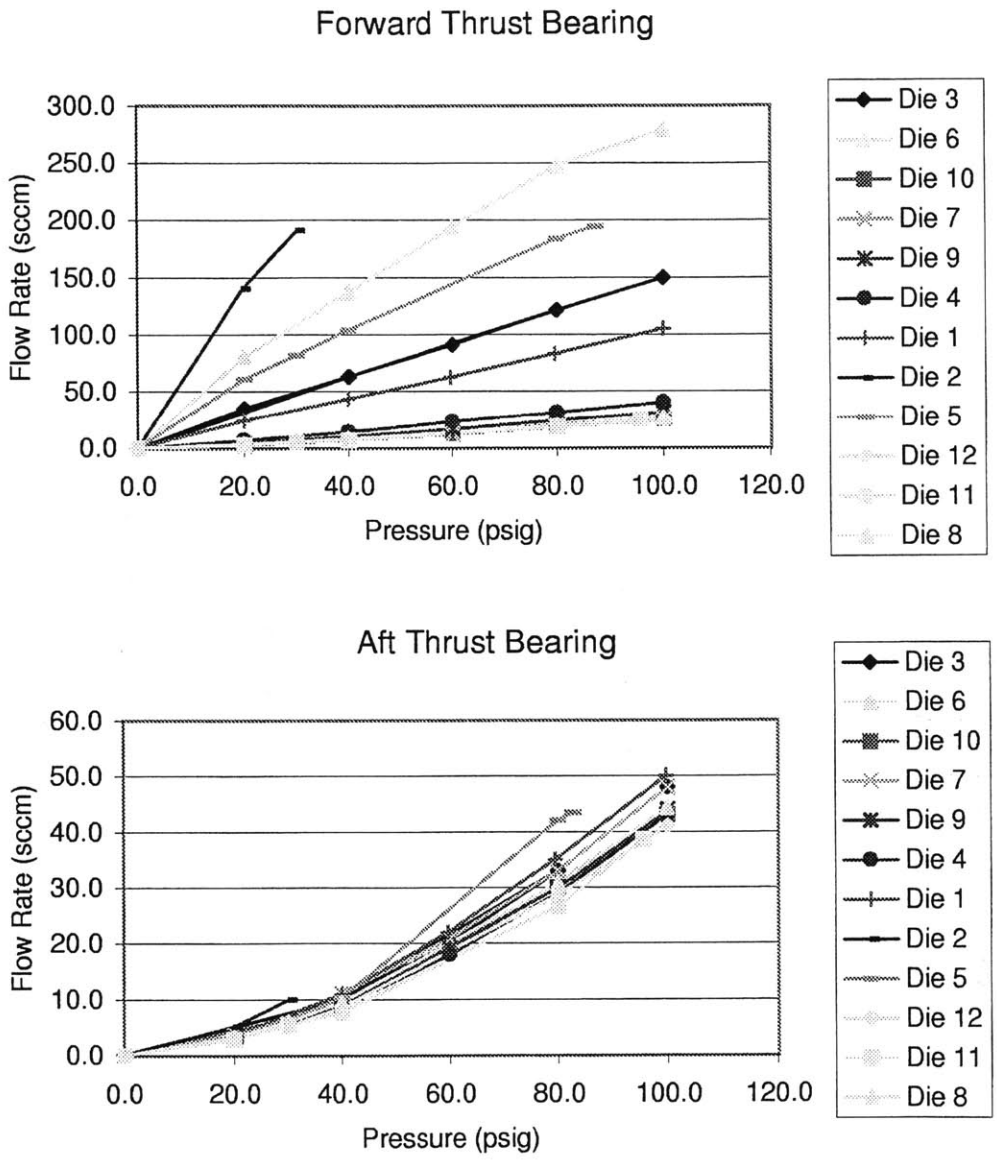

Figure C-1: Summary of the fixed rotor thrust bearing flowrates, in correspondence with Figure 3-5.

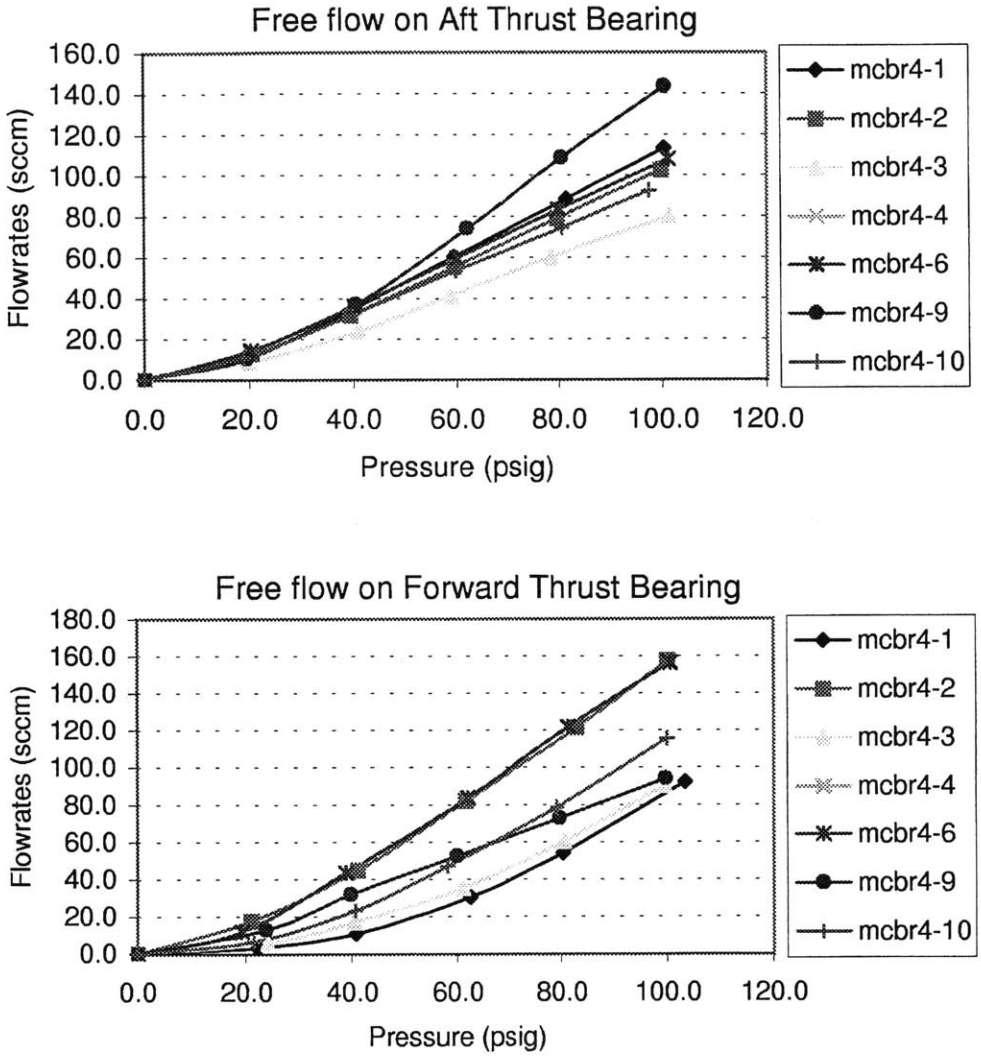

Figure C-2: Summary of the released rotor thrust bearing flowrates, in MicroBearing Build 4.

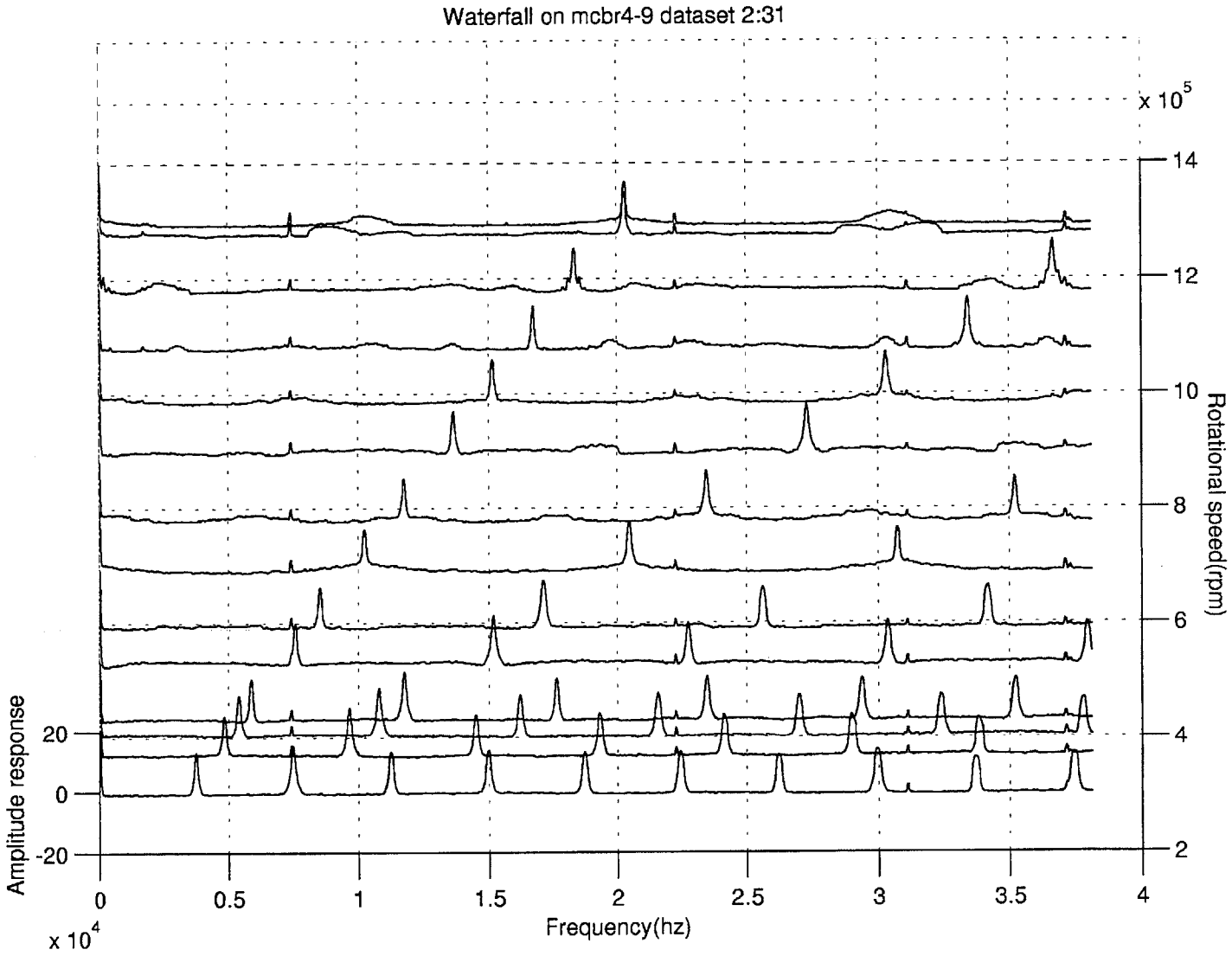

Figure C-3: A waterfall plot of frequency spectra, showing the integer multiples of the synchronous speed.

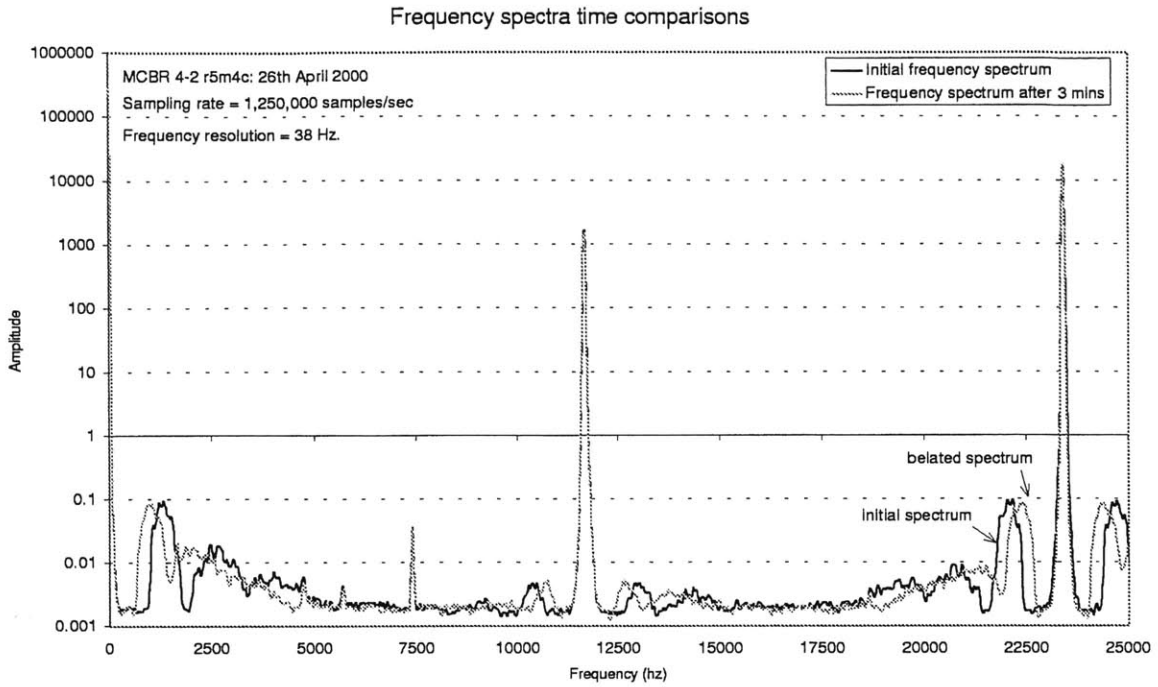

Figure C-4: Time dependence of the natural frequency.

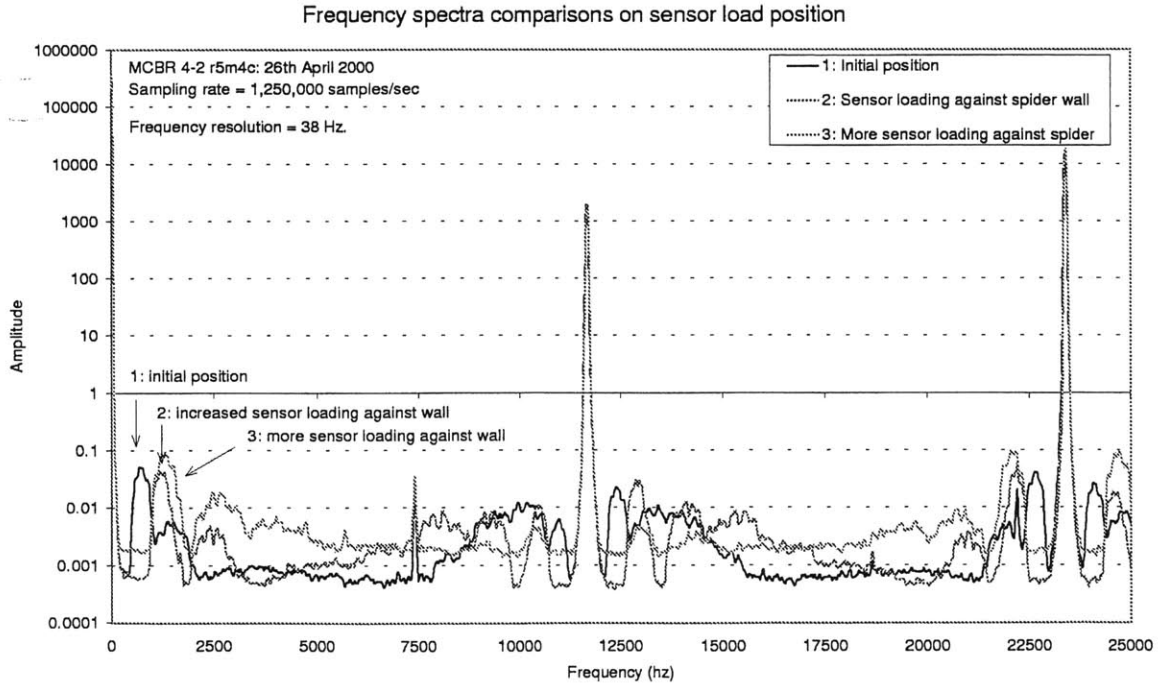

Figure C-5: Natural frequency variations with speed sensor load position against entry "spider wall" hole.

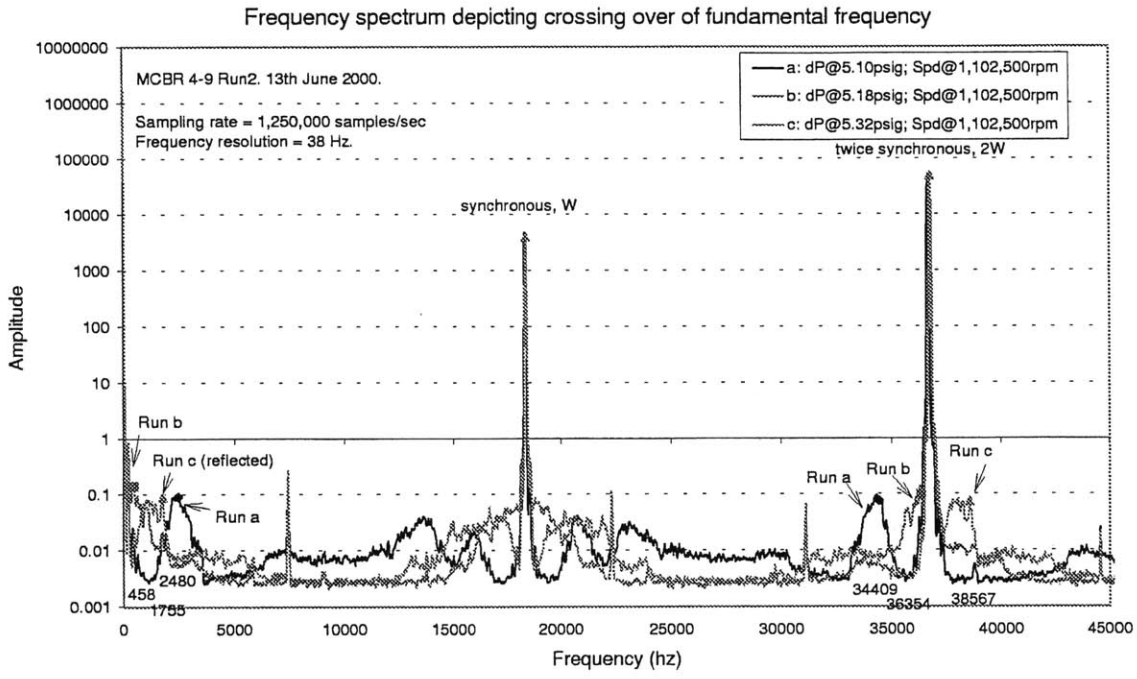

Figure C-6: A sample frequency spectrum delineating crossing the fundamental natural frequency, effected by increases in axial differential pressure.

C.3 Other windowing procedures

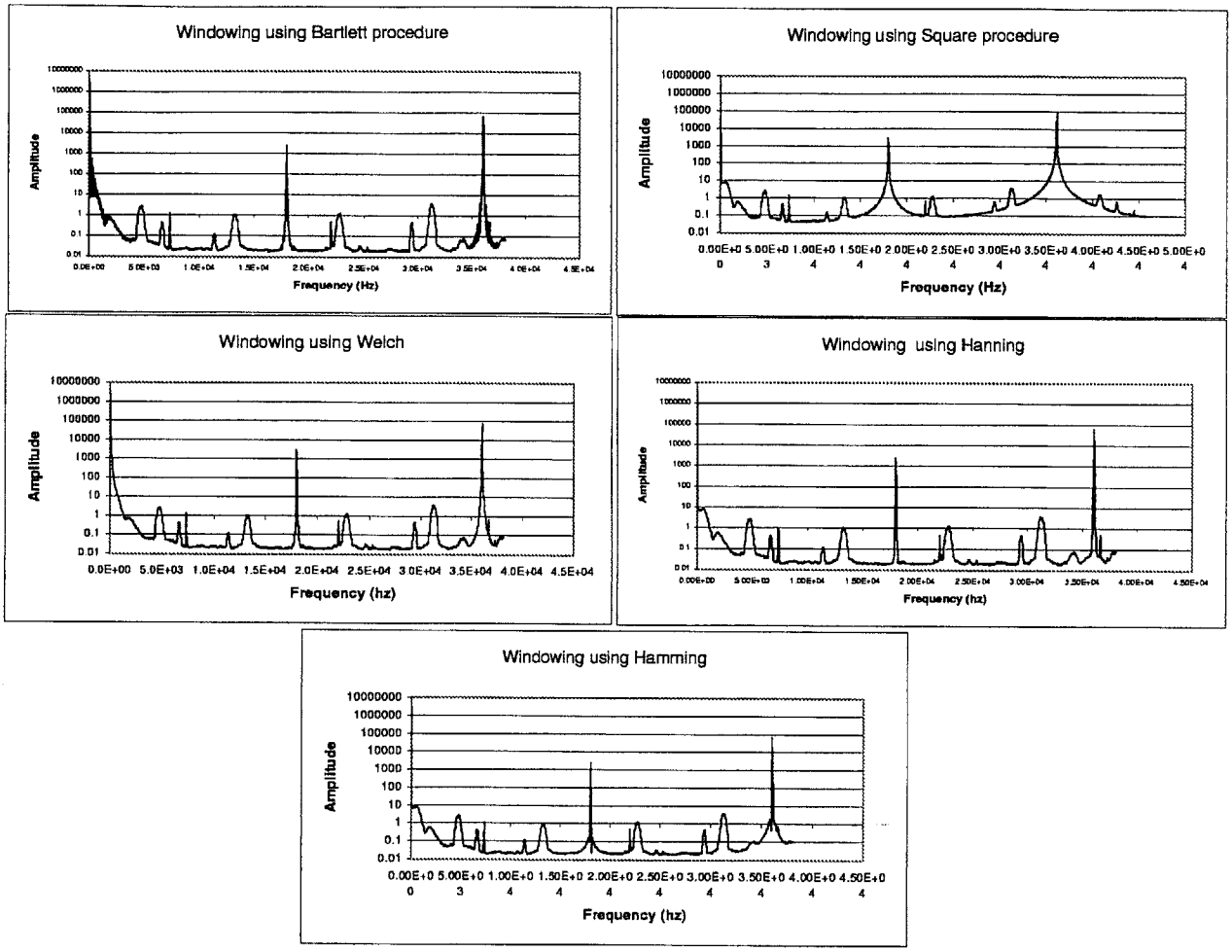

Figure C-7: Comparision of five windowing procedures.

Appendix D

Hydrodynamic thrust bearing—Design results

D.1 Summary of design geometries and results

Forward Thrust Bearing (at 200,000 rpm)

Design Geometries		*Resultant performance parameters*	
Number of grooves, k	50	Compression number	5.6
Bearing gap (um)	1.0 (tight)	Stability Parameter	0.20
Groove Depth (um)	2.4(2.0-2.4)		
Outer groove radius (um)	700		
Inner groove radius (um)	560		
Groove spiral angle	16°		
Ratio of groove-ridge widths	1.2		

Aft Thrust Bearing (at 200,000 rpm)

Design Geometries		*Resultant performance parameters*	
Number of grooves, k	50	Compression number	5.6
Bearing gap (um)	1.0	Stability Parameter	0.20
Groove Depth (um)	2.4(2.0-2.4)		
Outer groove radius (um)	700		
Inner groove radius (um)	560		
Groove spiral angle	16°		
Ratio of groove-ridge widths	1.2		

Combined performance of both FTB and ATB (at 200,000 rpm)

Load capacity @50% eccentricity (N)	0.0572
Load capacity @zero eccentricity (N)	0.0
Stiffness (N/m) @50% eccentricity	1.63E05
Stiffness (N/m) @zero eccentricity	9.34E04
Wn/rotational speed @50% eccentricity	6.82
Wn/rotational speed @zero eccentricity	5.16
Drag (W) @50% eccecntricity	0.0036
Drag (W) @zero eccecntricity	0.0028

Figure D-1: Summary of optimized design and performances.

D.2 Main and end-effect correction factors

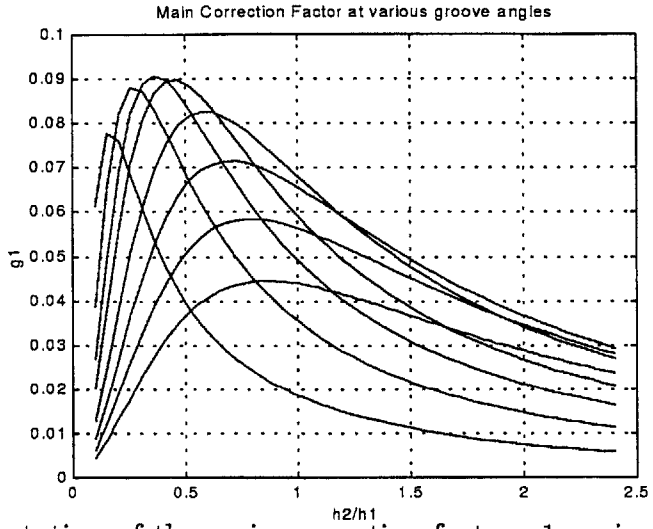

Figure D-2: Representation of the main correction factor $g1$ against different δ and groove angle α.

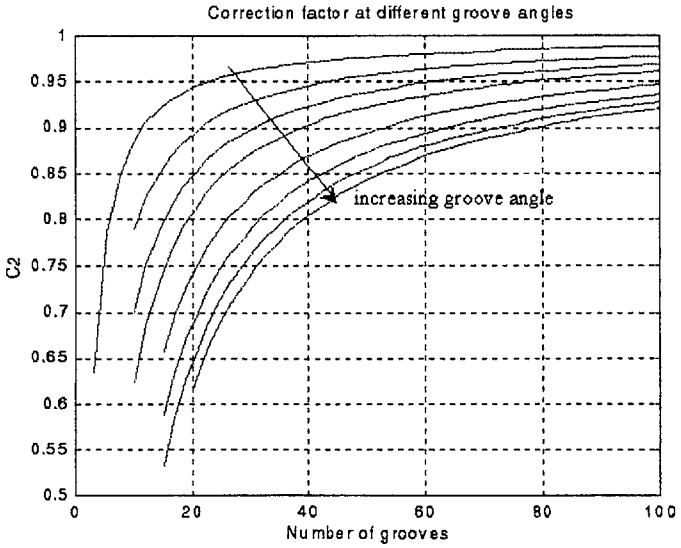

Figure D-3: Representation of the correction factor C_2 against different number of grooves k and groove angle α.

Bibliography

[1] K. Atkins and R. Perez. Influence of gas seals on rotor stability of a high speed hydrogen recycle compressor. Proceeding of the 17th turbomachinery symposium, Texas A&M University, 1988.

[2] A.A Ayón, X. Zhang, and R. Khanna, editors. *Ultra Deep Anisotropic Silicon Trenches Using Deep Reactive Ion Etching*, Solid-State Sensor and Actuator Workshop, Hilton Head, South Carolina, 2000.

[3] M.B. Banerjee, R.G. Shandil, S.P. Katyal, G.S. Dube, K.S. Pal, and K. Banerjee. A non-linear theory of hydrodynamic lubrication. *Journal of Mathematical Analysis and Applications*, 117(1):266–274, jul 1986.

[4] S.F. Bart. *Modeling and Design of Electroquasistatic Microactuators.* PhD thesis, Massachusetts Institute of Technology, 1990.

[5] T.G. Beckwith, R.D. Marangoni, and J.H. Lienhard. *Mechanical Measurements.* Addison-Wesley-Longman, fifth edition, 1993.

[6] M.S Bhatti and C.W. Savery. Heat transfer in the entrance region of a straight channel:laminar flow with uniform wall heat flux. *ASME-AIChE Heat Transfer Conference*, pages 76–HT–20, aug 1976.

[7] G. A. Bird. *Molecular Gas Dynamics.* The Oxford Engineering Science Series. Clarendon Press, Sydney, Australia, first edition, 1976.

[8] E.F. Boon and S.E. Tal. Hydrodynamische dichtung fur rotierende wellen. Chemie - Ing. - Techn, 31 January 1959. Nr:3, p.202.

[9] Kenneth S. Breuer. Personal Communication. Visiting Associate Professor of Aeronautics and Astronautics. Massachusetts Institute of Technology, 2000.

[10] Dye-Zone A. Chen. Design and calibration of an infrared position sensor. Master of science in mechanical engineering thesis, Massachusetts Institute of Technology, 1999.

[11] Dara Childs. *Turbomachinery Rotordynamics.* John Wiley & Sons, Inc., New York, New York, first edition, 1993.

[12] J.E.R Coney and M.A.I El-Shaarawi. A contribution to the numerical solution of developing laminar flow in the entrance region of concentric annuli with rotating inner walls. *Journal of Fluids Engineering*, pages 333–340, December 1974.

[13] V.N. Constantinescu. Gas lubrication. *ASME*, 1969. Translated from Romanian 'Lubrificatia cu gaze', Ed. Acad., 1963.

[14] V.N. Constantinescu and S. Galetuse. On the dynamic stability of the spiral-grooved gas-lubricated thrust bearing. *Journal Of Tribology*, 109:183–188, January 1987.

[15] V.N. Constantinescu and S. Galetuse. Stability criterion for spiral groove thrust gas bearings. *Journal Of Tribology:Transaction of ASME*, 112:734–737, October 1990.

[16] S. Crandall, editor. *From Whirl to Whip in Rotordynamics*, Transactions, IFToMM 3rd International Conference on Rotordynamics, Lyon, France, 1990.

[17] R.C. DiPrima and J.T. Stuart. Flow between eccentric rotating cylinders. *Journal of Lubrication Technology*, pages 266–274, jul 1972.

[18] D. Dowson. A generalized reynolds equation for fluid-film lubrication. *Int. Journal Mech. Sci., Pergamon Press. Ltd*, 4:159–170, 1962.

[19] Mark Drela. MIT 16.13 class lectures, 1994.

[20] Eric K. Drexler. *Nanosystems: molecular machinery, manufacturing, and computation.* Wiley Interscience, first edition, 1992.

[21] Frederic F. Ehrich. Personal Communication. MIT MicroEngine Project, Massachusetts Institute of Technology, 2000.

[22] Fredric F. Ehrich. Sum and difference frequencies in vibration of high speed rotating machinery. *Journal of Engineering for Industry*, pages 181–184, 1972.

[23] Fredric F. Ehrich. *Handbook of Rotordynamics.* Krieger Publishing Company, Inc., Malabar, Florida., second edition, 1999.

[24] Epstein et al. Micro Turbine Generators. Final Technical Report prepared for MIT Lincoln Laboratory, 1995.

[25] Epstein et al. Micro Gas Turbine Generators. First Semi-Annual Interim Technical Progress Report on Grant DAAH04-95-1-0093, January 1996.

[26] Epstein et al. Power MEMS and Microengines. Presented at IEEE Conference on Solid State Sensors and Actuators, Chicago, IL, June 1997.

[27] Epstein et al. Micro-Heat Engines, Gas Turbines, and Rocket Engines. AIAA 97-1773, presented at 28th AIAA Fluid Dynamics Conference, 4th AIAA Shear Flow Control Conference, Snowmass Village, CO, June 1997.

[28] Epstein et al. The MIT Microengine Project. Annual Technical Report, January 1999.

[29] Richard P. Feynman. There's plenty of room at the bottom. Transcript of a talk given Dr. Feynman, California Institute of Technology, Pasadena, California, 1961.

[30] G.W.K. Ford, D.M. Harris, and D. Pantall. Principles and applications of hydrodynamic type gas bearings. *Proc. of the Institution of Mechanical Engineers*, 171(2):93, 1957.

[31] Luc G. Frechette. *Development of a microfabricated silicon motor-driven compression system.* PhD dissertation, Massachusetts Institute of Technology, Department of Aeronautics and Astronautics, August 2000.

[32] C. Groshenry. Preliminary study of a micro-gas turbine engine. Master's thesis, Massachusetts Institute of Technology, 1995.

[33] Bernard J. Hamrock. Optimization of self-acting step thrust bearings for load capacity and stiffness. *ASLE Trans.*, 15(23):159–170, 1972.

[34] Bernard J. Hamrock. *Fundamentals of fluid film lubrication.* McGraw-Hill series in mechanical engineering. McGraw-Hill, c1994, New York, first edition, 1994.

[35] Stuart A. Jacobson. Personal Communication. Associate Chief Engineer, MIT Micro-Engine Project. Massachusetts Institute of Technology, 2000.

[36] Stuart A. Jacobson. Aerothermal Challenges in the Design of a Microfabricated Gas Turbine Engine. AIAA 98-2545, presented at the 29th AIAA Fluid Dynamics Conference, Albuquerque, NM, June 1998.

[37] Jack L. Kerrebrock. *Aircraft engines and gas turbines.* The MIT Press, Cambridge, Massachusetts, second edition, 1992.

[38] R.H. Larson and H.H. Richarson. A preliminary study of whirl instability for pressurized gas bearings. *Journal of Basic Engineering*, pages 511–520, December 1962.

[39] L. Licht, D.D. Fuller, and B. Sternlicht. Self excited vibrations of an air-lubricated thrust bearing. *ASME*, 80(2):411–414, February 1958.

[40] Chuang-Chia Lin. *Development of a Microfabricated Turbine-Driven Air Bearing Rig.* PhD dissertation, Massachusetts Institute of Technology, Department of Mechanical Engineering, June 1999.

[41] S.B. Malanoski and C.H.T Pan. The static and dynamic characteristics of the sprial-grooved thrust bearings. *Journal of Basic Engineering:Transaction of ASME*, pages 547–558, September 1965.

[42] Mechanical Technology Incorporated. *Design of Gas Bearings.* Two volumes: Twelve sections. Mechanical Technology Incorporated, 1968–90.

[43] A. Mehra, S.A. Jacobson, C.S Tan, and A.H. Epstein. Aerodynamic Design Considerations for the Turbomachinery of a Micro Gas Turbine Engine. Presented at the 25th National and 1st International Conference on Fluid Mechanics and Power, New Delhi, India, December 1998.

[44] A. Mehra and I.A. Waitz. Development of a hydrogen combustor for a microfabricated gas turbine engine. Presented at Solid-State Sensor and Actuator Workshop, Hilton Head Island, SC, June 1998.

[45] Amitav Mehra. *Development of a High Power Density Combustion System for a Silicon Micro Gas Turbine Engine.* PhD dissertation, Massachusetts Institute of Technology, Department of Aeronautics and Astronautics, February 2000.

[46] A.R Mirza and A.A Ayón. Silicon wafer bonding: The key enabling technology for mems high-voume manufacturing. *Future Fab International*, 6:51–56, 1999.

[47] E.A. Muijderman. *Spiral Groove Bearings.* Philips Technical Library, N.V. Philips' Gloeilampenfabrieken, Eindhoven, The Netherlands, 1966.

[48] J. O. Mur Miranda. Feasibility of electrostatic bearings for micro turbomachinery. Masters in engineering thesis, Massachusetts Institute of Technology, MIT Department of Electrical Engineering and Computer Science, 1997.

[49] A. Muszynska. Whirl and whip-rotor/bearing stability problems. *Journal of Sounds and Vibrations*, 110:443–462, 1986.

[50] S.F. Nagle and J.H. Lang. A Micro-scale Electric-Induction Machine for a Micro Gas Turbine Generator. Presented at the 27th Annual Meeting of the Electrostatic Society of America, June 1999.

[51] Steven F. Nagle. *Analysis, Design and Fabrication of an Electric Induction Micromotor for a Micro Gas-Turbine Generator.* PhD dissertation, Massachusetts Institute of Technology, Department of Electrical Engineering and Computer Science, July 2000.

[52] C. Nataraj, H. Ashrafiuon, and N.K. Arakere. Effect of fluid inertia on journal bearing parameters. *Tribology Trans.*, 37:784–792, 1994.

[53] H. Opitz. Pressure pad bearings. In *Proc. Instn Mech. Engrs.182*, number 182 in 3A(1967-68), pages 100–115, 1968.

[54] Doyle Jay Jr. Orr. *Macro-scale Investigation of High Speed Gas Bearings for MEMs Devices.* PhD dissertation, Massachusetts Institute of Technology, Department of Aeronautics and Astronautics, February 2000.

[55] Pan and Malanoski. *Fixed Thrust Bearings*, chapter 6.3. Mechanical Technology Incorporated, 1972.

[56] Edward Stanley Piekos. Personal Communication. PhD colleague in the MicroBearing team, Massachusetts Institute of Technology, 2000.

[57] Edward Stanley Piekos. *Numerical Simulation of Gas-Lubricated Journal Bearings for Microfabricated Machines.* PhD dissertation, Massachusetts Institute of Technology, Department of Aeronautics and Astronautics, February 2000.

[58] E.S Piekos and K.S. Breuer. Pseudospectral orbit simulation of non-ideal gas-lubricated journal bearings for microfabricated turbomachines. Paper No. 98-Trib-48 presented at the Tribology Division of The American Society of Mechanical Engineers, Toronto, Canada, October 1998.

[59] E.S Piekos, D.J. Orr, S.A Jacobson, F.F Ehrich, and K.S Breuer. Design and analysis of microfabricated high speed gas journal bearings. AIAA Paper 97-1966, presented at 28th AIAA Fluid Dynamics Conference, Snowmass Village, CO, June 1997.

[60] Lord Rayleigh. *The Theory of Sound*, volume 2. Dover Publication, New York, second edition, 1945.

[61] H.H. Richarson. Static and dynamic characteristics of compensated gas bearings. *Trans. ASME*, pages 1503–1509, 1958.

[62] W.B. Rowe. *Hydrostatic and hybrid bearing design.* Butterworth and Co. (Publisher) Ltd 1983, Liverpool, first edition, 1983.

[63] Nicholas Savoulides. Low order models for hybrid gas bearings. Master of science in mechanical engineering thesis, Massachusetts Institute of Technology, 2000.

[64] C.M.. Spadacinni. MicroEngine Weekly Presentation:Hydrocarbon Micro-combustor Experiments, June 15th, 2000. MIT MicroEngine Project, Massachusetts Institute of Technology.

[65] Paul Steranka. Pressure measurements in a miniature gas bearing. Gyro spin axis hydrodynamic bearing symposium, Massachusetts Institute of Technology, Instrumentation Laboratory, Cambridge, Massachusetts, December 1966.

[66] Y-C. Tai. *IC-Processed Polysilicon Micromechanics: Technology Material and Devices.* PhD thesis, University of California, Berkeley, 1989.

[67] Tom Takacs and Dennis Ward. Personal Communication. Microfabrication specialists, MIT MicroEngine Project. Massachusetts Institute of Technology, 2000.

[68] I.C. Tang and W.A. Gross. Analysis and design of externally pressurized gas bearings. *ASLE Transactions*, pages 261–284, 1962.

[69] J. H. Vohr. A study of inherent restrictor characteristics for hydrostatic gas bearings. Technical Report Vol. 2, Paper 30, University of Southhampton Gas Bearing Symposium, 1969.

[70] I.A. Waitz, G. Gautam, and Y.-S. Tzeng. Combustors for micro-gas turbine engines. *AMSE Journal of Fluids Engineering*, 120, March 1998.

[71] R.T.P. Whipple. Herringbone pattern thrust bearings. Technical Report 29, A.E.R.E T/M, 1949. Declassified in 1957.

[72] Frank White. *Viscous Flow.* McGraw-Hill, Inc., New York, New York, second edition, 1994.

[73] S. Whitley and L.C. Williams. The gas-lubricated spiral-groove thrust bearing. Technical Report 28 RD/CA, A.E.R.E E/R, 1959.

[74] William E. Wiesel. *Spaceflight Dynamics.* McGraw-Hill, Inc., New York, New York, first edition, 1989.

[75] D.V. Woodsworth. The viscosity thrust plate bearing. Technical Report 2217, A.E.R.E E/R, 1952. Declassified in 1956.

[76] Xin Zhang. Personal Communication. Research Scientist, Microsystems Technology Laboratories, Massachusetts Institute of Technology, 2000.